Université du Québec
Institut national de la recherche scientifique
Centre Énergie, Matériaux, Télécommunications

SELF-ASSEMBLY OF EUMELANIN MONOMERS INVESTIGATED BY SCANNING TUNNELING MICROSCOPY

Par

Fabrizio De Marchi

Thèse présentée pour l'obtention du grade de
Philosophiae Doctor, Ph.D.
en sciences de l'énergie et des matériaux

Jury d'évaluation

Président du jury et examinateur interne	Prof. Andreas RUEDIGER INRS-EMT
Examinateur externe	Prof. Antonella BADIA Université de Montréal
Examinateur externe	Prof. Louis CUCCIA Université Concordia
Directeur de recherche	Prof. Federico ROSEI INRS-EMT

© Droits réservés de Fabrizio De Marchi, April 2019

ABSTRACT

In nature, complex systems are commonly built by the aggregation of small building blocks in a process called “self-assembly”. By mimicking and controlling this bottom-up approach, it would be possible to design and build all sorts of nanostructures, simply by using a proper set of molecular building blocks. However, the *a priori* design of self-assembled structures and properties is still far from been achieved.

More insight can be gathered by the use of a simple model system, to understand how a molecule on a surface will interact with its neighbours or with the substrate itself. Nonetheless, the same molecular precursors are often involved in biologically relevant processes and form sophisticated materials like enzymes and ribosomes. Understanding their self-assembly could lead to the ability to encode this kind of complexity and information density into engineered self-assembled molecular structures.

Within this view, we present here the results concerning the systematic investigation of functionalized indols over various substrates (HOPG, Au and Ag). The chosen molecules are the precursors of eumelanin, an elusive class of black insoluble polymers derived biogenetically from tyrosine with potential application in bioelectronics.

Scanning Tunneling Microscopy allows to observe the formed 2D self-assembled structures in a reduced complexity environment, where the relation between the weak non-covalent intermolecular interactions and the adopted supramolecular structure can be uncovered. X-ray Photoelectron Spectroscopy monitors the variation of the chemical state of the molecule, while density functional theory and Monte Carlo simulation corroborate our hypothesis.

The self-assembled structure formed by indole 2-carboxylic acid (I2CA) has a single carboxylic acid that creates hydrogen-bonded dimers, which are arranged into lamellar structures relatively independently of the substrate and preparation conditions. The catechol group of 5,6-dihydroxyindole (DHI) is instead strongly affected by the applied surface, which triggers a redox reaction leading to metal-organic nanostructures on Ag(111) or covalent dimers on Au(111). The presence of both a carboxyl and a catechol in 5,6-dihydroxyindole-2-carboxylic acid (DHICA) leads to a variety of different architectures, determined by the interplay between its carboxyl and hydroxyl groups. The catechol group oxidizes upon O_2 exposure, triggering further phase transformations.

Keywords : Scanning tunneling microscopy, molecular self-assembly, eumelanin

RÉSUMÉ

Dans la nature, des systèmes complexes sont généralement construits en agrégeant de petits sous-unités, avec un processus appelé «auto-assemblage». En imitant et en contrôlant cette approche ascendante, il serait possible de concevoir et de construire toutes sortes de nanostructures, simplement en utilisant un ensemble approprié de précurseur moléculaires. Cependant, la capacité d'une conception *a priori* de structures et de propriétés auto-assemblées est encore loin d'être atteinte.

L'étude d'un système simple peut servir à mieux comprendre comment une molécule sur une surface interagira avec ses voisins ou avec le substrat lui-même. Néanmoins, les mêmes modestes précurseurs moléculaires sont souvent impliqués dans les processus biologiques pertinents et forment des matériaux sophistiqués tels que les enzymes et les ribosomes. La compréhension de leur auto-assemblage pourrait permettre de coder ce type de complexité et de densité d'informations dans des structures moléculaires auto-assemblées.

Dans cette perspective, nous présentons ici les résultats concernant l'étude systématique des indoles fonctionnalisés sur divers substrats (HOPG, Au et Ag). Les molécules choisies sont le précurseur de l'eumélanine, une classe insaisissable de polymères noirs insolubles dérivés biogénétiquement de la tyrosine avec une application potentielle en bioélectronique. La microscopie à effet tunnel permet d'observer les structures auto-assemblées 2D formées dans un environnement de complexité réduite, où la relation entre les interactions intermoléculaires non-covalentes et la structure supramoléculaire adoptée peut être découverte. La spectroscopie photoélectronique x surveille la variation de l'état chimique de la molécule, tandis que la théorie de la densité fonctionnelle et la simulation de Monte Carlo corroborent notre hypothèse.

La structure auto-assemblée formée par l'acide indole 2-carboxylique (I2CA) possède un seul acide carboxylique qui crée des dimères liés à l'hydrogène, qui sont disposés en structures lamellaires relativement indépendantes du substrat et des conditions de préparation. Le groupe catéchol de 5,6-dihydroxyindole (DHI) est fortement réactive, et donne à la molécule la capacité de former des nanostructures organométallique organiques sur Ag(111) ou des dimères covalents sur l'Au(111). Par contre, l'interaction entre le carboxyle et le catéchol dans l'acide 5,6-dihydroxyindole-2-carboxylique (DHICA) a conduit à une variété d'architectures différentes, déterminées par les interactions entre ses groupes carboxyle et hydroxyle.

Mots-clés : Microscopie á effet tunnel, eumélanine, auto-assemblage moléculaire, indole

SOMMAIRE RÉCAPITULATIF

CHAPITRE 1 : INTRODUCTION

1.1 Trouver l'inspiration á partir de l’observation du monde naturel

Les systèmes biologiques sont capables de produire une grande variété de matériaux, dont des structures élaborées possèdent des propriétés incroyables et des caractéristiques uniques. Parmi ces chefs-d'œuvre naturels, nous pouvons inclure les coquillages, les perles, les coraux, les cornes, le bois et la soie. De la même manière, aussi notre corps est constitué d’une multitude de matériaux possédants des qualités extraordinaires, comme les os, les dents, le collagène et les fibres musculaires. Ces matériaux ne sont pas seulement complexes, mais ils sont également très organisés, du niveau moléculaire à l’échelle nanométrique.

Les processus biologiques montrent une forte prévalence pour une approche « ascendante », où les ensembles sont construits pièce par pièce (figure 1.1a), souvent dirigé par la présence d'un échafaudage. Les structures sont ainsi obtenues en empilant ses composants très simples un sur l’autre, plutôt qu'en éliminant du matériau d'une pièce brute jusqu'à l'obtention des caractéristiques et dimensions souhaitées, comme dans la photolithographie et dans les autres processus « descendants » utilisé dans la microélectronique (figure 1.1b). La plupart des principaux processus ascendants qui se produisent dans la nature, de l'échelle moléculaire à l'échelle planétaire, entrent dans la catégorie de l'auto-assemblage, ou de l'organisation autonome d'unités de base en des modèles plus vastes, sans aucune intervention extérieure.

Du point de vue plus rigoureux de la science des matériaux, il est utile d'utiliser le terme auto-assemblage moléculaire, en référant qu’aux processus qui ont lieu à l'échelle nanométrique. L’auto-assemblage ne se limite pas à l'agrégation spontanée de molécules, mais comprend la création de matériaux raffinés et des machines moléculaires qui ont non seulement la capacité de haute précision, la flexibilité et la correction d'erreur, mais sont également autonomes et en constante évolution.

Le biomimétisme - apprendre à partir de formes et de processus naturels puis à les imiter - a permis de pousser l’innovation humaine dans plusieurs domaines, allant d’applications avancées, telles que les surfaces superhydrophobes inspirées du lotus (figures 1.4a-b), à des

applications quotidiennes plus banales, telles que des bandes Velcro dont la forme rappelle les crochets Xanthium (Figure 1.4c-d). Il n'est donc pas surprenant que l'étude des processus d'auto-assemblage ait fourni une source d'intérêt et d'inspiration, en particulier dans le domaine de la nanotechnologie, offrant une approche peu coûteuse et efficace pour la préparation de matériaux nanométriques. Les possibilités offertes par l'auto-assemblage peuvent être la solution à la croissante demande de caractéristiques plus petites. En fait, les approches ascendantes présentent un avantage considérable par rapport aux techniques descendantes, telles que la lithographie, car la taille la plus petite des caractéristiques n'est limitée par aucune limite physique sauf de la taille des blocs moléculaires utilisés. Les objets nanométriques, tels que les molécules, les points quantiques ou les nanotubes peuvent s'auto-assembler pour produire toutes sortes de structures complexes et d'agrégats moléculaires, qui peuvent á son tour être utilisé pour plusieurs applications différentes. Dans cette perspective, il sera présenté dans cette thèse une étude sur le mécanisme d'auto-assemblage de l'eumélanine, un pigment naturel très intéressant pour des applications de bioélectronique. En étudiant l'agrégation des précurseurs de l'eumélanine et en observant les structures qu'ils forment, on peut obtenir aussi des idées fondamentales sur les interactions entre les sous-unités moléculaires, une étape cruciale pour développer davantage notre connaissance de la chimie supramoléculaire.

1.2 La chimie au-delà de la liaison chimique

Contrairement à la chimie traditionnelle, qui se concentre principalement sur les liaisons covalentes, la chimie supramoléculaire est spécialisée dans les interactions non covalentes. Parmi ses différentes branches, la chimie supramoléculaire s'occupe aussi de la préparation des nanostructures bidimensionnelles ; le domaine de l'auto-assemblage en surface, ou chimie supramoléculaire 2D, comme son nom l'indique, est centré sur ce qui se passe sur un substrat, où les fragments moléculaires peuvent se réorganiser pour former des réseaux périodiques appelés monocouches auto-assemblées (SAMs). Plusieurs composants contribuent à la formation de tels arrangements moléculaires : à part de l'interaction molécule-molécule, la surface elle-même joue un rôle important, non seulement en tant que support/contrainte mais aussi en influençant la dimensionnalité de la structure auto-assemblée. En raison de son interaction avec l'adsorbat, la surface peut aussi entraîner la croissance vers une structure qui ne serait pas obtenue en solution. Les surfaces représentent donc un terrain de jeu unique. Le confinement spatial dans deux dimensions ajoute des contraintes supplémentaires, interdisant dans certains cas la formation d'une configuration de liaison particulière en raison d'un empêchement stérique. De plus, une fois que les précurseurs moléculaires sont adsorbés sur

un substrat, la formation de domaines chiraux n'est pas rare, même si la molécule elle-même est achirale. Enfin, la présence d'un substrat peut jouer le rôle de catalyseur et déclencher des modifications chimiques.

Néanmoins, l'avantage principal de disposer d'un substrat est plutôt lié aux méthodes de caractérisation qui peuvent être utilisées pour étudier les échantillons. Des techniques de microscopie à sonde locale sont utilisées pour étudier les échantillons cultivés sur des surfaces, qui permettent l'imagerie à l'échelle moléculaire (ou même sous-moléculaire !) des réseaux auto-assemblés, et permettant ainsi d'identifier les arrangements moléculaires, une tâche très difficile à aborder avec des approches plus traditionnelles (Figure 1.6).

1.3 La biologie à l'échelle nanométrique

L'un des appareils de microscopie à sonde locale (SPM) les plus intéressants est sans aucun doute le microscope à effet tunnel (STM). Comme les autres techniques SPM, le STM peut régulièrement fournir une résolution sous-moléculaire de molécules sur une surface, à condition qu'elle soit dotée d'une pointe suffisamment acérée. Même si l'image STM résultante est la convolution de la densité d'état et de la morphologie de surface, un utilisateur expert est capable d'identifier rapidement les molécules et de déduire la structure du réseau par comparaison avec des systèmes plus simples. Le STM est devenu donc la méthode de choix pour la caractérisation des réseaux 2D supramoléculaires, car il permet de répondre aux questions fondamentales de la chimie supramoléculaire et de la science de surface, ainsi que de soutenir le développement de nouveaux nanomatériaux. En même temps, la capacité de suivre les processus biologiques à l'échelle nanométrique, comme la reconnaissance cellulaire et la signalisation, est une opportunité intéressante, car elle permettrait d'obtenir des informations importantes sur les interactions des petites biomolécules qui peuvent à leur tour être exploitées pour de nouvelles applications technologiques telles que les biocapteurs ou les implants biocompatibles.

Dans cette optique, un excellent exemple d'application du STM à la chimie supramoléculaire est donné par l'auto-assemblage de bases nucléiques. Les interactions qui sont à l'origine des paires Watson-Crick (W-C) sont d'importance fondamentale pour la bonne exécution de la réplication de l'ADN, ainsi que de la force motrice pour la polymérisation du premier oligonucléotide - d'où l'origine de la vie. Cependant, afin de mieux comprendre la complémentarité entre les bases nucléiques (NB), tous les différents apports (liaison

hydrogène, énergie de solvatation, interactions hydrophobes et de van der Waals) devaient être déterminés séparément, une tâche expérimentale très difficile. Les travaux réalisés par les groupes de Heckl et Besenbacher ont permis de visualiser ces configurations de liaison sur une surface et ils ont confirmé que leur auto-assemblage ne se limite pas à des interactions de type W-C. Indépendamment de leur structure similaire, chacque NB forme un réseau avec des structures différentes : la guanine (G) et l'adénine (A) forment des réseaux 2D étendus, contrairement à la cytosine qui forme une structure de filament désordonnée. L'identification du comportement d'auto-assemblage de chaque NB a permis l'étude de systèmes plus complexes, comme la codéposition des deux NBs complémentaires (CG) ou non complémentaires (CA). La structure résultante confirme la spécificité de l'interaction W-C, car la guanine était intégrée à la structure du filament C, contrairement à la codéposition de C et A qui conduisait à la formation de deux phases distinctes après le recuit.

1. 4 Eumelanin

Cette capacité du STM à visualiser les échantillons biologiques à l'échelle nanométrique, en plus d'obtenir des informations sur leur structure, pourrait être fondamentale pour clarifier la structure supramoléculaire de l'eumélanine, qui encore aujourd'hui représente un défi compliqué mais intriguant.

Comme son nom l'indique, ce pigment est une mélanine, une classe de macromolécules bio-fonctionnelles présentes dans la majeure partie de la biosphère. Il est très courant dans le corps humain où, avec la phéomélamine, il détermine les variations de couleur de la peau, les yeux et les cheveux. Les fonctions de l'eumélanine ne sont pas seulement liées à l'aspect esthétique, mais il s'agit également d'un photoprotecteur important. Les études sur les mélanines ont été si centrées sur l'eumélanine que les deux termes sont souvent utilisés de manière interchangeable.

La structure d'eumélanine, cependant, est toujours un argument de débat. Etant donné son insolubilité dans la majorité des solvants, il est nécessaire d'utiliser des techniques de caractérisation comme la cristallographie aux rayons X, qui par contre ne donne pas une réponse fiable en raison de la grande hétérogénéité chimique de l'eumélanine. Au niveau moléculaire, il est généralement convenu que l'eumélanine est une combinaison de le 5,6-dihydroxyindole (DHI) et le 5,6-dihydroxyindole-2-carboxylique (DHICA), qui sont présents dans toutes leurs formes redox: ortho -hydroquinone (H2Q), -sémiquinone (SQ) et - (indole) quinone (Q) (figure 1.17).

La biosynthèse de l'eumélanine et de la phéomélamine rappelle la conversion par oxydation de la catécholamine en aminochromes. Le processus, appelé mélanogenèse, est décrit par la voie de Raper–Mason, présentée à la figure 1.18. Une fois que nous nous éloignons des monomères simples et que nous essayons de regarder au niveau supramoléculaire, il devient de plus en plus difficile de décrire la structure de l'eumélanine. Á part les difficultés associées à la détermination du rapport DHI / DHICA, les unités monomériques de l'eumélanine possèdent un grand nombre de configurations de liaisons possibles. En fait, l'analyse de l'eumélanine naturelle isolée à partir d'encre sépia ou de celle produite par la réaction d'oxydation des précurseurs présente une collection de dimères et de trimères. En plus, l'eumélanine peut contenir des molécules non cyclisées, et la composition globale varie en fonction de l'état du substrat et d'oxydation utilisés pour la préparation.

En raison de cette structure plutôt complexe, l'eumélanine a toujours été décrite comme un hétéropolymère conjugué et étendu. Ce modèle, appelé "semiconducteur amorphe" pour suivre le formalisme de Mott-Davis, correspond bien à l'hétérogénéité chimique et aux propriétés observées, telles que le comportement de conduction et l'absorption expérimentale à large bande, qui rend l'eumélanine plus proche d'un semiconducteur inorganique que d'un matériau organique.

Un changement radical de point de vue structural de l'eumélanine a gagné du terrain ces dernières années, ce qui suggère que l'eumélanine n'est pas composée d'une grande structure étendue, mais plutôt de petits oligomères, moins de 10 unités monomériques, maintenus ensemble par des interactions non covalentes et aromatiques, qui forment des nano-agrégats dans une structure de type graphitique : l'eumélanine serait alors encore amorphe, mais constituée de structures hiérarchiques. Cependant, il y a encore trop peu de preuves directes pour soutenir le modèle de désordre chimique ainsi que l'organisation supramoléculaire de la mélanine. Dans le cadre de cette thèse, nous essayons donc d'aborder le problème en adoptant une approche ascendante de l'enquête. Au lieu de partir du polymère d'eumélanine formé, nous envisageons d'observer ses monomères dans un environnement de complexité réduite, comme le UHV. Semblable à ce qui a été montré précédemment pour les bases nucléiques, en étudiant les interactions entre les molécules DHI et DHICA avec un STM, nous espérons mieux comprendre le mécanisme à la base de l'agrégation des précurseurs de l'eumélanine. De plus, l'environnement UHV contrôlé nous permet d'étudier la polymérisation progressive des précurseurs, d'élucider la conformation de la liaison et d'évaluer le rôle des différents états d'oxydation du groupe catéchol qui affectent la structure auto-assemblée.

CHAPITRE 2 : TECHNIQUES EXPÉRIMENTALES

2.1 Microscopie à effet tunnel

Le STM est devenu la technique de choix pour l'étude de la morphologie superficielle du réseau moléculaire auto-assemblée (SAMNs), principalement en raison de sa haute résolution spatiale (de l'échelle nanométrique à l'échelle atomique) et grâce à la quantité d'informations obtenues. En termes généraux, le STM partage le même mécanisme de fonctionnement que les autres microscopies à sonde locale. Un système mécanique micrométrique permet d'approcher manuellement une pointe en face de la surface de l'échantillon à étudier. Après cela, un moteur à chenille arpenteuse place la pointe dans la zone ou domaine de fonctionnement de l'instrument ainsi qu'un système piézoélectrique qui lui permet de passer en mode balayage (ligne par ligne) sur l'échantillon. La distance entre l'échantillon et la pointe est constamment ajustée par un système de retour afin de suivre le profil de l'échantillon et d'éviter l'écrasement de la pointe sur la surface. Les données relatives à la hauteur ou à un autre type d'interaction sont ensuite collectées par un ordinateur qui les convertit ensuite en une image de la densité d'états (DOS), à partir de laquelle la topographie de l'échantillon peut être déduite.

Le STM permet d'obtenir un profil morphologique à l'échelle atomique de la surface sans utiliser de source électronique. En effet, le fonctionnement est basé sur l'effet tunnel: la pointe et l'échantillon sont maintenus à des tensions différentes, à peu de Å l'un de l'autre, forçant un courant électrique à passer à travers la «barrière anti-tunnel» entre eux. Généralement, les courants tunnel sont de l'ordre de quelques nanoampères (0,1−5nA) et la tension appliquée à travers la barrière est comprise entre 10 mV et 10V. La distance entre le noyau de l'atome situé à l'apex de la pointe et le noyau d'un atome de l'échantillon étudié est généralement maintenue entre 5 et 15 Å. En plus des informations morphologiques, il est également possible d'effectuer des mesures spectroscopiques, pour obtenir les spectres I/V, liés à la conductance de l'échantillon et donc à sa bande énergétique.

2.2 Spectroscopie photoélectronique par rayons X

Bien que la plupart de ces travaux de thèse tournent autour de l'analyse STM de réseaux 2D auto-assemblés, les informations morphologiques obtenues ne suffisent pas à caractériser complètement un échantillon, et par conséquent, des techniques complémentaires sont

nécessaires. En particulier, l'analyse de la composition de la surface est importante pour identifier les molécules ou détecter la présence de contaminants, tandis qu'une analyse chimique plus sophistiquée est aussi nécessaire pour discerner entre les différents états d'oxydation des composés chimiques, comme dans le cas de nos précurseurs d'eumélanine.

La spectroscopie par photoémission (PES) est souvent la technique de choix. Son mécanisme de fonctionnement implique l'utilisation de la loi photoélectrique d'Einstein, ou l'émission d'un électron après l'absorption atomique d'un photon.

En termes généraux, les expériences PSE partagent toutes la même procédure générale. L'analyse des échantillons se fait dans un environnement UHV, afin d'améliorer la transmission des photoélectrons et de minimiser la contamination. Les photons générés par une source de lumière monochromatisée, sont irradié sur échantillon pour générer des porteurs de charge par effet photoélectrique. Alors que la profondeur de pénétration de la lumière varie en fonction de sa longueur d'onde, le libre parcours moyen des électrons est de l'ordre de quelques nanomètres, les informations collectées sont en relation avec la surface et les PES sont donc considérés comme des techniques d'analyse de surface. Ces photoélectrons sont collectés, résolus en énergie, légèrement retardés et comptés en fonction de l'angle d'émission et de l'énergie cinétique par un analyseur d'énergie. À son tour, l'énergie cinétique de l'électron émis est liée à ses états électroniques d'origine, ainsi qu'à son état vibratoire et à son niveau de rotation, qui sont spécifiques à chaque élément chimique.

Á partir de cette approche commune, différentes techniques du PSE ont été développés et nommés en fonction de la longueur d'onde utilisée. Chaque type de source déterminera de quelles orbitales moléculaires les photoélectrons vont être émis, et donc les propriétés qui peuvent être étudiées. Par exemple, la spectroscopie photoélectronique UV (UPS) repose sur les photoélectrons émis après l'absorption de la lumière ultraviolette dans l'échantillon, généralement à partir d'une lampe à décharge à base d'Hélium (He). La faible énergie du rayonnement UV (<41 eV) est suffisante pour éjecter des électrons seulement à partir de la couche de valence, ainsi l'UPS est plus appropriée pour évaluer le travail de sortie du matériau. Pour étudier la composition élémentaire et le profil de profondeur, la spectroscopie photoélectronique X (XPS) est plus appropriée, car l'absorption du rayonnement X (1000-1500 eV) permet de sonder les électrons des orbitales de liaisons. La nomenclature spectroscopique des caractéristiques XPS est directement liée aux différents nombres quantiques. Le nombre quantique principal apparaît en premier, suivi du moment cinétique étiqueté comme et enfin l'élan total.

2.3 Procédures

Le déroulement standard d'une expérience dans le système SPECS implique la préparation et le nettoyage des substrats métalliques. L'échantillon est transféré dans la chambre SPECS pour un nettoyage par pulvérisation dans un plasma d'argon pur (Ar) dans le but d'éliminer les oxydes/contaminations. L'Ar est donc injecté dans la chambre à travers une valve de fuite jusqu'à l'obtention d'une pression partielle de $1x10^{-6}$ mbar, puis la surface de l'échantillon métallique est bombardée par des ions d'Ar^+ pendant 10-15 ' à 1-2 keV. Après la pulvérisation, la surface devient très rugueuse et un recuit thermique à 450-550 °C sera effectué pendant 30' pour diminuer la rugosité et avoir une surface lisse. Le processus doit être répété plusieurs fois jusqu'à l'obtention d'une surface atomiquement plane. L'échantillon est caractérisé par STM, afin d'évaluer la qualité de surface sur laquelle, des images à haute résolution seront réalisée et enregistrer. Ses images qui seront par la suite utilisées comme références au cours des étapes successives. Des procédures de préparation similaires ont été adoptées pour la caractérisation XPS de l'échantillon, réalisée dans le système Omicron. Pour déclencher l'oxydation, la même procédure a été adoptée dans les deux chambres UHV: les échantillons ont été exposés à l'O_2 gazeux par dosage à travers une vanne de fuite dans la chambre principale, à une pression de 10^{-6} mbar pendant 30 minutes.

CHAPITRE 3 : AUTO-ASSEMBLAGE DE L'I2CA

Les systèmes modèles sont essentiels pour notre compréhension des processus d'auto-assemblage. Dans une première étape de notre étude des monomères d'eumélanine, nous avons étudié l'auto-assemblage en surface d'un acide indole avec une simple fonction, l'I2CA une petite molécule planaire bicyclique comprenant du benzène et du pyrrole (figure 3.1a). La molécule est caractérisée par une seule fonction carboxylique, qui ne laisse que peu de possibilités de liaison hydrogène intermoléculaire (OH···O, NH···O, CH···O), et par la faible symétrie de la molécule, qui augmente le nombre des géométries moléculaires possibles au sein des motifs de liaison.

L'auto-assemblage en surface de molécules comportant deux à quatre groupes carboxyle a fait l'objet de nombreuses études. Lorsqu'ils sont disposés de manière appropriée, les groupes –COOH facilitent la formation de réseaux ordonnés liés à l'hydrogène sur des surfaces relativement non réactives, notamment HOPG et Au (111). Ces surfaces sont généralement sélectionnées pour permettre des interactions intermoléculaires, plutôt que des interactions molécule-substrat, jouant le rôle le plus important dans la formation du film moléculaire. Moins d'études ont été réalisé sur les systèmes avec des degrés de fonctionnalisation plus bas, car, *a priori*, leur capacité de former des architectures bidimensionnelles ordonnées est réduite.

Il existe une littérature limitée sur l'auto-assemblage en surface de molécules avec un seul groupe –COOH, et donc plus d'investigations et de recherches s'avéreraient utiles. Par exemple, l'acide benzoïque, l'acide à base de benzène le plus simple, ne produit aucune structure ordonnée bidimensionnelle à longue distance. De même, l'acide thiophène-2-carboxylique ne produit pas des structures observables. D'autre part, les acides pyridinecarboxyliques peuvent former des couches ordonnées, stabilisées par des interactions OH···N et CH···O à l'interface liquide/HOPG, et il a été démontré que l'acide ferrocénécarboxylique formait des pentamères avec des liaisons hydrogène sur Au(111).

Les calculs DFT pour la configuration possible de dimères et trimères d'I2CA révèlent des énergies compatibles avec celles trouvées pour d'autres molécules carboxylées. Le dimère avec une liaison cyclique –COOH est l'architecture la plus stable. Les structures dimères décalées sont moins stables et présentent une différence d'énergie raisonnable entre les deux isomères I2CA (-6,60 kcal / mol par molécule contre -0,92 kcal / mol par molécule) pour qu'on

peut raisonnablement supposer que seule la structure montrée à la figure 3.1f devrait être observable.

Une fois déposait sur Au (111) ou à l'interface TCB / HOPG, I2CA auto-assemble en formant de vaste SAMN, avec une structure similaire à celle prédite par DFT en phase gazeuse. Les dimères –COOH s'entassent sous forme des lamelles ordonnées (structure à double lamelle, figure 3.2 et 3.3). L'espacement intra-lamellaire entre les dimères est réduit sur HOPG, amenant à des différences dans la maille primitive entre Au (111) et HOPG. Ces légères différences dans l'empilement lamellaire sont dues aux différences épitaxiales entre les deux surfaces. Dans quelques d'expériences, nous avons observé la formation sur TCB / HOPG d'une structure dans laquelle chaque lamelle contenait des dimères I2CA avec des angles d'inclinaison identiques (structure lamellaire unique, figure 3.4).

Les calculs DFT en PBC montrent que le système a besoin d'une contribution énergétique par l'interaction de surface pour se stabiliser ; l'énergie de cohésion prédite est positive et cette barrière d'énergie répulsive doit donc être surmontée par des interactions molécule-substrat. Les calculs suggèrent donc que l'épitaxie de substrat commande l'assemblage des couches ; en l'absence de substrat, un assemblage 2D est peu susceptible d'être stable. Des considérations énergétiques nous amènent à prévoir que la structure à double lamellaire contient un dimère cis-symétrique dans la cellule élémentaire, alors que la structure à lamelle unique contient un seul dimère -COOH trans-symétrique. Cependant, même avec l'imagerie haute résolution offerte par l'UHV, il n'était pas possible de distinguer les trois conformations possibles du dimère présentées dans la figure 3.1 (cd). Les molécules I2CA apparaissent systématiquement en forme de poire, dépourvues de toute asymétrie du cycle pyrrole à partir duquel la position de l'azote peut être déduite.

En utilisant de l'acide heptanoïque comme solvant, nous observons une structure différente sur HOPG, comme le montre la figure 3.4 La structure n'a pas des lamelles bien définie vue à l'interface TCB/HOPG. Le contraste de l'image suggère un appariement de molécules I2CA incompatible avec la dimérisation de -COOH observée sur Au (111) ou lorsque le TCB était utilisé comme solvant. Le grand espacement entre les dimères I2CA liés OH···N implique que le solvant de l'acide heptanoïque adsorbe avec l'I2CA.

CHAPITRE 4 : RÉACTIVITÉ DU DHI

Suite à notre étude sur I2CA, nous avons confirmé que les précurseurs de l'indole adsorbent de manière plane sur la surface d'Au(111). Nous avons également vu que les interactions latérales permettent la formation des réseaux stables 2D, et donc la prochiralité joue un rôle important. Tous ses constatations intéressantes, nous permettrons par la suite d'étudier des systèmes plus complexes.

Dans cette perspective, nous poursuivons notre enquête sur les réseaux monocouches auto-assemblés (SAMN) d'indoles fonctionnalisés en présentant nos travaux sur DHI, dans lequel un cycle pyrrole est fusionné avec un catéchol. Le catéchol (o-dihydroxybenzène) et ses dérivés ont fait l'objet de recherche croissante en chimie des polymères en raison de leur pouvoir collant polyvalent. Malgré cela, l'exploitation possible de groupes fonctionnels de catéchol pour des applications d'auto-assemblage 2D n'a pas été étudiée en détail, bien que leur chimie permette plusieurs interactions qui favoriseraient la formation de nanostructures stables. Alors que les groupes hydroxyle peuvent créer des SAMN stabilisés par liaison hydrogène, les catéchols peuvent en outre subir des réactions redox réversibles, se transformant en formes de semiquinone et de quinone (Figure 4.1). La déshydrogénation partielle peut induire une transition de phase vers des architectures plus robustes, en exploitant les interactions entre le catéchol et ses formes oxydées. Sans oublier que le DHI est également un des derniers produits intermédiaires monomères du processus biochimique qui transforme la tyrosine en mélanine.

Après avoir déposé DHI sur Ag, les molécules s'assemblent dans des structures lamellaires à travers la surface (Figure 4.2 a), qui présente de multiples domaines d'orientation pouvant aller jusqu'à des centaines de nanomètres à la surface. Les lamelles sont formées par des paires moléculaires dont les dimensions suggèrent un assemblage non lié par covalence. La séparation entre les lamelles diminue lorsque la couverture moléculaire augmente. Le contraste et la forme des molécules formant le dimère ne sont pas identiques (figure 4.2b). Au biais positif, un trait brillant supplémentaire, probablement un atome d'argent, semble être logé entre les deux molécules à l'intérieur de la lamelle (Figure 4.2c), que nous avons provisoirement attribués à une structure métal-organique. La différence de contraste entre ces caractéristiques peut être dû à plusieurs conformations de DHI, à sa géométrie prochirale, ou à différents états d'oxydation résultant du rédox catéchol-quinone. Pour bien caractériser la structure lamellaire,

une mesure XPS des réseaux moléculaires DHI sur Ag (111) a été réalisée (Figure 4.3). Les spectres O1s révèlent la présence de pics de catéchol et de quinone : le pic principal à 533,0 eV (figure 4.3b) est attribué au groupe hydroxyle (O-C) du catéchol, tandis que le pic à 2,0 eV BE inférieur (531,1 eV) est attribué à O=C, ce qui suggère que les groupes sont oxydés en carbonyle. Ceci est cohérent avec les spectres C1s correspondants dans lesquels un pic à 288,7 eV, affecté à C=O, est identifié (Figure 4.3a). D'après ces données, nous en déduisons que le DHI adsorbé sur l'Ag(111) est présent sous deux formes : le catéchol et son pendant oxydé sous la forme d'indole-5,6-quinone (IQ, figure 4.1c). Nous pouvons déterminer la proportion des deux formes rédox à partir du rapport 4:7 entre l'aire des composantes O=C (IQ) et O-C (DHI) des O1s de la figure 3b.

Pour poursuivre notre évaluation de la réactivité du catéchol à la surface, nous avons tenté de déclencher une oxydation en exposant les SAMN 2D sur Ag (111) à l'oxygène. Après exposition à l'oxygène, nos spectres XPS montrent un changement évident du pic de O1s (Figure 4.5c). Une augmentation du pic O=C aux dépens de O-C a été observée (Figure 4.5b). La FWHM du pic de C-O a fortement augmenté, ce qui peut être dû à la conformation à liaisons hydrogène multiples adoptée par le groupe hydroxyle. En outre, un troisième pic apparaît à 529,9 eV, ce qui est lié à la formation d'oxyde d'argent à la surface. La transformation du catéchol en quinone peut également être déduite du spectre C1s (Figure 4.5a), où, conformément aux données O1s, il existe une augmentation de la surface de pic attribuée à C=O. Du point de vue morphologique, nous voyons que l'exposition à l'oxygène détruit l'auto-assemblage lamellaire, la majorité des molécules étant assemblées en amas désordonnés, comme le montrent les figures 4.4a et b. Il y a un manque d'ordonnancement à long portée mais il est souvent possible de voir de petits points proches de plusieurs molécules, qui suggère que les adatomes Ag sont toujours incorporés dans une structure organométallique.

De taches de molécules ordonnées ont parfois été trouvées à la surface, comme le montre la figure 4.4c, dans lesquelles des chaînes de molécules plus brillantes sont alternantes disposées autour d'un fragment moléculaire plus sombre. Cette variation du contraste STM peut être due à un état d'oxydation différent de DHI, similaire à celui illustré à la figure 4.2b, ou à une disposition différente de la molécule par rapport à ses voisins. L'unité cellulaire de cette structure contient 14 molécules et ni l'annelage ni l'exposition ultérieure à l'O_2 ont conduit à des domaines ordonnés plus grands ; pour une exposition plus élevée (c'est-à-dire une concentration plus élevée de QI), aucune phase ordonnée a été observée. La déshydrogénation

supplémentaire n'a pas amélioré l'ordre, ce qui suggère qu'un rapport minimum de catéchol sur quinone était nécessaire pour la stabilité de la structure.

Lorsqu'elles sont déposées sur Au, les molécules DHI s'auto-assemblent dans une structure différente de celle observée sur Ag (111). Chaque maille contient une paire de dimères dans un arrangement compact, disposés perpendiculairement les uns aux autres. La courte longueur de ces dimères n'est pas compatible avec l'assemblage non covalent, donc nous proposons une structure dimérique covalente. L'analyse XPS des échantillons DHI/Au(111) montre que la molécule est constituée de catéchol pur. Bien que le pic de O1s soit très proche du pic d'Au4p, il est toujours évident, comparé au spectre de DHI/ Ag (111), qu'un seul composant est présent pour DHI sur Au (111). Comme confirmation supplémentaire, les C1s (Figure 4.8 a) ne montrent aucun pic lié à une composante C=O. La position du composant CC étant proche de celle obtenue pour Ag, elle permet donc de réduire la présence d'une liaison organométallique C-Au, dont la présence serait indiquée par un composant de BE inférieur. Encore une fois, la position de pointe de N1s est proche de celle du pyrrole à 400,0 eV. L'absence de pics supplémentaires à 399,0 eV liés à la liaison aromatique C = NC exclut la présence de la forme semiquinone. Similaire à Ag, le recuit n'affecte pas l'auto-assemblage moléculaire sur Au; Cependant, contrairement au cas Ag, les structures moléculaires sur Au restent inchangées après le dosage de l'oxygène, même après avoir été exposées aux conditions atmosphériques.

Sur la base de ces résultats expérimentaux, nous émettons l'hypothèse que le système DHI/Au(111) est composé de dimères covalent DHI-DHI. Bien qu'il ne soit pas inhabituel que des molécules se polymérisent à la surface d'Au, une étape de recuit est souvent nécessaire pour déclencher la polymérisation. Pour confirmer que la structure observée par STM sont des dimères DHI, une analyse TOF-SIMS de l'échantillon a été effectuée (Figure 4.9). Les spectres montrent à la fois que le monomère et le dimère sont présents à la surface. TOF-SIMS confirme également une sensibilité différente à l'oxydation des structures formées sur les deux substrats étudiés. Sur Au(111), aucun pic associé à IQ ne peut être observé, confirmant ainsi que le DHI/Au(111) est resté stable pendant le transfert entre les deux systèmes UHV, sans aucun processus d'oxydation. Un résultat opposé est obtenu pour Ag(111), où aucun dimère n'est visible, et le pic IQ est plus fort que son équivalent réduit.

Ces résultats montrent que la réaction du DHI sur les surfaces (111) est fortement affectée par la nature du substrat lui-même. Alors que sur Ag, les molécules réagissent pour former des structures métal-organique, sur Au, elles sont plutôt capables de se lier les unes aux autres et forment des dimères liés par covalence.

La réaction de dimérisation covalente proposée à la surface n'a été jamais rapportée pour une étude moléculaire 2D en surface. Bien que DHI soit bien connu pour son aptitude à polymériser dans des conditions appropriées, il s’agit du premier rapport présentant la polymérisation de fractions indole, réalisée sous UHV à température ambiante. D'autre part, alors que la polymérisation oxydante du DHI conduit généralement à une gamme de produits avec des longueurs de chaîne et des motifs de liaison différents, la présence d'une surface limite le processus, ne produisant que des dimères présentant une liaison à leurs positions 2-3. La conformation particulière des dimères à la surface suggère que la dimérisation est déclenchée par la réactivité du cycle indole. Dans un environnement acide, les molécules d'indole peuvent subir une réaction de polymérisation conduisant à leur trimérisation, dont les produits intermédiaires sont similaires aux dimères représentés à la figure 4.7c.

CHAPITRE 5 : LE POLYMORPHISME DU DHICA

Dans les deux chapitres précédents, nous avons montré comment le groupe fonctionnel définit la structure finale du réseau d'auto-assemblage.

Diverses architectures 2D sont possibles en raison des multiples faibles interactions du groupe catéchol malgré la création des dimères d'acide non covalents très stables par les acides carboxyliques qui dominent le processus d'auto-assemblage. Mais que se passe-t-il alors lorsque ces deux groupes sont présents en même temps ? Dans ce chapitre le résultat de notre enquête sur DHICA, sera présenté.

Par rapport aux deux systèmes modèles précédents, la présence de ces deux groupes fonctionnels dans DHICA augmente le nombre d'interactions possibles, ce qui permet ainsi la création de réseaux moléculaires auto-assemblés (SAMN) avec différents motifs de liaison (figures 5.1b et c).

Une fois déposé sur Au (111), DHICA peut s'auto-assembler en un certain nombre de motifs différents, avec une variété de phases souvent présentes simultanément à la surface. Les phases les plus courantes sont présentées sur la figure 5.2a, qui représente différentes architectures : un réseau ouvert poreux et carré, un réseau de type mur de briques et une phase qui ressemble à une échelle. Toutes les phases présentent des motifs de liaison avec les molécules toujours disposées, pour former des paires de dimères carboxyliques. La raison peut être élucidée en comparant les énergies de ces différentes liaisons hydrogènes (calcul DFT, Figure 5.4), où le dimère cyclique -COOH est au moins deux fois plus fort que les autres interactions. D 'ailleurs, le groupe catéchol peut adopter plusieurs conformations de liaison différentes pour former des liaisons hydrogènes, soit linéaires avec un autre catéchol, soit perpendiculaires par interaction avec l'azote et l'oxygène d'un DHICA voisin. Ces liaisons catécholiques sont assez proches en énergie et, puisque la stabilisation globale d'un SAMN est liée à la somme des interactions molécule-molécule, il peut y avoir plusieurs phases accessibles à température ambiante, ce qui est conforme à nos observations expérimentales.

Puisque nous ne pouvons pas exclure a priori que la différence au niveau de structure auto-assemblée puisse être due à la présence de différentes formes rédox de DHICA, nous avons tenté de déclencher l'oxydation de la partie catécholique de la molécule en exposant la molécule au O_2 gaz.

Nous avons constaté que l'exposition d'échantillons de DHICA/Au (111) entraînait plusieurs conséquences, selon la phase de démarrage. La phase á réseau ouvert ne semble pas être affectée par l'oxygène, et la même chose été observé pour la phase dimère covalente DHI. Alors que les autres phases sont plus fortement affectées et deviennent de plus en plus désordonnées à mesure qu'elles sont exposées à des pressions partielles croissantes d'O_2. Une transition de phase se produit après l'exposition de la molécule à 10^{-5} mbar d'O_2, produisant une structure avec des paires de dimères disposées en rangées, séparées par de fines lignes pouvant être des espèces diffusantes.

Contrairement aux SAMN non exposés, le recuit des phases désordonnées obtenues par oxydation conduit à un réarrangement du SAMN. La figure 5.6b-c montre qu'après un recuit thermique à 100 °C, le DHICA exposé à l'oxygène se réorganise en un réseau complexe à structure en nid d'abeille dont la cellule unitaire contient 18 molécules. Les molécules sont engagées dans une structure circulaire en forme de fleur, formant deux anneaux concentriques : six molécules sont situées au centre de la structure, pointant vers le centre du nid d'abeille, tandis que douze autres sont étroitement emballées pour former un deuxième anneau concentrique, chacune avec une orientation différente pour permettre la formation de paires de dimères linéaires dans un agencement rappelant la structure d'échelle obtenue à température ambiante. Contrairement à une structure cyclique similaire formée à partir d'I2CA, nous remarquons une symétrie élevée (et aucune chiralité apparente) dans l'assemblage. Ceci suggère que la disposition centrale en forme de fleur moléculaire ne peut pas provenir de la liaison hydrogène des fragments carboxyliques, car il a été observé que cela rompait la symétrie et induisait une torsion chirale. Une autre interprétation possible de cette configuration est que les molécules sont déprotonées et que six d'entre elles sont coordonnées autour d'un ou de plusieurs adénomes Au, dans une conformation similaire à celle observée par Lipton-Duffin et al. Cette hypothèse est encore renforcée par les images STM à plus faible biais qui montrent la présence d'une caractéristique en forme de point au centre de la structure en forme de fleur, ainsi que par la différence de contraste entre les molécules composant la structure centrale et celle dans leur environnement (figures 5.6a et b), qui suggèrent que ces molécules du cycle interne pourraient être dans un état chimique différent de leurs homologues du cycle externe. Conformément à ce qui est observé pour DHI, où les formes catéchol et quinone de la molécule présentent un contraste STM différent, cela suggère qu'une forme rédox différente de DHICA peut être formée après une exposition à l'O_2.

Nous pouvons donc supposer que la molécule est encore sous sa forme catéchol lorsqu'elle est déposée à la surface d'Au(111), mais contrairement à son homologue décarboxylé, elle est sujette à l'oxydation, probablement parce qu'elle n'a pas été stabilisé par dimérisation covalente.

CHAPITRE 6 : CONCLUSIONS ET PERSPECTIVES

Comme nous l'avons vu au cours des chapitres précédents, le dépôt d'indoles fonctionnalisés sur une surface a été une étude intéressante mais néanmoins ardue. L'indole rend la molécule adsorbée à plat sur la surface, ce qui le rendre un échantillon spécimen pour une étude STM. Grâce à la résolution nanométrique obtenue par cette technique, nous avons pu voir sur image les réseaux 2D créés par l'auto-assemblage de différents indoles fonctionnalisés, I2CA, DHI et DHICA. En même temps, en raison de la petite dimension de nos précurseurs moléculaires, il est très difficile de comprendre convenablement l'orientation de la molécule et sa prochiralité.

Dans cette perspective, les modélisation DFT et MC seraient fondamentales, car le résultat de leurs simulations soutiendrait ou rejetterait notre hypothèse expérimentale. Bien que l'objectif principal de cette étude sur les indoles fonctionnalisés soit d'élargir notre vision de la structure « désordonnée » de l'eumélanine, ces molécules se sont également révélées utiles pour le développement de la structure supramoléculaire. Quelles que soient les difficultés rencontrées, nous avons pu acquérir des connaissances importantes sur l'auto-assemblage et sur l'interaction entre les différentes liaisons non covalentes qui régissent le processus

Les résultats concernant l'investigation du I2CA représentent parfaitement cet aspect. Comme prévu, le groupe acide carboxylique pilote le processus d'auto-assemblage, entraînant la formation de dimères moléculaires liés à l'hydrogène sur Au (111). Alors que on passait de l'environnement UHV à l'interface liquide-solide, moins « idéale » et semblable au système biologique, nous avons constaté l'effet du solvant sur l'auto-assemblage. A l'interface TCB / HOPG, I2CA constitue toujours la structure compacte qui présente de légères différences dans l'empilement lamellaire en raison des contraintes épitaxiales différentes sur les deux surfaces. Bien que l'acide heptanoïque ait été utilisé comme solvant, la liaison OH · · · O entre l'acide carboxylique I2CA n'était pas présente, ce qui a favorisé la formation de dimères liés à OH · · · N. La conformation différente de l'auto-assemblage et le grand espacement entre les dimères impliquent la co-adsorption de I2CA.

La comparaison entre les différents modèles de réseaux I2CA montre que la structure lamellaire présente une orientation différente en fonction du tassement : alors que la structure à double lamellaire contient un dimère cis- et un trans-symétrique dans la cellule unitaire, la structure à une seule lamelle contient un seul dimère -COOH trans-symétrique. De plus, les calculs d'énergie de cohésion totale montrent que lorsque le substrat est absent, un assemblage 2D a

peu de chances d'être stable. Ceci suggère que l'acide carboxylique seul ne serait pas capable de construire une structure supramoléculaire plus grande semblable à celle qui a été supposé pour l'eumélanine. En revanche le groupe des catéchols ouvre beaucoup plus de possibilités, vu que notre enquête sur DHI a révélé. Une fois déposé sur Au (111), DHI s'auto-assemble et forme une structure compacte, dont les fonctionnalités imaginées par STM ne correspondent pas à celles attendues pour une seule molécule. La possibilité que la molécule forme des structures dimères covalentes lors de l'adsorption sans aucune étape de recuit a été étonnement prouvée par l'analyse TOF-SIMS. Ce type de développement est très intéressant, étant donné qu'une telle configuration de liaison est très rare dans les unités d'eumélanine. Le seul comportement similaire connu est la polymérisation de l'indole en solution acide, qui continue toutefois à produire un trimère cyclique.

Lorsqu'elle est déposée sur Ag (111), la molécule forme à nouveau une structure lamellaire, similaire à celle obtenue avec I2CA. L'orientation moléculaire était en revanche un peu inclinée et l'analyse XPS de l'échantillon démontrait que le DHI était partiellement oxydé par adsorption. Les structures montrées ainsi étaient de nature organométallique et composées d'un mélange de catéchols et de quinones. Ce processus d'oxydation pourrait être déclenché de plus par une exposition à l'oxygène, entraînant une conversion supplémentaire de l'espèce catéchol en quinone. Dans certains cas, le IQ peut déclencher une transition de phase des SAMN, mais nous n'avons pas été en mesure de contrôler systématiquement le taux d'oxydation afin de créer des structures avec un ordre à longue portée. Malgré cela, un tel comportement est sans antécédent. Bien que les groupes hydroxyles aient généralement été négligés, l'inclusion de groupes catéchols peut constituer un outil précieux pour la fabrication de précurseurs moléculaires auto-assemblés.

Après nos premières observations, nous avons essayé de mieux comprendre la mécanique des catéchols et de revenir à une surface plus inerte, telle que l'Au (111). D'autre part, après la formation du dimère covalent, le DHI est assez stable et ne s'oxyde pas même après exposition à l'O_2. Il était alors utile d'étudier l'auto-assemblage de DHICA sur Au(111), car nous nous attendions à ce que l'acide carboxylique sur le cycle pyrrole empêche la formation de tout dimère covalent. De plus, DHICA serait la référence idéale pour tester les connaissances que nous avons acquises jusqu'à présent sur les groupes carboxyliques et catéchols et viendrait compléter notre étude sur les monomères d'eumélanine.

Une fois à la surface d'Au, les molécules de DHICA se réarrangent en une multitude de polymorphes présentant différentes symmétries et densités de tassement, allant de poreux à

compacts, équarris et hexagonaux. Des motifs de liaison similaires sont partagés entre les phases, le dimère cyclique carboxylique étant omniprésent. La simulation en phase gazeuse DFT montre en fait qu'il s'agit de l'interaction intermoléculaire la plus stable, alors que le groupe catéchol ne présente pas de conformation de liaison préférentielle. La raison du polymorphisme DHICA est donc davantage axée sur la cinétique, en effet, les simulations de MC indiquent que même de légères perturbations de la force relative de ces interactions peuvent modifier l'équilibre entre les forces intermoléculaires, produisant les différents réseaux à la surface.

Le polymorphisme DHICA est encore plus intéressant lorsque la sensibilité de la molécule à l'oxydation est prise en compte. En fait, après avoir été exposée à l'O_2, la phase de réseau ouvert reste inchangée, tandis que pour les autres, l'ordre à longue distance est perdu et devient plus désordonné. Fait intéressant, le réarrangement moléculaire est modifié lors du recuit thermique. Comme dans le cas des commandes ordonnées de DHI/Ag (111), dans ce cas également, les réseaux semblent être composés de formes rédox mixtes de DHICA formant une structure organométallique.

Bien que ces résultats concluent notre étude sur les monomères d'eumélanine en surface, ce n'est que le premier pas vers une meilleure compréhension de la structure et du comportement de l'agrégation de l'eumélanine. Le STM démontre d'être un outil intéressant pour l'étude de petites molécules pertinentes sur le plan biologique et leur comportement d'auto-assemblage. Elles seront indispensables pour la poursuite du développement du projet. Comme nous l'avons vu, la contrainte de surface en 2D a gêné la formation de grands systèmes à liaisons covalentes, mais cette barrière peut être dépassée par l'utilisation d'un précurseur moléculaire plus grand. Une telle étude nous aiderait à mieux décrire la structure supramoléculaire de l'eumélanine : le précurseur de l'eumélanine s'auto-assemblerait-il de manière non covalente, comme dans le modèle du « désordre », ou par de liens covalents entre l'unité formée d'un plus grand hétéropolymère, comme dans le modèle semi-conducteur amorphe ? En outre, l'étude d'autres petits systèmes modèles, dotés de fonctionnalités différentes, pourrait permettre de mieux comprendre la polymérisation des catécholamines, ainsi que les interactions qui régissent l'auto-assemblage moléculaire.

L'application de ces résultats n'est cependant pas limitée au eumélanine / biologique. Après la dimérisation DHI sur Au, des précurseurs moléculaires pourraient être conçus à l'avance pour tenter d'obtenir un polymère conjugué 2D étendu, un objectif attirant pour l'électronique organique. D'un point de vue scientifique plus superficiel, le groupe des catéchols s'est révélé être un système complexe mais doté d'un potentiel considérable, en particulier si nous pouvions

parvenir à contrôler la tautomérisation du catéchol, une réaction rédox peut être déclenchée afin d'induire la transition de phase de réseaux auto-assemblés, un outil utile pour la conception de nanostructures. Pour ce faire, des recherches sur différentes surfaces métalliques, telles que le Pt et le Pd, peuvent s'avérer utiles pour bien comprendre le rôle de l'oxygène et du mécanisme rédox.

TABLE OF CONTENTS

LIST OF FIGURES

LIST OF TABLES

LIST OF ACRONYMS

2D – two-dimensional

3D – three-dimensional

CCM – Constant Current Mode

CHM – constant height mode

DHI - 5,6-Dihydroxyindole

DHICA - 5,6-Dihydroxyindole carboxylic acid

DOPA - L-3,4-dihydroxyphenylalanine

DNA – deoxyribonucleic acid

HOPG – Highly oriented pyrolytic graphite

MC – Monte Carlo

NFL – NanoFemtoLab

NB – Nucleobase

PES – Photoelectron spectroscopy

RNA – ribonucleic acid

RT – Room Temperature

SAM – self-assembled monolayers

SAMN – self-assembled molecular network

SPM – scanning probe microscopy

STM – scanning tunneling microscopy

STS – scanning tunneling spectroscopy

W-C – Watson-Crick

XPS – X-ray photoelectron spectroscopy

CHAPTER 1: INTRODUCTION

1.1 Finding inspiration in the natural world

Biological systems are able to produce a large variety of materials, whose elaborate structures possess incredible features and peculiarities. Among such natural masterworks are shells, pearls, wood, silk, bird beaks, antler and horns.[1, 2] In a similar way, we are made by a multitude of materials that possess extraordinary qualities, like bones, teeth, collagen and muscle fibre.[3] Those materials are not only complex, but highly organized, from the molecular level to the nanometric scale.[4] If we scale down to the cellular level, we can find macromolecular systems, such as hemoglobin, polymerases, membrane channels and ribosomes, that are tailored and engineered to carry out specific functions in the cells.

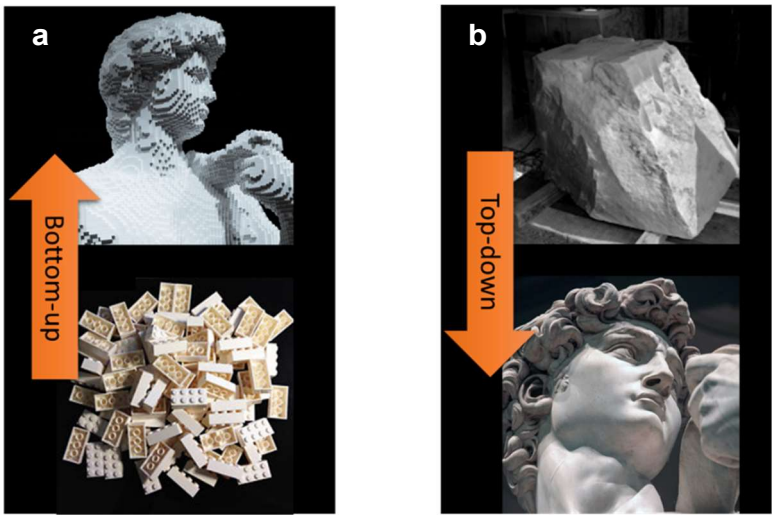

Figure 1.1: Graphical comparison of bottom-up and top-down approaches. a) Lego blocks put together to create a LEGO David[5], which resembles b) the Michelangelo masterpiece chiseled from marble.[6]

But how is it possible that nature is able to build such convoluted systems? Most biological systems show a strong prevalence for an approach which is commonly referred to as "bottom-up" design,[7, 8] where assemblies are built piece by piece (Figure 1.1a), often steered by the presence of a scaffold. Complex structures are thus achieved by stacking its very simple components together, rather than by removing material from a blank piece until the desired features and dimensions are obtained, as in "top-down" processes (Figure 1.1b). After billions of years of evolution, almost all biological systems share a common small set of building blocks (amino acids, nucleic acids and carbohydrates), that can be combined

to build an enormously diverse range of structures.[3] For example, it has been estimated that in the human body 10^5-10^6 different proteins (Figure 1.2),[9, 10] are formed under genetic control by ribosomes, all starting from a mere set of 20 amino acids. A variation in the amino acid sequence affects the final structure that the protein will take and its effect in the organism (Figure 1.2a).[11]

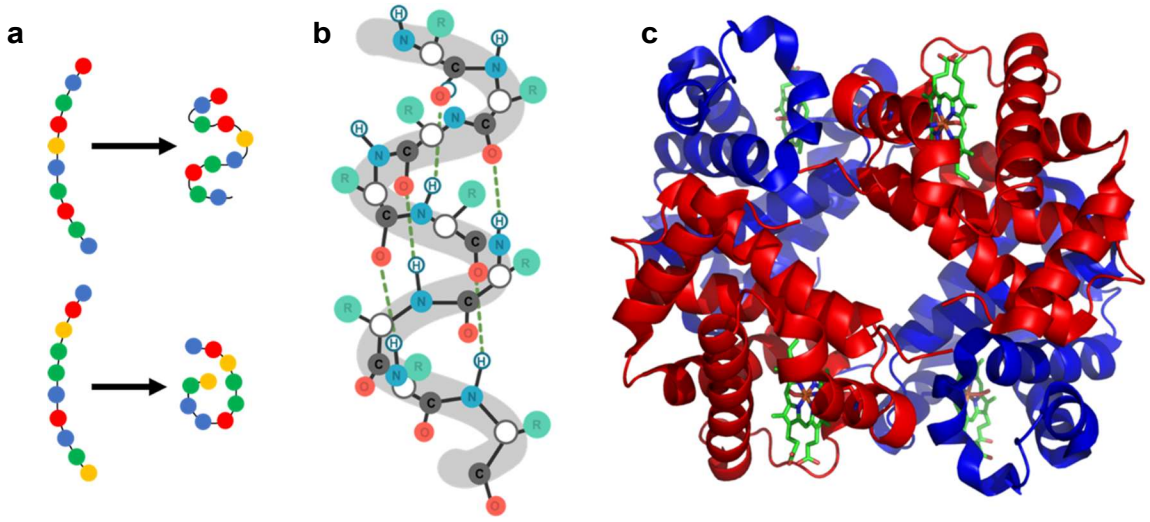

Figure 1.2: a) The specific sequence of amino acids in polypeptide chains determines the protein folded shape; b) Model of the intrachain non-covalent interactions between the amino acid units;[12] c) heamoglobin structure, formed by between two α (red) and two β (blue) subunits and heme groups (green).[13]

Most of the main bottom-up processes that occur in nature, from molecular to planetary scale, fall under the category of self-assembly, or autonomous organization of basic building components into larger patterns, without any external intervention.[14] This general definition for self-assembly is, however, quite loose,[15] and may generate confusion while grouping together several self-processes with different mechanisms, such as the formation of semiconductor quantum dots or the coordinated movement of fish schools. From a more rigorous material science point of view, it is then useful to use the term “molecular self-assembly”, thus referring only to processes that take place at the nanoscale.[16] Not straying far from the previous example, both the protein’s folding and aggregation processes fit perfectly this definition (Figure 1.2). To avoid confusion, from now on when talking about self-assembly, we will refer only to the molecular one.

Self-assembly is not limited to the spontaneous aggregation of molecules but includes the creation of refined materials and molecular machines. The process does not only have high precision, flexibility and error correction capacity, but is also self-sustaining and evolving. One of the classic examples, as well as the first macromolecular observation of self-

assembly in the biological world, came from the investigation of the tobacco mosaic virus (TMV).[17] The macromolecule structure of the virus is formed by an RNA strand, almost 6400 nucleotides, that is coated by 2130 protein subunits (each composed by 158 amino acid residues) assembled to form a single right-handed helix. It has been observed that the isolated protein and RNA strands of TMV self-assemble *in vitro* to form particles that are indistinguishable in shape and infectivity from the native virus.[18] The process follows two stages, with the coat proteins first self-assembling to form the disk subunits, each corresponding to two turns of the final helix structure (Figure 1.3), and then associating with the viral RNA to form the intact virus.[19, 20] The process of disk subassembly through reversible, noncovalent interactions allows the process of assembly and disassembly to be dynamic: each stage is at or close to equilibrium. This mechanism is therefore capable of undoing occasional errors that may occur during the assembly process. That is, the process can be regarded as intrinsically error-checking and error-correcting. The disk subunits assemble around the viral RNA in a more efficient manner than the stepwise growth of the helix, obtained by addition of single protein units.[14]

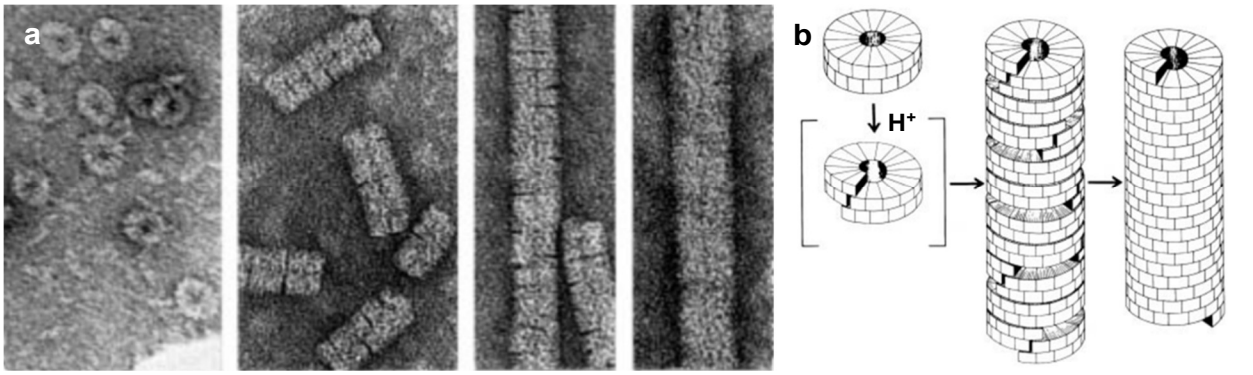

Figure 1.3: a) Electron micrographs of a TMV coat protein disk self-assembling into the α-helix structure; b) Schematic model of the self-assembly of TMV protein disk subunits into the virus. (figures adapted from Butler,[17] with permission of Royal Society)

Biomimicry – learning from and then emulating natural forms and processes, has helped pushing human innovation in several fields,[21] from advanced applications, such as lotus-inspired superhydrophobic surfaces (Figure 1.4a-b),[22, 23] to more mundane day-to-day ones, like Velcro straps whose shape is based on burdock's hooks (Figure 1.4c).[24] It is thus not surprising that biological self-assembly processes have provided a large source of interest and inspiration, especially in the field of nanotechnology, offering a promising bottom-up approach, both inexpensive and efficient, for the preparation of nanostructured materials.[3, 14, 25, 26]

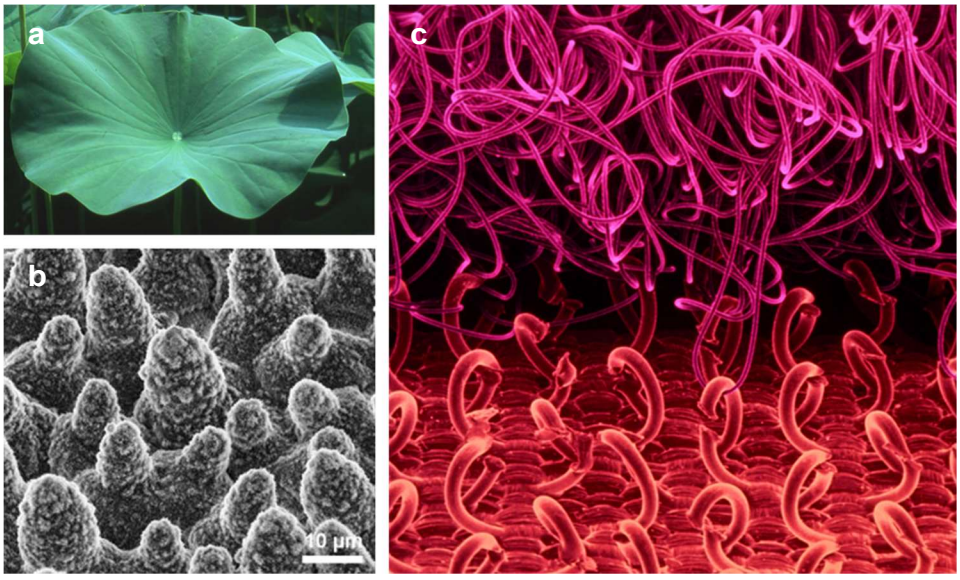

Figure 1.4: a) Lotus leaves exhibit superhydrophobicity due to their peculiar surface morphology, as highlighted by the b) scanning electron microscopy picture. (Figures adapted from Ensikat)[22]; c) Colorized scanning electron micrographic image of joined VELCRO®[27]

The possibilities opened by self-assembly may become the answer to comply to the ever-increasing demand for smaller features by Moore's empirical law. In fact, bottom-up approaches have a considerable advantage over top-down techniques, like lithography, since the smallest feature size is not constrained by any physical limit but depends only on the size of the molecular building blocks used.

An elegant (and successful) example of how biomimicry and self-assembly can be exploited to prepare nanostructures has been given by Rothemund in his work with deoxyribonucleic acid (DNA) origami, a versatile and simple method for folding a single strand of DNA into any shape (Figure 1.5).[28, 29] The DNA consists of two strands (an unbranched polymer) that are composed of four different nucleobases: adenine (A), thymine (T), guanine (G), and cytosine (C). The well-known DNA double helix is formed when the nucleobases sequence of the two strands match, *i.e.* when of the monomer form the canonical Watson–Crick (WC) hydrogen-bonded pair, G–C and A–T.[30] Instead, to produce his structures, Rothemund selected several short single strands of DNA, whose nucleobase sequence was chosen based on a software generated model in order to match specific sections of the main strand.[28] By exploiting the exquisite specificity of WC base pairing, each single strand of DNA thus directs the folding into the desired shape. This allowed the formation of shapes with 100 nm of diameter and spatial resolution of 6 nm, dimensions that are comparable to early results achieved using AFM and STM surface manipulation.

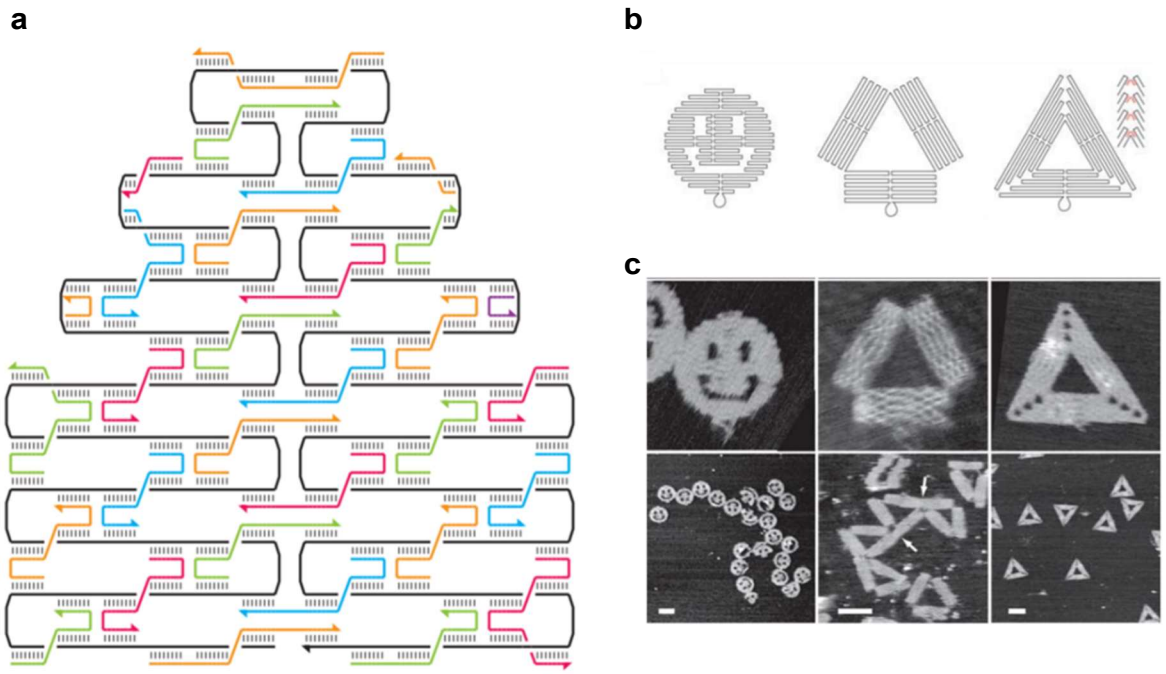

Figure 1.5: a) Design of a trapezoid DNA origami. The structure backbone is made from a long DNA strand (black). Shorter DNA strands (colored) bond to the main one to fold it into the desired shape. b) More complex designs of DNA origami c) atomic force microscopy image of scaffolded self-assembly. Top images are 165x165 nm, while the scale bar in the bottom ones corresponds to 100 nm (figures adapted from Rothemund, [28] with permission of Springer Nature).

While DNA origami may not have an immediate application, they represent a proof of concept for the intriguing possibilities made available by self-assembly. Nanoscale objects, such as molecules, quantum dots or nanotubes, can self-assemble to produce any kind of complex structures and aggregates useful for a number of different applications. A few examples would include micelles that may be used as drug delivery vehicles,[31] three-dimensional (3D) hydrogels with specific amino acid sequence that promotes cell growth[32, 33] or bioscaffolds that are used as tools for further nanofabrication.[34, 35]

1.2 The chemistry beyond the chemical bond

Although nature is able to almost effortlessly craft nanostructures using self-assembly approaches, it is still an open challenge to replicate the process in the laboratory and tailor it to our purpose. The improved understanding of the interactions that drive this organization, a topic that falls within the field of supramolecular chemistry, is pivotal to the development of self-assembly bottom-up protocols.[36] Rather than working on single molecules, supramolecular chemistry mainly focuses on the chemical systems made of a discrete number of assembled molecular subunits or components. The forces responsible for the spatial

organization of those systems include hydrogen bonding, metal coordination, hydrophobic forces, van der Waals forces, π-π interactions and electrostatic effects.[37] Thus, contrary to traditional chemistry which is centered mainly on covalent bonds, supramolecular chemistry specializes in non-covalent interactions.

The field of supramolecular chemistry has grown and matured since the term was introduced for the first time by Jean-Marie Lehn in 1978.[38] From host-guest systems to molecular machines, it represents nowadays one of the most investigated topics in chemistry. While the vast majority of studies involve solution phase or crystalline solids, of particular interest for the supramolecular chemist is the preparation of two-dimensional (2D) nanostructures.

The field of on-surface self-assembly, or 2D supramolecular chemistry, as the name suggest, focuses on what happens on a substrate, where molecular moieties can rearrange themselves to form periodic arrays called self-assembled monolayers (SAMs).[39] Multiple components contribute to the formation of such molecular arrangements: aside from the molecule-molecule interaction, the surface itself plays an important role, not only acting as a support/constrain and influencing the dimensionality of the self-assembled structure, but often driving the growth towards a structure that would not be obtained in solution due to its interplay with the adsorbate and the medium.[40]

While undeniably interesting, this is not the main advantage of having a substrate, which is instead related to the characterization methods that can be employed to investigate the samples. Diffraction techniques are commonly used for solid-state supramolecular chemistry, while more classical approaches (such as optical spectroscopies and nuclear magnetic resonance, NMR) are exploited for solution-phase investigation - which in both cases give indirect information from which the supramolecular structure has to be inferred (Figure 1.6a). On the contrary, scanning probe microscopy (SPM) techniques are available for investigating the samples deposited on surfaces, enabling the molecular (or even sub-molecular!) scale imaging of the self-assembled networks, and thus allowing to identify the molecular arrangements, an otherwise very difficult task to tackle with more traditional approaches (Figure 1.6b-c).[41] At the same time, large-scale images can be obtained in order to evaluate overall surface ordering and the presence of different domain orientations. These techniques can be both used in ultra-high vacuum conditions (UHV), a reduced complexity environment which allows to minimize the possible reactions of the adsorbate, or at the solution – solid interface, where it is possible to address the effect of solvent and concentration.

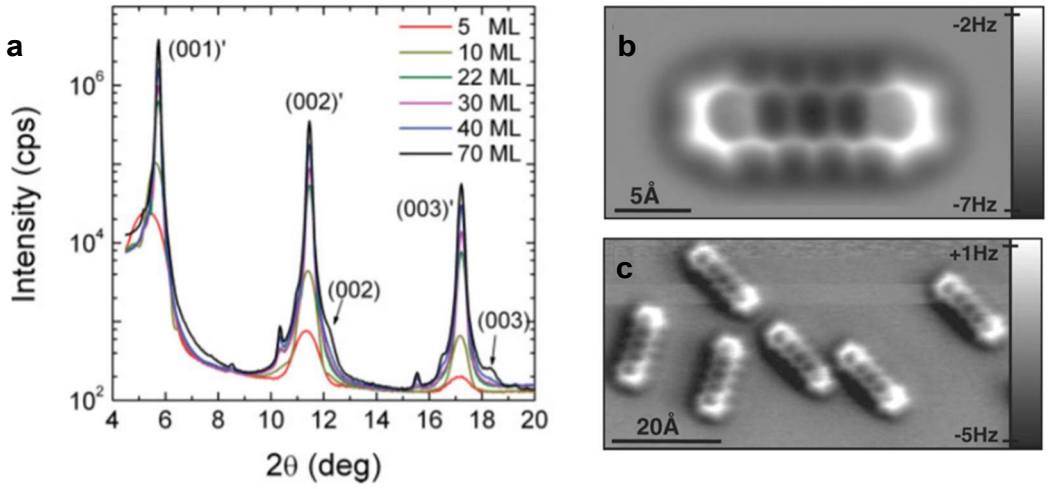

Figure 1.6: a) X-Ray Diffraction patterns of pentacene monolayers on SiO2 (figure reproduced from Brillante[42] with permission of American Physical Society); b, c) Constant-height atomic force microscopy images of pentacene on Cu(111) surface (figure adapted from Gross[41] with permission of the American Association for the Advancement of Science)

1.2.1 Basic principles of self-assembly on-surface

Before moving further to illustrate the capabilities of SPM by showing some important experimental results from the literature, it is useful to give more details on the molecular self-assembly on a surface and to take an in-depth look at the process to better understand which are the parameters that affect the process. As we have seen in the previous paragraphs, self-assembly is more than a mere "spontaneous" process. Interactions between the building blocks lead to the creation and destruction of bonds until equilibrium is achieved, thus enabling the creation of replicable and extended patterns that could even possess self-healing qualities. At the same time, if the system does not reach such equilibrium state, other structures may be still produced spontaneously which, in contrast, will not present a clear periodic arrangement. Such difference in the behaviour between these two cases is given by the ratio between surface diffusivity and molecular flux, as shown in Figure 1.7a.[43, 44] If such ratio is low, then it is easier for the molecule to be trapped in an unfavourable state due to a steric hindrance and thus not to be able to diffuse further. In this case, it is more correct to talk about "self-organization" rather than self-assembly, as the growth is kinetically driven.[40, 43] Instead, if the molecule diffusion on the surface is fast enough, the molecule can move freely, following the free-energy minimization until a thermodynamically favoured position is achieved.

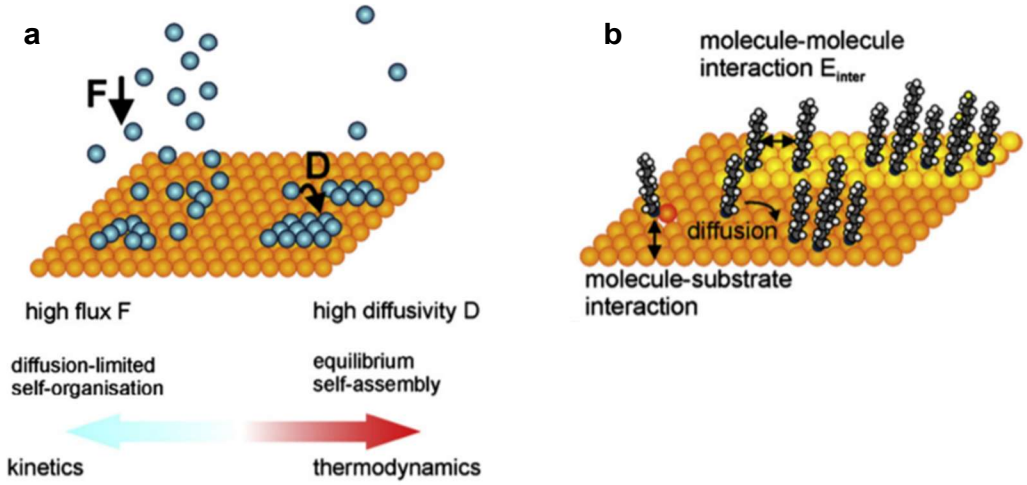

Figure 1.7: Schematic illustrating the different conditions leading to self-organisation versus self-assembly b) the different energy contributions to self-assembly. (figures are adapted from Kühnle,[43] with permission of Elsevier)

The formation of a particular self-assembled pattern on a surface depends thus on the balance between different energy contributions (Figure 1.7b). In order for the molecule to diffuse on a surface, it has to possess kinetic energy $E_{kin,}$ higher than the barrier E_{diff}. While this is not true for all the systems at room temperature, especially when considering larger building blocks, most of the STM apparatus include also a heating system, which allows to anneal the sample. Thermal energy is thus transferred from the substrate to the adsorbed molecules, and the diffusion barrier is readily overcome. On another note, substrate temperature cannot be endlessly increased, otherwise the molecule may gain enough E_{kin} to overcome the adsorption energy E_{ads} and desorb.

The last energetic term to take into consideration is given by the intermolecular interaction energy E_{inter}. Covalent bonds are very rare in self-assembly process, because their higher energy makes them almost irreversible: the building block may thus get trapped in an unfavourable conformation, similarly to what happens in self-organizing processes. Weak bonds, such as the ones created by non-covalent interactions, are instead reversible, and may be broken and reformed until the lower equilibrium position is achieved. While such non-covalent interactions are ubiquitously present in self-assembly, they are not a necessary condition. Some notable systems involve covalent bonds as well, like the sulfur-gold bonds of alkanethiols on Au(111), which is regarded as the archetypical self-assembled monolayers (SAMs) system.[45]

Regardless of the interaction nature, the formed bonds, however, have to be strong enough to be stable, thus E_{inter} has to be higher than E_{kin}, but still of the same order of

magnitude to ensure reversibility. Hence, we can put in order the different energy contribution for a self-assembly process as $E_{diff} < E_{kin} < E_{inter} < E_{ads}$.

Surfaces represent thus a unique playground,[40] and the rules that govern the 3D systems in solution or solid-state should not be taken for granted. The spatial confinement to 2D adds additional constraints, in some cases forbidding the formation of particular bonding configuration due to steric hindrance. Moreover, once the molecular precursor adsorbs on a substrate, the formation of chiral domains is not uncommon, even if the molecule itself is achiral.[46, 47] Lastly, the presence of a substrate may act as a catalyst and trigger chemical modification in the molecular precursor's functional group.[48]

1.2.2 Types of non-covalent bonds and functional groups

As the bond reversibility is a fundamental characteristic of self-assembly processes, it is clear that non-covalent interactions play a leading role in the process. The most common types of non-covalent bonds and interactions that are present in self-assembling systems are summarized in Table 1.1, along with their energy, distance and salient features. [40]

Table 1.1: Classification of the principal interactions in 2D self-assembly, along with the with associated energy and typical bonding distances.[40]

	Energy range	Distance	Character
Adsorption	0.5–10 eV	≈ 1.5–3 Å	Directional, site selective
Surface migration	0.05–3 eV	≈ 2.5–4 Å	1D / 2D
Van der Waals	0.02–0.1 eV	< 1 nm	Nonselective
Hydrogen bonding	0.05–0.7 eV	≈1.5–3.5 Å	Selective, directional
Electrostatic ionic	0.05–2.5 eV	Long range	Nonselective
Metal-ligand interactions	0.5–2 eV	≈1.5–2.5 Å	Selective, directional

Regardless of the system, Van der Waals forces have to be considered as omnipresent, both in the molecule-surface interactions and intermolecular ones. A notable example is given by the strong adsorption between alkyl chains and highly oriented pyrolytic graphite (HOPG). Due to the intermolecular van der Waals interaction, the alkyls chains ar e close-packed between each other, forming lamellar structures (Figure 1.8a).[49] This has been exploited for the designed molecular precursor with alkyl functionalities that would interdigitate between each other, allowing the creation of porous network that can be used as host-guest system (Figure 1.8b-c).[39, 50] On the other hand, because of the weakness

and non-selective nature of van der Waals forces, it is hard to understand *a priori* their contribution to the process and to design molecular precursors.[36, 51]

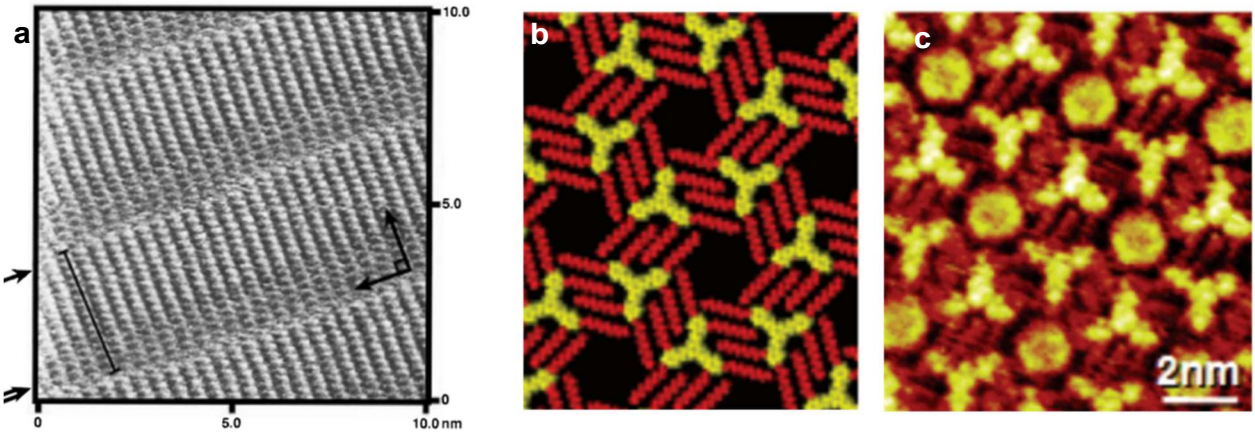

Figure 1.8: a) STM image of ordered rows of triacontane phenyloctane/graphite. Black bar marks one molecular length. (figure reproduced from Cyr,[49] with permission of American Chemical Society) b) model for the supramolecular host matrix of 1,3,5-tris[(E)-2-(3,5-didecyloxyphenyl)-ethenyl]-benzene, and c) STM images of the same matrix filled with a hexabenzocoronene molecule (figures adapted from Schull,[50] with permission of American Chemical Society)

The effect of hydrogen bonds, on the contrary, is way more evident. Hydrogen bonding is a specific interaction between a positively polarized hydrogen that is covalently bonded to an electronegative atom of an H-bond donor molecule and a negatively polarized atom of an H-bond acceptor molecule.[52] The main feature is, however, its directionality, which along its strength makes building blocks based on hydrogen bonding very appealing for the tailoring and design of nanostructures. Carboxylic acids are representative of this category and have been widely applied as connections in supramolecular network due to their well-known predisposition to form strong hydrogen bonds.[52, 53] In fact, trimesic acid (TMA) and its derivative have been largely investigated on the 2D surfaces. After deposition on HOPG in UHV conditions, STM images shows that TMA forms the common carboxylic dimers and self-assembles into a honeycomb arrangement forming porous structures, called “chickenwire” (Figure 1.9a). On the other hand, it is possible to obtain an additional pattern, often referred to as “flower”, with three carboxylic acid bonding together (Figure 1.9b).[54] The phase transition is triggered by increased molecular coverage, that forces the molecule to maximize the energy gained through adsorbate–substrate interactions, or by the interaction with the different solvent.[54-56]

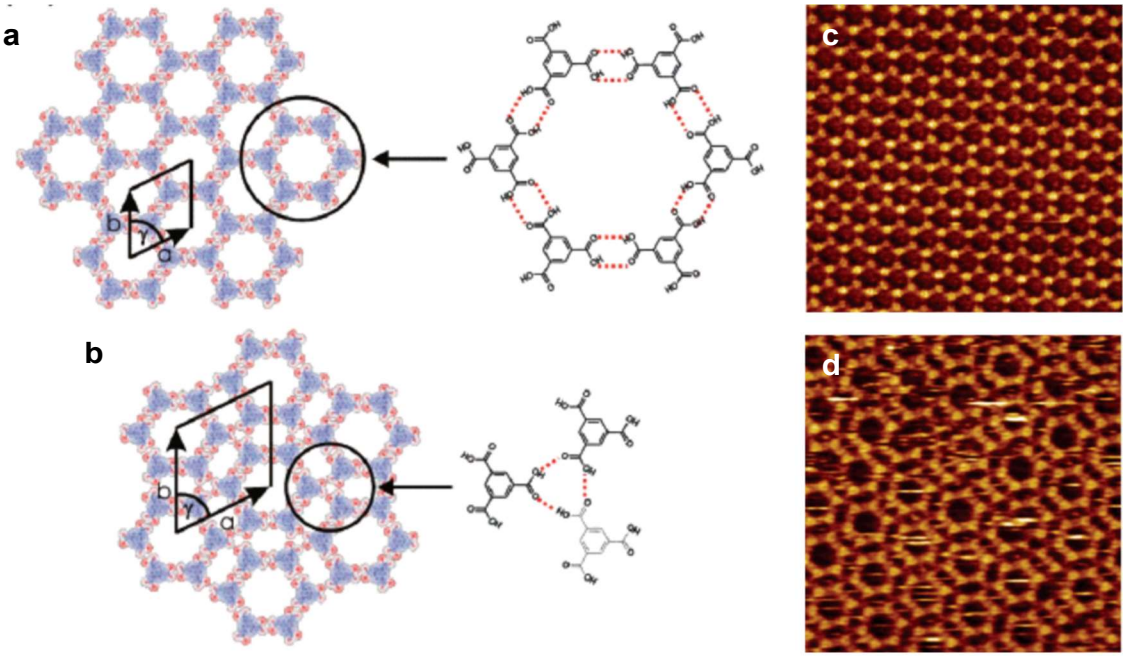

Figure 1.9: a) chickenwire and b) flower TMA structure models with their corresponding hydrogen-bonding scheme; 15×15 nm constant current STM images for c) trimesic acid TMA at the heptanoic acid/HOPG interface, forming a chickenwire structure, and d) at the pentanoic acid/HOPG interface, forming instead a flower structure. (figure adapted from Lackinger,[54] with permission of American Chemical Society)

Generally speaking, however, the adsorption geometry and molecular arrangement of self-assembled networks are determined by the chosen surface, since molecule-substrate interactions are much stronger than the molecule-molecule ones. On the other hand, the proper choice of substrate may reverse this paradigm. On surfaces such as Au(111), Ag/Si(111) or HOPG, which are not reactive and present smaller potential corrugation, the resulting self-assembled networks are commonly driven by intermolecular interactions. Even in these cases, however, the substrate influence is never negligible, and even small variation in the substrate reconstruction has a tangible effect in the supramolecular architecture of the adsorbates.[57]

1.3 Scanning Tunneling microscopy applied to biochemistry

One of the most interesting SPM apparatus is, without a doubt, the scanning tunneling microscope (STM). In 30 years since its invention, high-quality commercially available STM instruments are wide-spread, and cutting-edge technologies were developed to improve their range of applications. Similar to other SPM techniques, the STM can routinely obtain sub-molecular resolution imaging of isolated molecules and supramolecular networks on a surface as long as it is provided with a sufficiently sharp tip. Even though the

resulting STM image is the convolution of the surface density of states and morphology, an expert user is able to quickly identify molecular features and infer the network structure by comparison with simpler model systems. Moreover, the imaging can be supported by density functional theory (DFT) simulation or Monte Carlo (MC) modelling to strengthen the interpretation of the acquired experimental data. Data acquisition can also be modulated by varying operation parameters: for example, changing bias polarity allows to investigate both filled and empty states of the surface. Proper selection of bias voltage (V_t) and tunnelling current (I_t) allows the imaging of different molecular orbitals.[58] Scanner movement can be stopped in order to perform spectroscopy measurements, the most common being the sampling of the local density of states (LDOS) by recording (dI/dV)/(I/V) curves, also known as scanning tunnelling spectroscopy (STS).

STM has become the method of choice for the characterization of supramolecular 2D networks, as it allows to answer to fundamental questions of supramolecular chemistry and surface science, as well as assisting the development of novel nanomaterials. At the same time, the ability to probe biological processes at the nanoscale, such as cell recognition and signalling, is an intriguing opportunity, as it would allow to gain important insights on the interactions of small biomolecules that can in turn be exploited for nanotechnological applications such as biosensors and biocompatibility of implants.[59, 60]

An excellent example of the multidisciplinary appeal of STM is well portrayed in the self-assembly of nucleobases on gold surface. The interactions that are behind the specificity of WC pair are of fundamental importance for the proper execution of DNA replication, as well as the driving force for the polymerization of the very first oligonucleotide – hence, the origin of life. However, in order to better understand the complementarity between nucleobases (NBs), all the different contributions (hydrogen bonding, solvation energy, and hydrophobic and van der Waals interactions) had to be determined separately, which is a very demanding experimental task. The pioneering work done by the groups of Heckl on HOPG and MoS_2 and by Besenbacher on Au(111) have permitted the visualization of the bonding configuration of these nucleobases, as well as confirming that their self-assembly is not limited to WC-type interactions.[61, 62] In the following paragraphs, we will present a small review of the NB self-assembly on surface, as we want to emphasize how the characterization of these systems in an ideal environment, far from the real biological condition, can provide useful insights to the development of supramolecular chemistry and biology.

Among nucleobases, guanine is the most interesting and versatile because of the combination of donor and acceptor sites given by the multiple amine, carbonyl and imine groups

(Figure 1.10). This is reflected in the hydrogen bonded ribbon-like structure that guanine adopts either in solid or solution phase (Figure 1.10a).[62] Moreover, in the presence of certain metal ions in solution, quartet-based architectures stabilized by metal coordination bonds are possible (Figure 1.10b).[62]

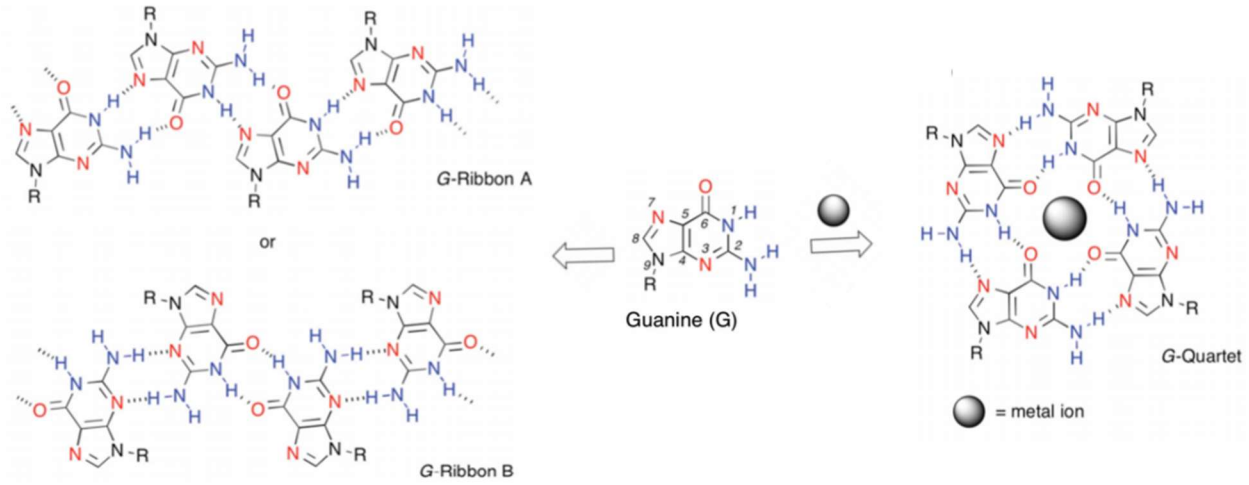

Figure 1.10: Chemical structure of guanine and examples of its hydrogen bonded self-assembled structures in solution: a) ribbon-like structures and b) quartet templated by the metal ion. Hydrogen-bonding donor and acceptor sites are indicated in blue and red, respectively. (figure adapted from Ciesielski,[62] with the permission of John Wiley and Sons)

Once on the surface, the self-assembly process proceeds on a different pathway, and is driven mainly by the chosen substrate. On both HOPG and MoS_2, guanine forms a close packed ribbon structure, mainly stabilized by cyclic N–H···O and N–H···N bonds, which reminds of the ribbon structure shown previously (Figure 1.11a).[63]

Instead, on the Au(111) surface, the molecule self-assembles into large 2D square structures (Figure 1.11b-c).[64, 65] Analysis of the STM images shows that the networks are formed by enantiomerically pure guanine quartets, without the presence of any metal coordination. When annealed at 400K, the quartet structure rearranges to form the same ribbon structures obtained on MoS_2 and HOPG, thus showing that the quartet is not the most thermodynamic favourable conformation for guanine on Au(111). Nevertheless, the quartet structure still forms at room temperature, so it has to be kinetically favoured. Otero has shown that due to the increased charge perturbation the same hydrogen bonds are much more stable in the quartet configuration with respect to dimer/trimer one.[64] This effect, called resonance-assisted hydrogen bonding, enhance the lifetime of the quartet structure, and is decisive for the creation the room temperature guanine phase as well for most of the WC base pairs.

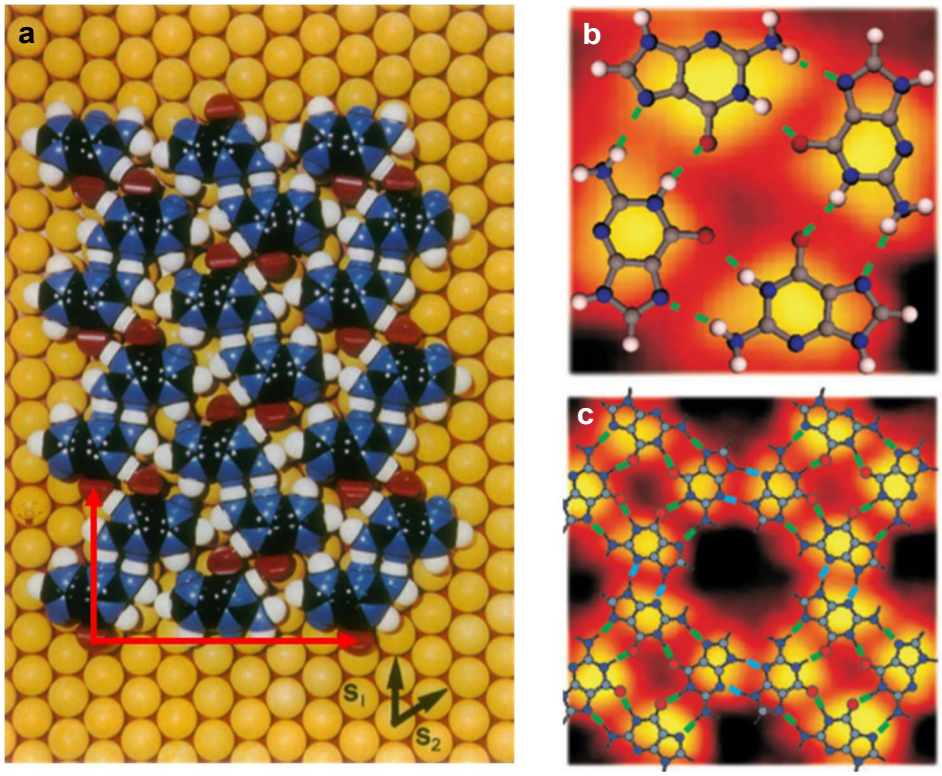

Figure 1.11: a) Guanine ribbon close packed structure on MoS_2; S_1 and S_2 are the substrate lattice vectors, 3.16 A long. The unit cell (red) of the guanine lattice is a = $3.5s_1$ and similarly b = $-3s_1 + 7s_2$ (figure reported from Heckle[56]); . b-c) A close-up STM image of the L guanine-quartet network superimposed with a theoretical molecular model. (figure adapted from Xu,[65] with permission of John Wiley and Sons).

The analysis of the molecular features from the STM images is not always a straightforward process. Multiple isoenergetic configurations are often possible, making the identification of the self-assembled structure challenging. Due to the nearly round shape of the molecule, adenine may form maximum two hydrogen bonds with each of its neighbours. On the other hand, the small dimension of the molecule allows for more than 20 possible bonding conformations.[66] On surfaces like HOPG, Au(111) and MoS_2, where the interaction between the molecule and the substrate is weak, adenine self-assembles into very close packed networks, which make the unambiguous identification of the structure very complicated (Figure 1.12a-d).[61, 67, 68] By comparison of the intermolecular feature spacings, obtained by the STM experimental results and the ab initio calculated values it is, however, possible to distinguish which of the many possible adenine monolayers accounts for the observed structure.[69] This ambiguity is lost in the case of the more reactive Cu(110) surface, where long dimer chains coexist with other extended 2D phases instead (Figure 1.12e,f).[70] The one-dimensional structures are created by strong interaction between adenine's amino group and the surface itself, which forces the

molecules to adopt a tilted adsorption configuration and prevents further hydrogen bonding.[70]

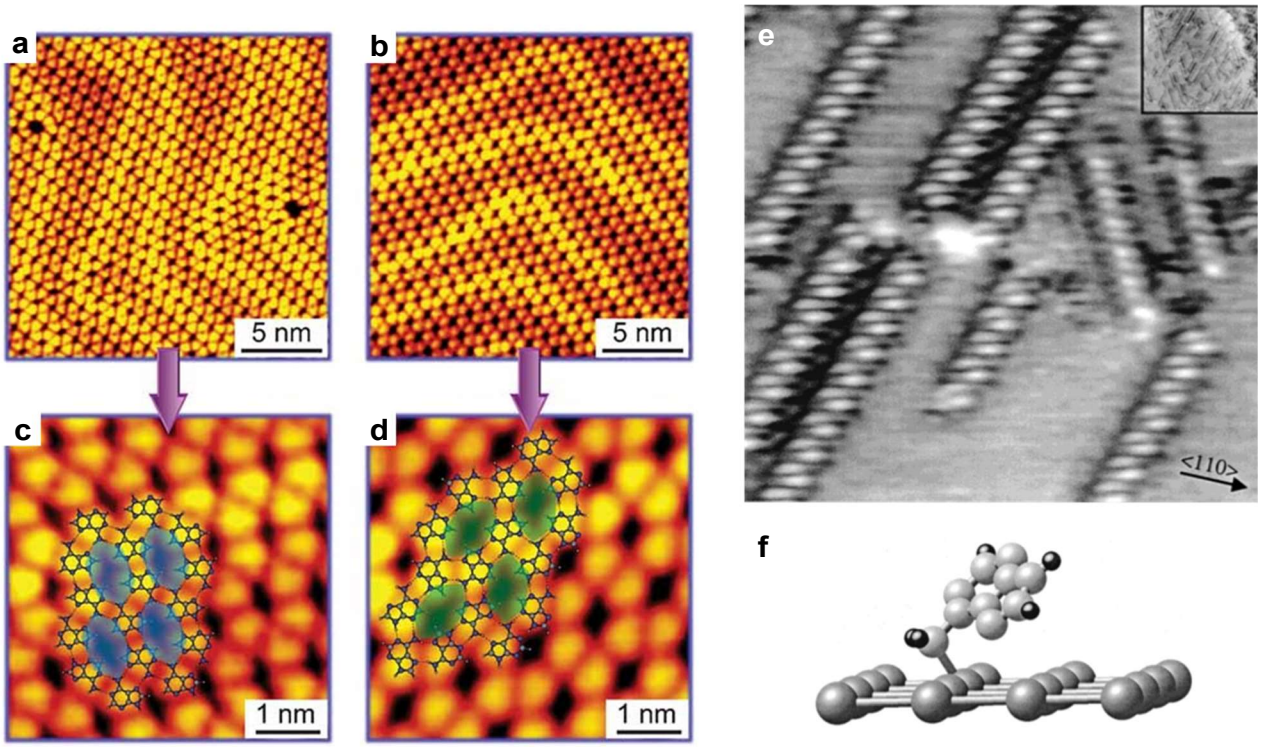

Figure 1.12: a-d) Experimental STM images of adenine monolayers on the Au(111) surface. Theoretical models for each phase are superimposed on the images in c and d. (figure reproduced from Kelly, [68] with permission of John Wiley and Sons). e) 10×10 nm STM image of adenine on Cu110, along with a f) model for its optimized adsorption structure (figure adapted from Chen,[70] with permission of American Chemical Society.

While these results may suggest that all the molecular precursor self-assemble in nicely packed 2D networks, this is far from true. Of course, the surface scientist has some tricks at his disposal: the molecular coverage can be increased, thus reducing the lattice sites available for diffusion, or the surface temperature can be varied in order to decrease diffusion. Nevertheless, not all the molecules are able to form periodic 2D structures: for example, cytosine forms disordered molecular network of 1D ribbons interconnected by five- and sixfold rings, a random arrangement that depends on the surface coverage (Figure 1.13a).[71, 72]

Nevertheless, the lack of long-range order does not mean that no useful information can be gained. Provided with the knowledge of the behaviour of the single NBs on the Au(111) surface, Otero et al. investigated the co-deposition of both complementary (C-G) and non-complementary (C-A) pairs of nucleobases and gained some constructive insights on the nature of the WC interactions.[73] Guanine or adenine were deposited over the cytosine

ribbon structure at RT, producing two different assemblies. Co-deposition of the complementary base guanine produced a binary nucleobase mixture with an increase in the number of fivefold rings, which are stable even after the sample was annealed at 370K (Figure 1.13b-c)

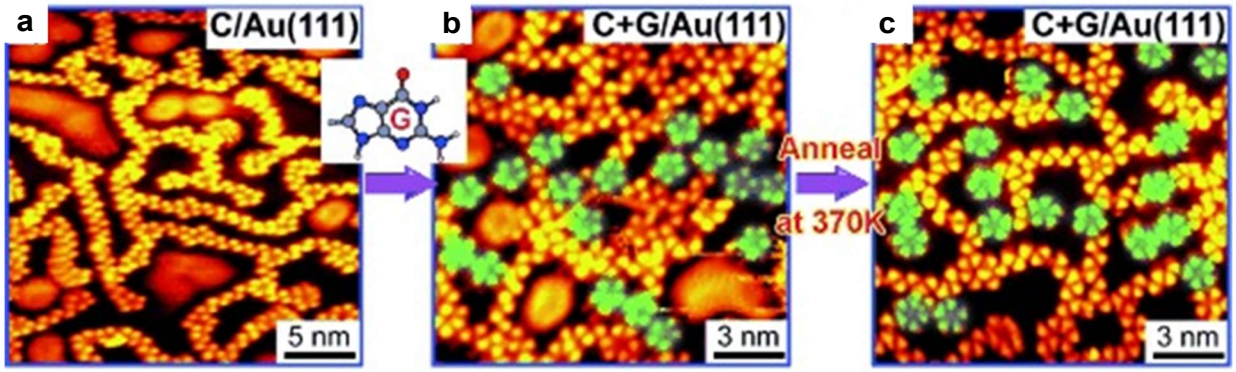

Figure 1.13: a) As-prepared self-assembled cytosine ribbons on Au(111). b) Fivefold rings appear over the surface after co-deposition of guanine on the cytosine C) after annealing, the C=G structure remains disordered. (figures adapted from Otero,[73] with permission of John Wiley and Sons)

No significant change was observed in the disordered cytosine ribbon structure when non-complementary base adenine was used instead (Figure 1.14a-b). Once again, the base mixture was heated, but this time the annealing step triggered a phase transition, and the formation of separated domains of adenine and cytosine. This result suggested that upon guanine deposition, stable C-G pairs are formed, which self-assemble in the ring structures. On the other hand, no C-A structure was formed, and as thermal annealing gave enough energy to overcome the diffusion barrier, the two components are segregated into different phases.

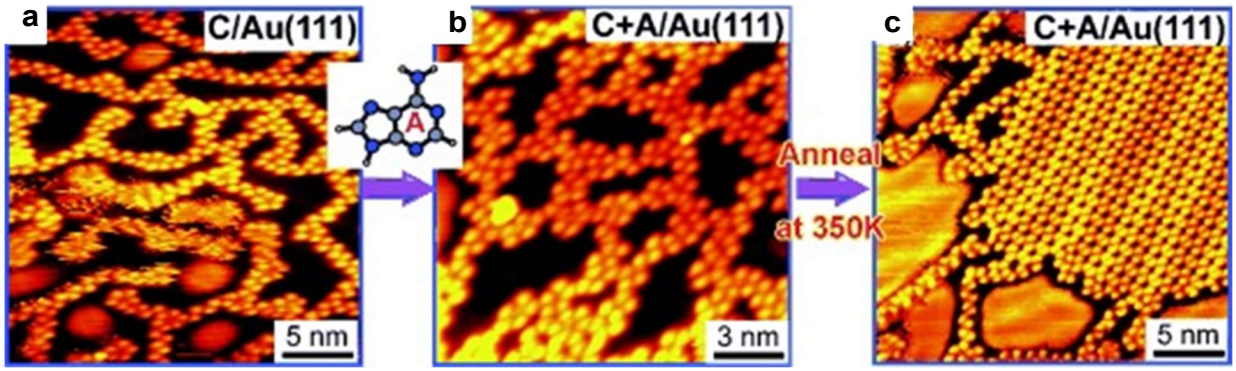

Figure 1.14: a) as-prepared self-assembled cytosine ribbons on Au(111). b) the fivefold rings do not appear after the codéposition of adenine. c) after heating, the noncomplementary C+A mixture segregates into adenine islands and cytosine zigzag branches (figure adapted from Otero,[73] with permission of John Wiley and Sons).

This result suggests that the DNA sugar ring backbone may not be a necessary prerequisite for the formation of WC pairs, and that surfaces may trigger recognition between complementary bases. The formed base pairs may have stacked on each other, and act as a catalyst for the synthesis of a covalent backbone, which would be a prerequisite for the emergence of the first primitive form of replication and have thus played an important role in the creation of life.[73, 74]

1.4 Eumelanin

The properties of a particular cellular component, as well as its role in complex biological systems, are ultimately determined by its supramolecular structure. In turn, the 3D shape adopted by a macromolecule is governed by the interactions between its monomeric units. Hence, it is no wonder that a great deal of effort has been devoted to determine atomic-resolution structure of most of the biologically relevant macromolecules, such as carbohydrates, lipids, proteins, and nucleic acid, either by single-crystal X-ray diffraction or by NMR, performed in solution. Despite these large efforts, there's a compound that has managed to elude its complete characterization and still presents an intriguing challenge: eumelanin.

As the name suggest, eumelanin is one of the melanin pigments, a class of bio-functional macromolecules present in most of the biosphere. It is very abundant in the human body where, together with pheomelanin, it determines the variation of colour for skin, eye and hair.[75] Eumelanin functions are not only related to esthetical appearance, but it is also an important photoprotectant, and it may be involved in the development of melanoma skin cancer.[76, 77] Investigation of melanin pigments has been so centred on eumelanin that the two terms are often used interchangeably.

Eumelanin's structure, on the other hand, is still under debate. Being insoluble in the most common solvents as well as opaque, the only standard structural approaches applicable are X-ray and neutron scattering, which however fail to fully characterise eumelanin due to his high chemical heterogeneity.

1.4.1 Eumelanin optoelectronic properties

As a result of the rising trend of biomaterials' applications,[78, 79] eumelanin has recently become the focus of a renewed wave of interest.[80, 81]

It is in fact know from the early studies of McGinnes in 1970 that eumelanin is able to conduct electricity in the solid phase, but unlike other biological materials it presented an electronic behaviour more akin to disordered inorganic systems.[82] It is observed that by increasing the applied voltage to a eumelanin pellet, the current increases monotonically, until it reaches a threshold voltage V_T, after which a sudden increase in current and a drop in voltage takes place (Figure 1.15a). The negative resistance region is obtained during the switching, and it is due to the load line resistance.

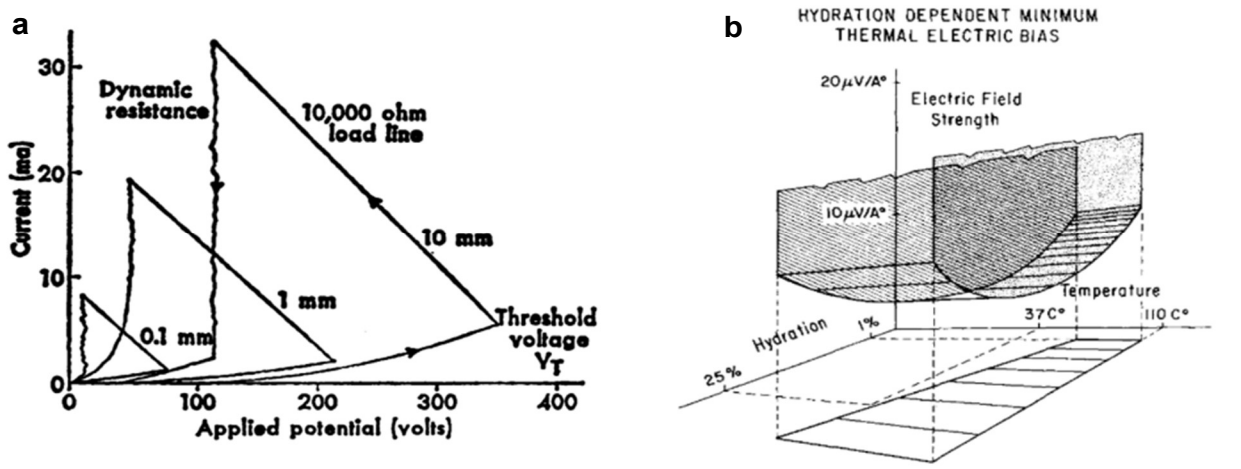

Figure 1.15: Current-voltage properties of melanin prepared by autoxidation of Ldopa for various sample thicknesses; (figure reproduced from McGinness,[82] with the permission of the American Association for the Advancement of Science) b) The minimum temperature and electric field required to produce the on state depend on the hydration The on state can only be produced within the shaded region for a 0.1-sec pulse. (figure reproduced from Filatovs[83], with the permission of John Wiley and Sons)

After switching, the I/V plot instead follows a new curve characteristic of this low resistance state, producing the triangular plot in Figure 1.15a. This phenomenon, often referred to as "threshold switching", is very uncommon, and has been mainly reported for thin amorphous materials and chalcogenide glasses.[84] In this "on" state the conductivity of eumelanin is increased by a factor of 10^2-10^3 at a relatively low voltage, compared to other inorganic materials.[82] Further investigation also noted that the switching behaviour of the eumelanin can also be enhanced by hydration state,[82] or by the sample temperature (Figure 1.15b).[83] Meanwhile, other studies evidenced that eumelanin presented a pseudomemory effect, such as the sample remained in the "on" state even after applied bias was removed.[85]

The potential applications of eumelanin are, however, not limited to its conductive properties. In fact, eumelanin possesses a broad-band monotonic light absorption, as

shown in Figure 1.16, which can be fitted to a simple exponential. Once again, this characteristic is atypical, especially when compared to other organic materials, since it does not present any feature that could be assigned to chromophore groups.[86] While it may be convenient to point at the polymer's poor solubility, investigations by Riesz ruled it out, as they show that scattering accounts only for the 6% of the total optical attenuation.[87] Moreover, in agreement with its biological role as photoprotector, it presents strong non-radiative relaxation of photo-excited electronic states, *i.e.* can deactivate UV and visible photon energy with high efficiency.[88]

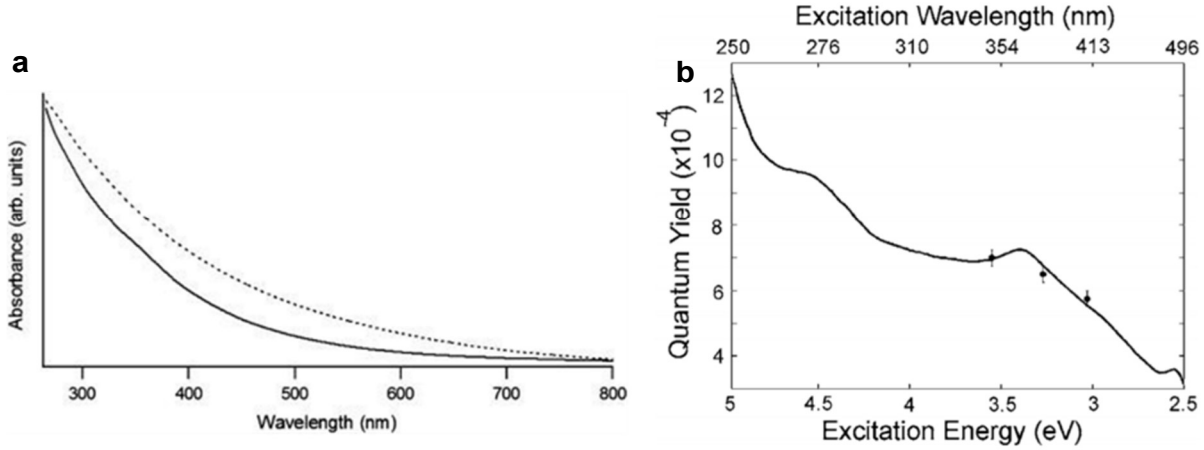

Figure 1.16: Characteristic broadband absorbance of eumelanin (dashed line) and pheomelanin (solid line). (figure reproduced from Tran,[89] with permission of Elsevier) b) Eumelanin quantum yield as a function of excitation energy across UV and visible wavelengths (figure reproduced from Nighswander-Rempel,[90] with permission of AIP publishing.

1.4.2 Eumelanin structure

Despite such interest over eumelanin properties and the extensive experimental investigations, [91] there is not yet consensus over eumelanin structure and aggregation behaviour.

At the molecular level, it is generally agreed that eumelanin is a combination of 5,6-dihydroxyindole (DHI, Figure 1.17a) and 5,6-dihydroxyindole-2-carboxylic acid (DHICA, Figure 1.17b), which are present in all their various redox forms: ortho-hydroquinone (HQ, Figure 1.17a), -semiquinone (SQ, , Figure 1.17d), and -(indole)quinone (IQ, Figure 1.17c) form.

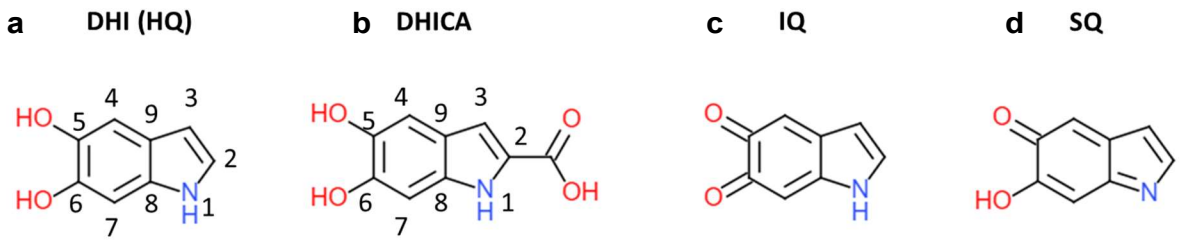

Figure 1.17: DHI, DHICA and its different redox states.

The bio-synthesis of both eumelanin and pheomelanin is analogous to the oxidative conversion of catecholamine to aminochromes.[92] The process, called melanogenesis, is described by the Raper–Mason pathway (Figure 1.18).[93] The first step is triggered by the bifunctional enzyme tyrosine, which converts L-tyrosine and L-3,4-dihydroxyphenylalanine (L-DOPA) into L-dopaquinone. From there, the chemical pathway splits, as the combination of the products with L-cysteine leads to the formation of pheomelanin. The formation of eumelanin instead involves the intramolecular cyclization of L-dopaquinone, followed by a redox exchange with dopaquinone, that gives L-dopachrome and L-DOPA. The red coloured dopachrome is then mainly decarboxylated to 5,6-dihydroxyindole (DHI), or rearranged as 5,6-dihydroxy indole-2-carboxylic acid (DHICA) as the minor product. These two indoles are then further oxidized and polymerized to produce eumelanin. It is interesting to notice that just the two first steps are catalysed by tyrosinase, while the successive steps proceed spontaneously. In fact, if DHI is exposed to air, or to alkaline solution, it quickly forms a dark insoluble polymer and precipitates. DHICA follows a similar process, but it is much slower and gives a dark brown solution which does not precipitate.[94]

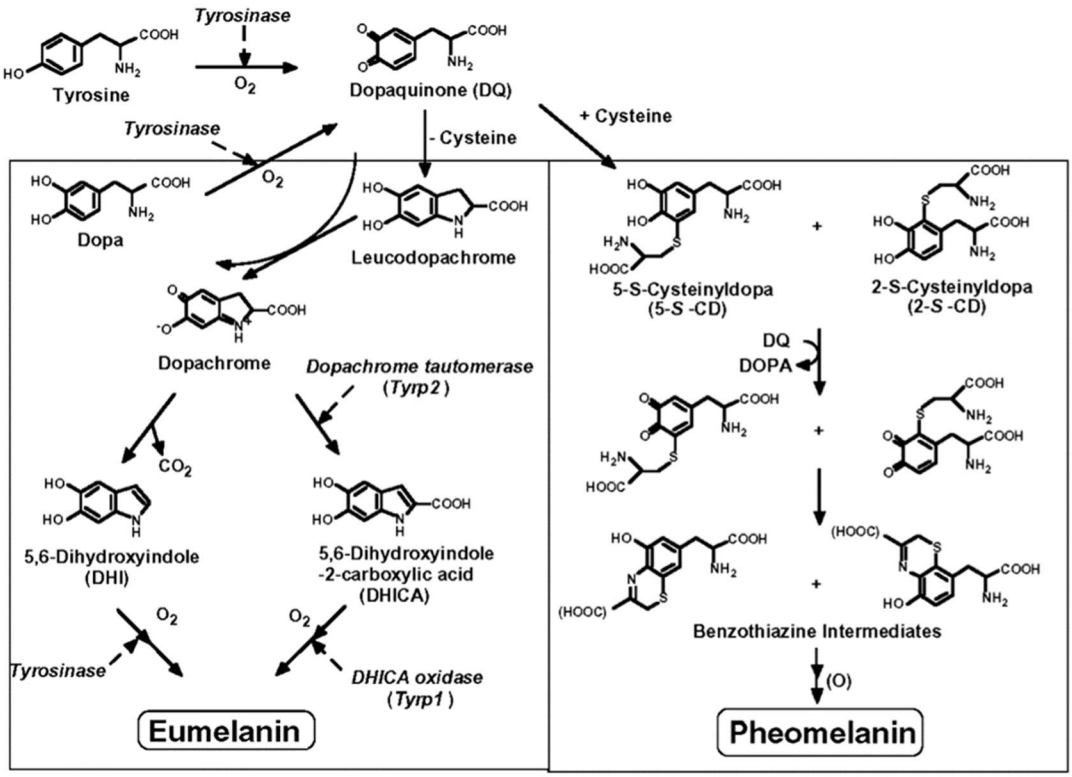

Figure 1.18: Raper-Mason cycle for the biosynthesis of Eumelanin and Pheomelanin (figure reproduced from Wakamatsu,[95] with the permission from John Wiley and Sons)

As we move away from the single monomers and try to look at the supramolecular level, it becomes significantly harder to describe eumelanin structure. Aside from the difficulties associated with the determination of the DHI/DHICA ratio,[76, 95] the monomeric units possess a large number of possible bonding configurations. In fact, the analysis of either natural eumelanin isolated from sepia ink[96] or the ones produced from the oxidative reaction of precursors[97] present a collection of dimers and trimers. In particular, DHI dimers present preferential 2,4'- and 2,7'-bondings, while for DHICA the 4-4' and 4-7' conformations are preferred due to the presence of the carboxylic acid in position 2.[98, 99] Furthermore, eumelanin may contain uncyclized units and overall composition varies based on the substrate and oxidation conditions.[76]

Due to this rather intricate structure, eumelanin has historically been described as a highly conjugated and extended heteropolymer. Such model, called "amorphous semiconductor" to follow Mott-Davis formalism,[100, 101] would point at eumelanin chemical heterogenicity to explain its uncommon properties, such as the conduction behaviour and the experimental broadband absorption. On the other hand, it does not explain the humidity dependence, and started to be questioned in the past years.[102]

A radical change of perspective on eumelanin structure has gained ground in the past years, which suggests that eumelanin is a large extended structure, but rather formed of small oligomers, less than 10 monomeric units, held together by non-covalent and aromatic interactions to form nanoaggregates in a graphitic-like structure. In the latter instance eumelanin would be still amorphous yet made of hierarchical structures. Such "chemical disorder" model is supported by quantum chemical simulations studies, which have shown that the featureless absorption spectra can be obtained by the convolution of non-homogeneously broadened Gaussian transitions associated with each of the components of the eumelanin ensemble.[89, 103-105] Moreover, initial proof of the eumelanin sub-molecule has been gained by X-Ray scattering and SPM analysis.[106-108]

1.5 Thesis statement and structure

So far, there is still too little direct evidence to support the chemical disorder model, as well as any supramolecular organisation in eumelanin.[109] Within this thesis we thus try to tackle the problem by taking a bottom-up approach for the investigation of eumelanin structure. Instead of starting from the complicated structure of a full formed eumelanin polymer, we plan to observe its monomers in a reduced complexity environment by taking advantage of UHV. Once deposited on a surface, the eumelanin precursors form self-assembled networks that are going to be characterized by STM in order to better understand the interactions that govern the molecules aggregation. Small molecules with low functionalization such as the indole moieties a useful model system to evaluate the effect of different functional group. Furthermore, the controlled UHV environment allows us to study the possible progressive polymerization of the precursors, elucidating the bond conformation as well as evaluating the effect of the different oxidation state of the catechol group on the self-assembled structure. Complementary analysis by XPS will help monitor the molecule oxidation state and how it is affected by the chosen substrate and surface temperature.

The experimental work contained in this thesis is divided into three chapters, each focusing on a different molecular moiety with increasing complexity. The investigation on I2CA and DHI in chapter 3 and 4 provides the necessary background to fully understand how carboxylic acid and catechol groups contribute to the self-assembly of indoles. The interplay between these two functional groups is then observed in chapter 5, where the polymorphism of DHICA on Au(111) is studied.

Chapter 1

• Introduction to the concepts of bottom-up approach, self-assembly and supramolecular chemistry. A short review of literature on STM characterization of nucleobases is presented to give an example of how 2D assembly can be used to study complex, biologically relevant systems, as well as a presentation of eumelanin properties and structure. A list of the common acronyms and symbols is introduced in Appendix A.

Chapter 2

• Dedicated to the experimental technique used to accomplish the work presented in this thesis. Fundaments of STM and XPS theory are presented, as well as a more detailed description of the instruments. Some space is given to the description of the UHV system and the procedures for cleaning the surfaces and to the sublimation of organic material.

Chapter 3

• This is the first of three chapters in which the original results of my work are presented. It is devoted to the investigation of I2CA, which is used as a simple model system to investigate the self-assembling properties of indoles.

Chapter 4

• The second experimental chapter involves the characterization of the self-assembled network of DHI, and the complex interplay between the catechol group and the surface.

Chapter 5

• In this chapter the results on DHICA deposition on Au(111) are presented. The polymorphism behaviour of the molecule on surface is explained with the aid of the comparison to the two previous systems.

Chapter 6

• The general conclusions of the previous chapters are drawn, together with the possible future development of this work.

A French language resumé of this thesis is attached in Appendix B.

1.6 Chapter bibliography

1. U. G. K. Wegst, H. Bai, E. Saiz, A. P. Tomsia and R. O. Ritchie, Bioinspired structural materials, *Nat. Mater*, 2014, **14**, 23.
2. P. M. M. Pereira, G. A. Monteiro and D. M. F. Prazeres, in *Biotechnologies and Biomimetics for Civil Engineering*, eds. F. Pacheco Torgal, J. A. Labrincha, M. V. Diamanti, C. P. Yu and H. K. Lee, Springer International Publishing, 2015
3. S. Zhang, *Nat. Biotechnol*, 2003, **21**, 1171.
4. P. Benjwal, and K.Balani, in *Biosurfaces: A Materials Science and Engineering Perspective*, eds K. Balani, V. Verma, A. Agarwal and R. Narayan, John Wiley and Sons, 2014.
5. Photo credit to M. Stocker, Lego David https://blog.tepapa.govt.nz/2018/02/08/is-lego-art; accessed 18/04/19
6. Photo credit to academia.org, Michelangelo's David, http://www.accademia.org/explore-museum/artworks/michelangelos-david/; accessed 18/04/19
7. P. Ball, *Nanotechnology*, 2002, **13**, R15.
8. M. C. Roco, *Curr. Opin. Biotechnol*, 2003, **14**, 337.
9. C. Perez-Iratxeta, G. Palidwor and M. A. Andrade-Navarro, *EMBO reports*, 2007, **8**, 1135.
10. E. A. Ponomarenko, E. V. Poverennaya, E. V. Ilgisonis, M. A. Pyatnitskiy, A. T. Kopylov, V. G. Zgoda, A. V. Lisitsa and A. I. Archakov, *Int. J. Anal. Chem*, 2016, **2016**, 7436849.
11. C. M. Dobson, *Nature*, 2003, **426**, 884.
12. Picture credit to Khanacadaemy "α-helix" under "Chemistry of amino acids and protein structure" distriuted under CC-BY-NC-SA 4.0. https://www.khanacademy.org/test-prep/mcat/biomolecules/amino-acids-and-proteins1/a/chemistry-of-amino-acids-and-protein-structure accessed 18/04/19
13. Image credit to R. Wheeler, Haemoglibin image created with en:pymol from en:PDB enzyme 1GZX, distributed under a CC-BY 2.0 license.
14. G. Whitesides, J. Mathias and C. Seto, *Science*, 1991, **254**, 1312.
15. G. M. Whitesides and M. Boncheva, *Proc. Natl. Acad. Sci. U.S.A*., 2002, **99**, 4769.
16. G. M. Whitesides and B. Grzybowski, *Science*, 2002, **295**, 2418.
17. P. J. Butler, *Philos. Trans. R. Soc. Lond., B, Biol. Sci*, 1999, **354**, 537.
18. H. Fraenkel-Conrat and R. C. Williams, *Proc. Natl. Acad. Sci. U.S.A*, 1955, **41**, 690.
19. A. Klug, *Angew. Chem. Int. Ed. Engl*, 1983, **22**, 565-582.
20. T. M. Schuster, R. B. Scheele and L. H. Khairallah, *J. Mol. Biol*, 1979, **127**, 461.
21. J. Hwang, Y. Jeong, J. M. Park, K. H. Lee, J. W. Hong and J. Choi, *Int. J. Nanomedicine*, 2015, **10**, 5701.
22. H. J. Ensikat, P. Ditsche-Kuru, C. Neinhuis and W. Barthlott, *Beilstein J. Nanotechnol*, 2011, **2**, 152.
23. J. Lehr, F. de Marchi, L. Matus, J. MacLeod, F. Rosei and A.-M. Kietzig, *Appl. Surf.Sci*, 2014, **320**, 455.
24. G. de Mestral, 1951, Velvet type fabric and method of producing same US2717437,
25. M. Sarikaya, C. Tamerler, A. K. Y. Jen, K. Schulten and F. Baneyx, *Nat. Mater*, 2003, **2**, 577.
26. S. Zhang, *Biotechnol. Adv*, 2002, **20**, 321.
27. Photo credit to D. Breger, http://nymag.com/vindicated/2016/11/an-idea-that-stuck-how-george-de-mestral-invented-velcro.html; accessed 18/04/19
28. P. W. K. Rothemund, *Nature*, 2006, **440**, 297.

29. P. W. K. Rothemund, 2006, Methods of making nucleic acid nanostructures, US7842793B2
30. J. D. Watson and F. H. C. Crick, *Nature*, 1953, **171**, 737.
31. G. Verma and P. A. Hassan, *Phys. Chem. Chem. Phys*, 2013, **15**, 17016.
32. M. Rivas, L. J. del Valle, C. Alemán and J. Puiggalí, *Gels*, 2019, **5**, 14.
33. M. Bradshaw, D. Ho, M. W. Fear, F. Gelain, F. M. Wood and K. S. Iyer, *Sci. Rep*, 2014, **4**, 6903.
34. G. Zhang, S. P. Surwade, F. Zhou and H. Liu, *Chem. Soc. Rev*, 2013, **42**, 2488.
35. S. P. Surwade, F. Zhou, Z. Li, A. Powell, C. O'Donnell and H. Liu, *Chem. Commun*, 2016, **52**, 1677.
36. J.-M. Lehn, *Proc. Natl. Acad. Sci. U.S.A*, 2002, **99**, 4763.
37. J. W. Steed and J. L. Atwood, *Supramolecular chemistry*, John Wiley & Sons, 2013.
38. J. M. Lehn, *Acc. Chem. Res*, 1978, **11**, 49.
39. S. De Feyter and F. C. De Schryver, *Chem. Soc. Rev*, 2003, **32**, 393.
40. J. V. Barth, *Annu. Rev. Phys. Chem*, 2007, **58**, 375.
41. L. Gross, F. Mohn, N. Moll, P. Liljeroth and G. Meyer, *Science*, 2009, **325**, 1110.
42. A. Brillante, I. Bilotti, R. G. Della Valle, E. Venuti, A. Girlando, M. Masino, F. Liscio, S. Milita, C. Albonetti, P. D'Angelo, A. Shehu and F. Biscarini, *Phys. Rev. B*, 2012, **85**, 195308.
43. A. Kühnle, *Curr. Opin. Colloid Interface Sci*, 2009, **14**, 157.
44. M. Bieri, M.-T. Nguyen, O. Gröning, J. Cai, M. Treier, K. Aït-Mansour, P. Ruffieux, C. A. Pignedoli, D. Passerone, M. Kastler, K. Müllen and R. Fasel, *J. Am. Chem. Soc*, 2010, **132**, 16669.
45. J.-P. Bucher, L. Santesson and K. Kern, *Langmuir*, 1994, **10**, 979.
46. F. Vidal, E. Delvigne, S. Stepanow, N. Lin, J. V. Barth and K. Kern, J*. Am. Chem. Soc*, 2005, **127**, 10101.
47. W. Mamdouh, H. Uji-i, A. Gesquière, S. De Feyter, D. B. Amabilino, M. M. S. Abdel-Mottaleb, J. Veciana and F. C. De Schryver, *Langmuir*, 2004, **20**, 9628.
48. L. Cardenas, R. Gutzler, J. Lipton-Duffin, C. Fu, J. L. Brusso, L. E. Dinca, M. Vondráček, Y. Fagot-Revurat, D. Malterre, F. Rosei and D. F. Perepichka, *Chem. Sci.*, 2013, **4**, 3263.
49. D. M. Cyr, B. Venkataraman and G. W. Flynn, *Chem. Mater*, 1996, **8**, 1600.
50. G. Schull, L. Douillard, C. Fiorini-Debuisschert, F. Charra, F. Mathevet, D. Kreher and A.-J. Attias, *Nano Lett*, 2006, **6**, 1360.
51. C.-A. Palma, M. Cecchini and P. Samori, *Chem. Soc. Rev*, 2012, **41**, 3713.
52. O. Ivasenko and D. F. Perepichka, *Chem. Soc. Rev*, 2011, **40**, 191.
53. M. Lackinger and W. M. Heckl, *Langmuir*, 2009, **25**, 11307-11321.
54. M. Lackinger, S. Griessl, W. M. Heckl, M. Hietschold and G. W. Flynn, *Langmuir*, 2005, **21**, 4984.
55. Y. C. Ye, W. Sun, Y. F. Wang, X. Shao, X. G. Xu, F. Cheng, J. L. Li and K. Wu, *J. Phys. Chem. C*, 2007, **111**, 10138.
56. J. F. Dienstmaier, K. Mahata, H. Walch, W. M. Heckl, M. Schmittel and M. Lackinger, *Langmuir*, 2010, **26**, 10708.
57. T. J. Roussel, E. Barrena, C. Ocal and J. Faraudo, *Nanoscale*, 2014, **6**, 7991.
58. Y. Kuk and P. J. Silverman, *Rev. Sci. Instrum*, 1989, **60**, 165.
59. D. R. Yaniv and L. D. McCormick, *Nanotechnology*, 1992, **3**, 44.
60. M. P. Casaletto, G. M. Ingo, S. Kaciulis, G. Mattogno, L. Pandolfi and G. Scavia, *Appl. Surf. Sci*, 2001, **172**, 167.
61. S. J. Sowerby, M. Edelwirth and W. M. Heckl, *J. Phys. Chem. B*, 1998, **102**, 5914.
62. A. Ciesielski, M. El Garah, S. Masiero and P. Samorì, *Small*, 2016, **12**, 83.

63. W. M. Heckl, D. P. Smith, G. Binnig, H. Klagges, T. W. Hänsch and J. Maddocks, *Proc. Natl. Acad. Sci. U.S.A.*, 1991, **88**, 8003.
64. R. Otero, M. Schöck, L. M. Molina, E. Lægsgaard, I. Stensgaard, B. Hammer and F. Besenbacher, *Angew. Chem. Int. Ed. Engl*, 2005, **44**, 2270.
65. W. Xu, R. E. A. Kelly, H. Gersen, E. Lægsgaard, I. Stensgaard, L. N. Kantorovich and F. Besenbacher, *Small*, 2009, **5**, 1952.
66. R. E. A. Kelly, Y. J. Lee and L. N. Kantorovich, *J. Phys. Chem B*, 2005, **109**, 11933.
67. J. E. Freund, M. Edelwirth, P. Kröbel and W. M. Heckl, *Phys. Rev. B*, 1997, **55**, 5394.
68. R. E. A. Kelly, W. Xu, M. Lukas, R. Otero, M. Mura, Y.-J. Lee, E. Lægsgaard, I. Stensgaard, L. N. Kantorovich and F. Besenbacher, *Small*, 2008, **4**, 1494.
69. L. M. A. Perdigão, P. A. Staniec, N. R. Champness, R. E. A. Kelly, L. N. Kantorovich and P. H. Beton, *Phys. Rev. B*, 2006, **73**, 195423.
70. Q. Chen, D. J. Frankel and N. V. Richardson, *Langmuir*, 2002, **18**, 3219.
71. R. E. A. Kelly, M. Lukas, L. N. Kantorovich, R. Otero, W. Xu, M. Mura, E. Lægsgaard, I. Stensgaard and F. Besenbacher, *J. Chem. Phys*, 2008, **129**, 184707.
72. R. Otero, M. Lukas, R. E. A. Kelly, W. Xu, E. Lægsgaard, I. Stensgaard, L. N. Kantorovich and F. Besenbacher, *Science*, 2008, **319**, 312.
73. R. Otero, W. Xu, M. Lukas, R. E. A. Kelly, E. Lægsgaard, I. Stensgaard, J. Kjems, L. N. Kantorovich and F. Besenbacher, *Angew. Chem., Int. Ed. Engl*, 2008, **120**, 9819.
74. S. J. Sowerby and W. M. Heckl, *Orig. Life Evol. Biospheres*, 1998, **28**, 283.
75. M. S. Blois, in *Photochemical and Photobiological Reviews: Volume 3*, ed. K. C. Smith, Springer US, 1978.
76. M. d'Ischia, K. Wakamatsu, A. Napolitano, S. Briganti, J. C. Garcia-Borron, D. Kovacs, P. Meredith, A. Pezzella, M. Picardo, T. Sarna, J. D. Simon and S. Ito, *Pigment Cell Melanoma Res*, 2013, **26**, 616.
77. P. H. Proctor and J. E. McGinness, *Arch. Dermatol*, 1986, **122**, 507.
78. M. Irimia-Vladu, *Chem. Soc. Rev*, 2014, **43**, 588.
79. M. Muskovich and C. J. Bettinger, *Adv. Healthc. Mater*, 2012, **1**, 248.
80. C. J. Bettinger, J. P. Bruggeman, A. Misra, J. T. Borenstein and R. Langer, *Biomaterials*, 2009, **30**, 3050.
81. F. Solano, *New J. Sci*, 2014, **2014**, 28.
82. J. McGinness, P. Corry and P. Proctor, *Science*, 1974, **183**, 853.
83. J. Filatovs, J. McGinness and P. Corry, *Biopolymers*, 1976, **15**, 2309.
84. M. M. Abdel-Aziz, *Appl. Surf. Sci*, 2006, **253**, 2059.
85. C. H. Culp, D. E. Eckels and P. H. Sidles, *J. Appl. Phys*, 1975, **46**, 3658.
86. M. L. Wolbarsht, A. W. Walsh and G. George, *Appl. Opt.*, 1981, **20**, 2184.
87. J. Riesz, J. Gilmore and P. Meredith, *Biophys. J*, 2006, **90**, 4137.
88. S. E. Forest, W. C. Lam, D. P. Millar, J. B. Nofsinger and J. D. Simon, *J. Phys. Chem B*, 2000, **104**, 811.
89. M. L. Tran, B. J. Powell and P. Meredith, *Biophys. J*, 2006, **90**, 743.
90. S. P. Nighswander-Rempel, J. Riesz, J. Gilmore and P. Meredith, *J. Chem. Phys*, 2005, **123**, 194901.
91. M. D'Ischia, *Int. J. Mol. Sci*, 2018, **19**.
92. M. D. Hawley, S. V. Tatawawadi, S. Piekarski and R. N. Adams, *J. Am. Chem. Soc*, 1967, **89**, 447.
93. H. S. Mason, *J. Biol. Chem*, 1948, **172**, 83.
94. G. Prota, in *Melanins and Melanogenesis*, ed. G. Prota, Academic Press, 1992.
95. K. Wakamatsu and S. Ito, *Pigment Cell Res*, 2002, **15**, 174.

96. A. Pezzella, A. Napolitano, M. d'Ischia, G. Prota, R. Seraglia and P. Traldi, *Rapid Commun. Mass Spectrom*, 1997, **11**, 368.
97. A. Napolitano, A. Pezzella, G. Prota, R. Seraglia and P. Traldi, *Rapid Commun. Mass Spectrom*, 1996, **10**, 468.
98. M. d'Ischia, A. Napolitano, A. Pezzella, P. Meredith and T. Sarna, *Angew. Chem., Int. Ed. Engl*, 2009, **48**, 3914.
99. A. Pezzella, D. Vogna and G. Prota, *Tetrahedron*, 2002, **58**, 3681.
100. N. F. Mott, *Adv. Phys*, 1967, **16**, 49.
101. J. E. McGinness, *Science*, 1972, **177**, 896.
102. P. Meredith and T. Sarna, *Pigment Cell Res*, 2006, **19**, 572.
103. C.-T. Chen, F. J. Martin-Martinez, G. S. Jung and M. J. Buehler, *Chem. Sci*, 2017, **8**, 1631.
104. C.-T. Chen and M. J. Buehler, *Phys. Chem. Chem. Phys*, 2018, **20**, 28135.
105. C.-T. Chen, C. Chuang, J. Cao, V. Ball, D. Ruch and M. J. Buehler, *Nat. Commun*, 2014, **5**, 3859.
106. G. W. Zajac, J. M. Gallas, J. Cheng, M. Eisner, S. C. Moss and A. E. Alvarado-Swaisgood, *Biochim. Biophys. Acta Gen. Subj*, 1994, **1199**, 271.
107. J. M. Gallas, G. W. Zajac, T. Sarna and P. L. Stotter, *Pigment Cell Res*, 2000, **13**, 99.
108. K. C. Littrell, J. M. Gallas, G. W. Zajac and P. Thiyagarajan, *Photochem. Photobiol*, 2003, **77**, 115.
109. A. A. R. Watt, J. P. Bothma and P. Meredith, *Soft Matter*, 2009, **5**, 3754.

CHAPTER 2: EXPERIMENTAL TECHNIQUES

2.1 Scanning tunneling microscopy

As already highlighted in the introduction chapter, STM has become the technique of choice for the investigation of SAMN superficial morphology, mainly because of its high spatial resolution (from nanometric to atomic scale) and for the quantity of information obtained. In broad terms, STM shares the same functioning mechanism of other SPM techniques.[1] A micrometric mechanical system allows to manually approach the tip to the sample. After that, a piezoelectric system coupled with an inchworm motor leads the tip in the operative range of the instrument, and it allows it to raster scan (*i.e.* line by line) over the sample. The distance between the sample and the tip is constantly regulated by a feedback system, in order to follow the profile of the sample and to avoid it to crash into the surface.[1] The data related to the height or other kind of interactions is then collected by a computer that then converts it to an image of the density of states (DOS), from which the sample topography can be inferred.

STM allows to obtain such morphological profile on atomic scale of the surface without using any electronic source. Instead, its functioning is based on the tunneling current: the tip and the sample are maintained at different voltages, few Å from each other, forcing an electronic current to flow through the "tunneling barrier" between them. Typically, the tunneling currents are in the nanoampere range (0.1−5nA) and the voltage applied across the barrier ranges from 10mV to 10V. The distance from the nucleus of the apex atom of the tip to the nucleus of the sample atom is ordinarily kept between 5 and 15 Å. With this kind of instrument is possible to work in several settings: keeping constant the tunneling current ("current" or Constant Current Mode, CCM) or, *vice versa*, keeping constant the height of the tip with respect to the sample ("topographic" or constant height mode, CHM). In CCM, an electronic feedback system allows to keep the current constant as the tip moves on the x-y plane (the sample plane) and records the variation with respect to the z axis. On the other hand, in CHM mode, the feedback system keeps the height constant, thus collecting the variation of tunneling current respect to the x-y plane. Other than the morphologic information, it is possible also to do spectroscopy, obtaining thus the I/V spectra, related to the sample conductance and thus to its energetic gap.[2]

2.1.1 STM theory

A good starting point to understand the mechanics behind STM tunneling is given by the classical quantum physics problem of electron scattering from a potential barrier V of length L (Figure 2.1). Classical mechanics predicts that if the electron energy E is lower than the potential barrier V, it will not penetrate it but will be reflected or absorbed. Quantum mechanics instead shows that there's a small probability that the electron will tunnel to the other side, thus crossing the barrier.

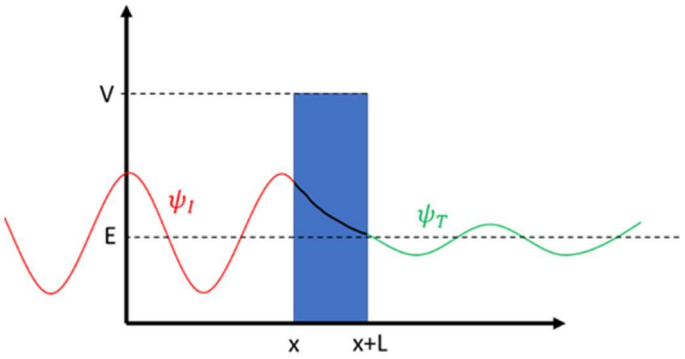

Figure 2.1: Model of a particle wave of energy E moving trough a finite potential barrier V.

It can be easily shown that the transmission coefficient T, calculated as the ratio between the probability densities $|\psi|^2$ of the particle transmitted ψ_T and incoming ψ_I, is equal to:

$$T = \left(1 + \frac{V^2}{4E(V-E)}\sinh^2\left(\frac{L}{\hbar}\sqrt{2m(V-E)}\right)\right)^{-1} \tag{2.1}$$

from which the tunneling current, in the limit of a strong attenuating barrier, can be estimated as:

$$I \sim A * e^{-L\sqrt{\frac{8m(E-V)}{\hbar}}} \tag{2.2}$$

This theoretical result can be applied as an approximation of the two metals separated by vacuum, such as in the STM case. The potential difference $E - V$ thus becomes the energy necessary to move an electron from its Fermi level at energy E_F to vacuum level, hence its work function ϕ. For a typical metal (ϕ = 2 – 5 eV) the current I decreases of one order of magnitude already after 1 Å. Hence, the current is very sensitive to small variation in the separation distance between tip and sample, thus giving very high vertical resolution. Following the same reasoning, in the case of an atomic sharp tip, 90% of the tunneling current will travel through the apex atom, giving a good lateral resolution as well.

While an easy example, this approach is limited to a single electron problem. A more rigorous theoretical approach is necessary in order to explain how the tunneling current strength is related to the spatial variation of physical properties of the sample. This is not a simple task, as it requires to join macroscopic and microscopic concepts in physics: while one may focus only on the interaction between the outermost tip atom and the surface atom probed, they are not two isolated systems, but part of macroscopic solids (hence around 10^{23} atoms) whose presence has to be taken in account. In other words, it is necessary to join the 'band' and the 'bond' picture.[3]

A first theoretical solution is given by the transfer Hamiltonian approach: initially employed by Bardeen in 1961 to explain Giaever's observation concerning tunneling in metal-insulator-metal superconductive junctions,[4] it was easily translated to the STM case.[5] In the simplified approach in one dimension, a potential barrier extends between x_a and x_b, separating the system in three regions, with the tip on the left and the sample on the right. Both of them are described by their an Hamiltonian with their own set of eigenfunctions ($H_S\psi_\mu^S = E_\mu\psi_\mu^S$ for the sample and $H_T\psi_\upsilon^T = E_\upsilon\psi_\upsilon^T$ for the tip), which quickly decay in the opposite regions. Within Bardeen model, also the potentials U_S and U_T are considered to be 0 outside their relative region. Within this view, the time evolution of a state ψ in the system tip-sample is governed by the Schrödinger equation:

$$-i\hbar\frac{\partial\Psi}{\partial t} = \left(-\frac{\hbar^2}{2m}\frac{\partial^2}{\partial x^2} + U_S + U_T\right)\Psi \tag{2.3}$$

Even in this simplified single-electron case (we're disregarding any interaction between electrons), it would be too hard to directly compute the eigenvalues and eigenfunctions of such Hamiltonian. Bardeen solved the problem by using instead the knowledge of the tip and sample' electronic structure. Following his approach, at the beginning the electron is stationary on the sample, thus $\psi(0) = \psi_\mu^S$, and is transferred to the tip as the time progresses. The wavefunction $\psi(t)$ can be expanded as a linear combination of the eigenfunctions for the two isolate components, as:

$$\Psi(t) = \psi_\mu^S e^{\frac{-iE_\mu t}{\hbar}} + \sum_\upsilon a_\upsilon(t)\psi_\upsilon^T e^{\frac{-iE_\upsilon t}{\hbar}} \tag{2.4}$$

By assuming that tip and sample states are orthogonal to each other, it is evident that the probability that an electron described by the state $\Psi(t)$ populates a state ψ_υ^T, expressed by the projection $|\langle\psi_\upsilon^T|\Psi(t)\rangle|^2$, is mainly due to $a_\upsilon(t)$. The time evolution coefficients can be calculated by time-dependent perturbation theory, and the scattering probability takes then a Fermi Golden Rule form:

$$P_{\mu\to\upsilon}=\frac{\partial|a_\upsilon(t)|^2}{\partial t}=\frac{2\pi}{\hbar}\left|\langle\psi_\upsilon^T|U_{Tip}|\psi_\mu^S\rangle\right|^2\delta(E_\mu-E_\upsilon)=\frac{2\pi}{\hbar}\left|M_{\mu\upsilon}\right|^2\delta(E_\mu-E_\upsilon) \quad (2.5)$$

The equation (5) takes in account only a single tunneling process, from μ to υ. On the other hand, tip and sample are characterized by a continuous of states. The total tunneling currents is the sum of each of those contributions, properly weighted by their occupation with the Fermi-Dirac distribution:

$$I=\frac{4\pi e}{\hbar}\sum_{\mu,\upsilon}f(E_\upsilon-E_F)(1-f(E_\upsilon-E_F)\left|M_{\mu\upsilon}\right|^2\delta(E_\mu-E_\upsilon-eV) \quad (2.6)$$

As it can be seen from equation 6, the current tunneling current is dependent of the DOS of the sample, modulated by the matrix element $M_{\mu\upsilon}$. The sign of the applied bias voltage V in the δ function is important, as it determines which states are imagined by STM: by switching the voltage, a completely different image can be detected, as shown below in Figure 2.2. In fact, from equation 6 it is evident that for negative potential the current is generated by the occupied states in the sample, whereas for positive bias the unoccupied states of the sample are of importance.

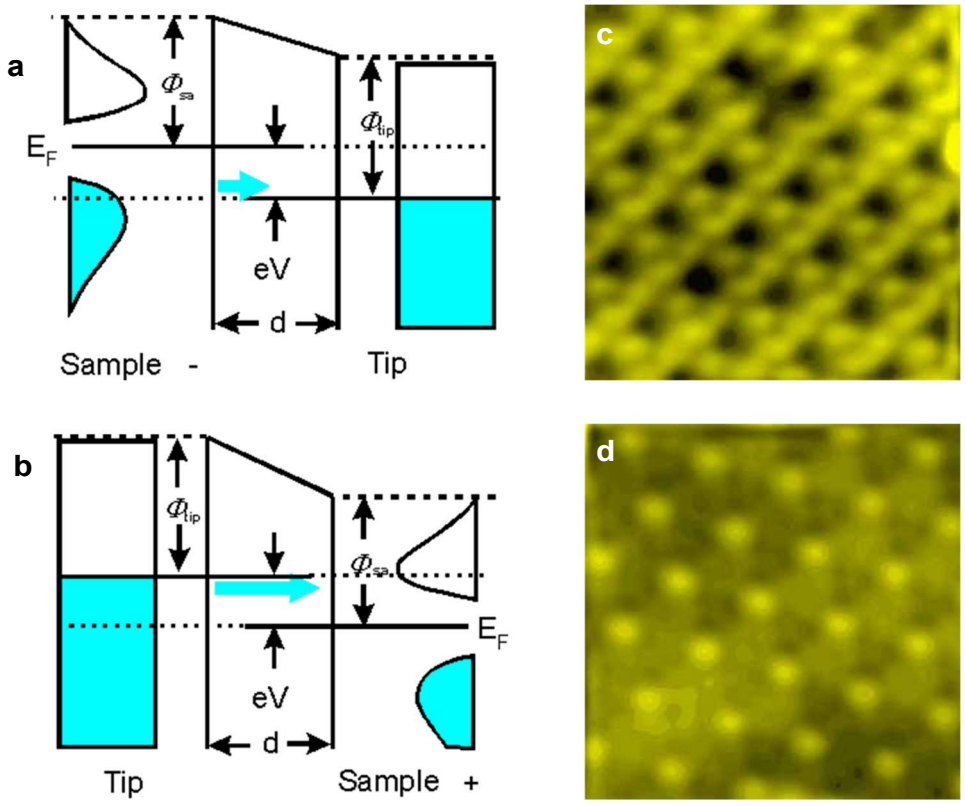

Figure 2.2: a) If the negative bias is applied on the sample, the current will be generated by the occupied states of the sample. Viceversa, if the bias is positive, b) the STM will probe the unoccupied states. On the right, c) occupied and unoccupied states of SiC(003) probed by STM.[6]

The last essential problem is to compute the matrix tunneling element $M_{\mu\upsilon}$. Bardeen's model is again useful, as the limitation on U_{Tip} and U_{Sam} allow to express the matrix as an integral over any surface lying entirely within the separation region between the tip and the sample, and depends only on the wavefunctions in the barrier:

$$M_{\mu\upsilon} = \langle \psi_\upsilon^T | U_T | \psi_\mu^S \rangle = \frac{\hbar^2}{2m} \int dS \left(\overline{\psi}_\upsilon^T \nabla \psi_\mu^S - \psi_\mu^S \nabla \overline{\psi}_\upsilon^T \right) \tag{2.7}$$

While this result concludes Bardeen's treatise, as it allows to calculate current between two metal contacts, for STM is not enough: as an explicit expression for the wavefunctions of the tip is not available since its actual atomic structure is not known.

As a solution to this problem, Tersoff and Hamann in 1983 proposed to model the tip as the simplest configuration possible, that is a spherical potential well centred in $\vec{r}_T$ (Figure 2.3a).[7, 8] The tip state ψ_υ^T can thus be expressed as a spherically symmetrical function and the tunneling matrix is therefore directly proportional to the value of the sample wavefunction in the geometrical point $\vec{r}_T$. Tersoff and Hamann model is commonly referred as S-wave tip wave function approximation, as it is possible to use the Bessel function of the s-orbital of the tip apex atom to calculate $M_{\mu\upsilon}$ and I, resulting:

$$I = \frac{16\pi^3 \hbar^3 C^2 e}{\kappa^2 m^2} n^T \int_0^{eV} n^S \left(\vec{r}_T, E_F^S + \epsilon \right) d\epsilon \tag{2.8}$$

where $\kappa = \frac{\sqrt{2m\phi}}{\hbar}$ is the decay constant, n^T and n^S are the DOS for tip and sample and C is a normalization constant.

a

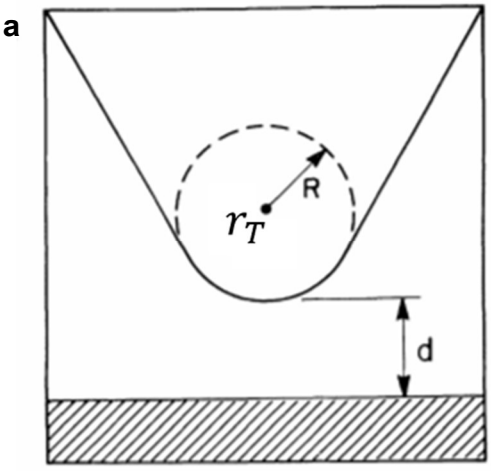

b

Tip Orbital	Matrix element
s	$\frac{2\pi C\hbar^2}{\kappa m}\psi^S(\vec{r}_T)$
p_x	$\frac{2\pi C\hbar^2}{\kappa m}\frac{\partial}{\partial x}\psi^S(\vec{r}_T)$
d_{zy}	$\frac{2\pi C\hbar^2}{\kappa m}\left(\frac{\partial^2}{\partial z \partial y}\psi^S(r_T) - \frac{1}{3}\kappa^2 \vec{r}_T\right)$

Figure 2.3: a) Tersoff approach to calculate the matrix element involves the assumption that the STM tip is spherical with radius of curvature R and centered in r_T (Figure adapted from Tersoff,[7] reproduced with permission of American Physical Society). b) Values of the matrix elements for the the different molecular orbitals.

From this result it is possible to obtain an expression for the spatial resolution achievable in STM, which however predict a lateral resolution of only 10 Å. In order to explain the atomic resolution obtained on most of the close packed metal surfaces, other molecular orbitals have to be taken in account. By utilizing spherical harmonics,[9] Chen was able to solve equation 7 for most of the atomic orbitals, and was able to explain the high atomic resolution of STM data by using a d_{z1}-state for the tip (figure 2.3b).

2.1 X-Ray photoelectron spectroscopy

While most of this thesis work revolves around STM analysis of 2D self-assembled networks, often the morphological information obtained is not sufficient to fully characterize a sample, and complementary techniques are necessary. In particular, compositional analysis of the surface is helpful to monitor the deposition on the surface or identify the presence of contaminants, while more sophisticated chemical analysis is required to discern between the different oxidation states that the chemical compounds, as in the case of our eumelanin precursors.

Within this view, photoemission spectroscopy (PES) is often the technique of choice. The common mechanism involves the fundamental photoelectric effect, the emission of an electron after the atomic absorption of a photon with energy $h\nu$ higher than the sample work function ϕ (Figure 2.4).

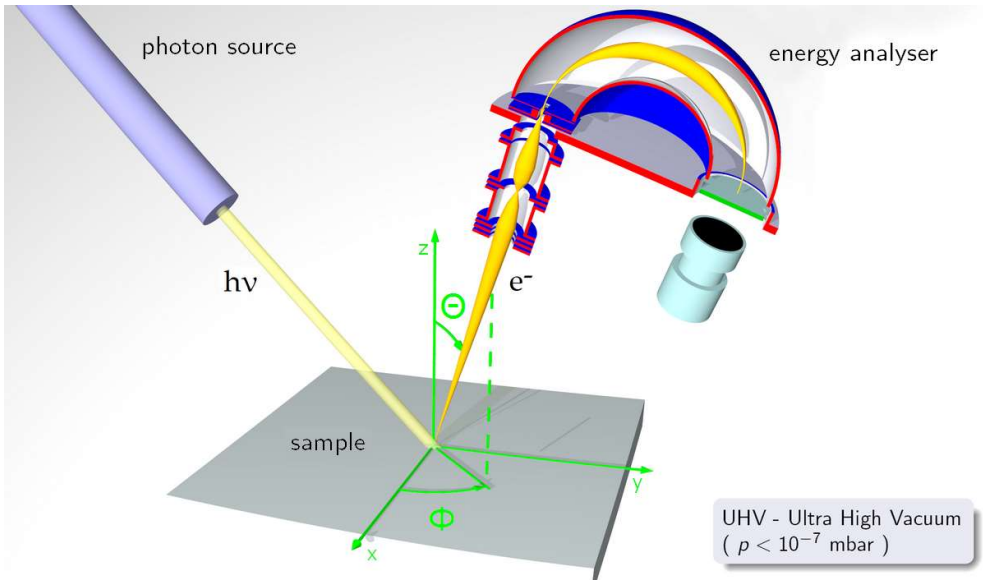

Figure 2.4: Model illustrating the general principle of work of PES.

In broad terms, PES experiments all share the same general procedure. Sample analysis takes place in a UHV environment, to enhance photoelectrons transmission as well as to minimizes contamination. Photons generated by a monochromatized light source generate irradiate a sample to generate charge carriers by photoelectric effect. While the penetration depth of the light varies in function of its wavelength, the mean free path for electrons is on the order of nanometres, hence the collected information is related to the surface and hence PESs are considered as surface analysis techniques. Those photoelectrons are collected, energy resolved, slightly retarded and counted with respect to emission angle and kinetic energy by an electrostatic analyser. In turn, the kinetic energy of the emitted electron E_k is related to its original electronic states, as well from its vibrational state and rotational level, which are specific for each chemical element, following the equation:

$$BE = h\upsilon - E_k - \phi_{spec} \tag{2.9}$$

where is the BE the binding energy and ϕ_{spec} a correction that has to be applied to take in account the Fermi level of the spectrometer.

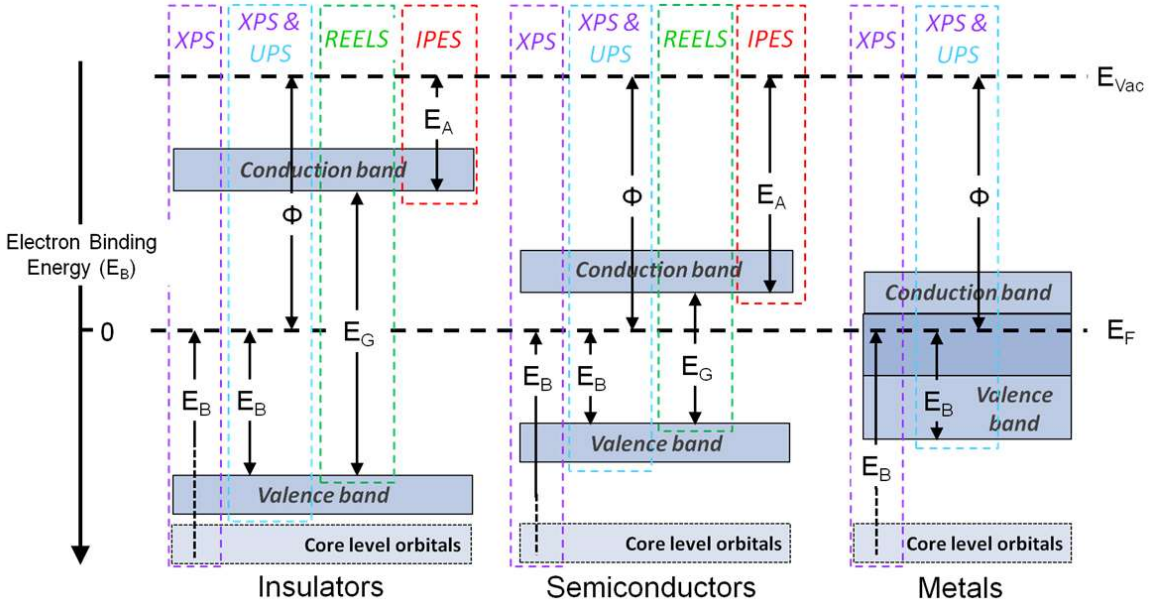

Figure 2.5: Relation between the different PES photon energy and the orbitals that can be investigated.

Starting from this common approach, different PES techniques were developed and named according to the wavelength used (Figure 2.5). Each the type of source in fact will determine from which molecular orbitals the photoelectrons are going to be emitted, and thus the properties that can be investigated. For example, Ultraviolet photoelectron

spectroscopy (UPS) relies on the photoelectrons emitted after the sample absorption of ultraviolet light, usually from a He discharge lamp. The low energy of the UV radiation (<41 eV) is sufficient to only eject electrons from the valence orbitals, thus UPS is more suitable to evaluate the material electronic work function. To investigate the elemental composition and depth profiling, X-Ray photoelectron spectroscopy (XPS) is instead more suitable, as the absorption of X-ray radiation (1000-1500 eV) allows to probe electrons from the core orbitals.

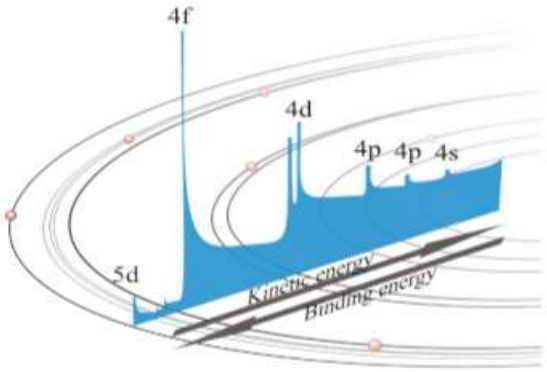

Figure 2.6 Photoelectron spectrum of lead showing the manner in which electron escaping for the solid can contribute to discrete peaks or suffer energy loss and contribute to background; the spectrum is superimposed on a schematic of a electronic structure of lead.[10]

The spectroscopic nomenclature for the XPS features is directly related to the various quantum numbers. The principal quantum number n appears first, followed by the angular momentum $l = 0,1,2,3$ labelled as s, p, d, f and finally total momentum $j = l + s$ (Figure 2.6).

The first acquisitions of photoelectric spectra date back to the early 1900, and while it was already evident that the positions of the absorption features were characteristic of the different elements, it took some time to fully understand why the same chemical species sometimes present small shifts – possible surface charge was one hypothetical explanation.

The development of XPS as an analytical tool required a great improvement of both the instrument's spatial and energy resolution and is largely attributable to the work with X-rays of the Manne Siegbahn group at the university of Lund and Uppsala, and in particular to his son Kai Siegbahn, who was awarded half of the Nobel Prize in 1981 for it.[11] In particular, the turning point came in 1963, after some complementary measurements on a photographic fixer (sodium thiosulfate) that revealed a double peak feature in the sulfur region.[12] The result could not be due to any surface charge or other instrumental effect,

since the sodium line was instead unsplit. It was thus realized that these shifts were correlated to the different chemical environment, marking the first conception of the electron spectroscopy for chemical analysis (ESCA), or as it is more commonly referred today, XPS.

2.2.2 PES theory

A few theoretical insights on the underlying principles of PES are useful to correctly understand the relation between the XPS spectra features and the material properties. A perfect starting point is given by the three-step model introduced by Berlung and Spicer in 1964.[13] As the name suggests, to better clarify all the contributions that affect the photoemission spectra intensity, the process is divided into three simpler steps: optical excitation, transport of the electron to the surface, and escape of the electron through the surface into the vacuum (figure 2.7).

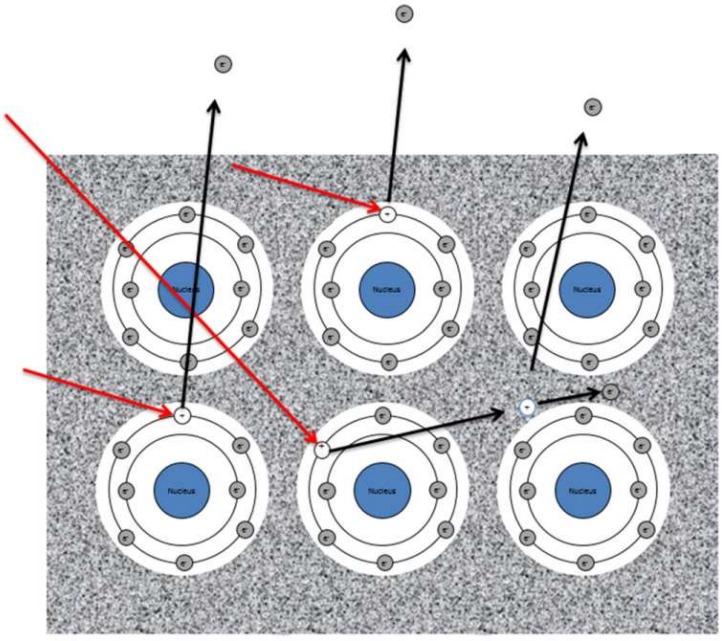

Figure 2.7: A schematic describing the three-step model. The red line represents a photon with energy in the x-ray regime, the black line represents the excited electron classically and the gray cloud represents the electrons participating in the bonding. (reproduced from Santana[14])

To properly explain the physical meaning of the BE, we can take a deeper look in the first step of the process, where after the absorption of a photon with energy $h\upsilon$ a single electron is excited from his initial state ψ_i is to a final state ψ_f. The most general form of a Hamiltonian perturbed by an electromagnetic radiation is given by:

$$H = \frac{1}{2m}\left(-\mathrm{i}\hbar\nabla - \frac{e}{c}A\right)^2 + eE + V \tag{2.10}$$

where A is electromagnetic vector potential of the incident light and E is the scalar potential. Similar to the approach followed in section 2.2, the intensity of the photoemission current is linked the probability of transition, that is described by Fermi's golden rule. By considering the gauge E=0, as well as neglecting two-photon processes and surface effects, the probability can be expressed as:

$$P_{i\to f} \propto \frac{2\pi}{\hbar}\left|\langle\psi_f|A\cdot\nabla|\psi_i\rangle\right|^2 \delta\left(E_f - E_i - h\upsilon\right) \tag{2.11}$$

While a discussion of the transition matrix element is out of the scope of this work, it is useful to further examine the two wavefunctions in order to simplify the problem by moving toward a one-electron view. Assuming that the system has N electrons, the initial state ψ_i can be written as a product of two wavefunctions: one for the orbital ϕ_k, from which the electron has been photoemitted, and another for remaining N-1 electrons $\psi_i(N-1)$. Following the same reasoning, final state ψ_f can written as the product of $\psi_f(N-1)$ and the free electron wavefunction ϕ_f. The matrix element in eq. 11 is thus reduced to:

$$\langle\psi_f|A\cdot\nabla|\psi_i\rangle = \langle\phi_f|A\cdot\nabla|\phi_k\rangle\langle\psi_f(N-1)|\psi_i(N-1)\rangle \tag{2.12}$$

Within the frozen-orbital approximation (Koopman's theorem), the *passive orbitals* $\psi_i(N-1)$ are not affected by the loss of the electron in ϕ_k, and thus the overlap integral in eq. 12 is reduced to unity. Under this assumption, the measured BE in eq. 9 is $-\varepsilon_k$, the negative Hartree-Fock energy of the orbital k, that is characteristic for each element.

On the other hand, the experimental value for BE is often far from the predicted quantum mechanical one. Aside from the evident application limits of Koopman's theorem, which are accounted by adding proper relaxation energies, it was already evident during the development of XPS that the core peaks position for the same element could present some variation of BE. This is due to the presence of non-equivalent atoms: different oxidation states, molecular environment, lattice sites and so on.

The physical basis of this variation, commonly called chemical shift, is illustrated by the charge potential model. The atoms are considered to be hollow spheres, on whose surface lies a valence charge Q_i The binding energy for a particular core level on atom i is thus given by:

$$\mathrm{BE}_i = \mathrm{BE}_i^0 + KQ_i + V \tag{13}$$

where BE_i^0 is the BE for the neutral atom, K a constant, and V is the potential energy produced by charges on the other atoms. The formation of an atomic bond causes a

displacement of charge, and the BE shift between difference chemical species can be thus seen as:

$$\Delta \mathrm{BE}_i = \Delta \mathrm{BE}_i^A - \Delta \mathrm{BE}_i^B \quad = \mathrm{K}\Delta Q_i + \Delta V + \Delta E_R \tag{14}$$

where the last term E_R represents the response of the in surrounding atoms to the formation of the core hole.

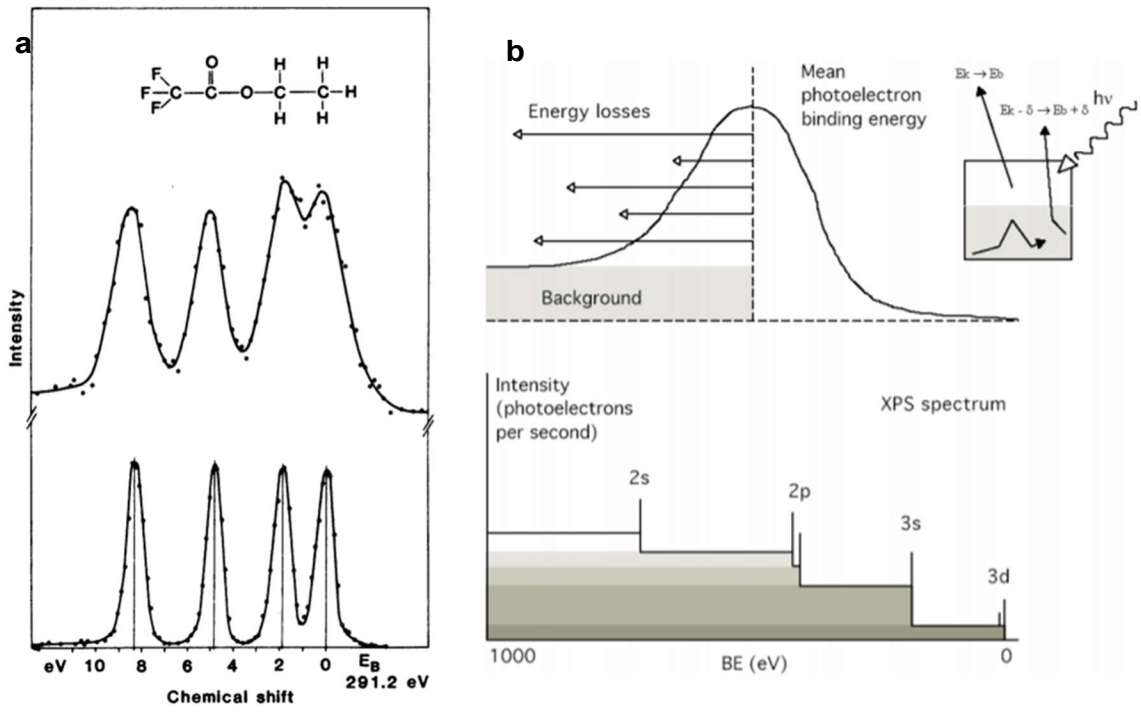

Figure 2.8: a) The shifts of the C1s components in the XPS spectra of ethyl trifluoroacetate. Upper spectrum taken without and lower spectrum taken with x-ray monochromatization (Figure reproduced from Siegbahn,[11] reproduced with permission of the American Association for the Advancement of Science). b) The background feature after the peak is due to scattered electrons, and c) it increases at higher BE.

Similar to other spectral line, also XPS peaks have non-zero linewidth, but have a slightly asymmetric peak shape that cannot be explained by just the natural broadening. This can be explained by examining the second part of the three-step model, where the excited electron moves towards the material surface. If an inelastic scattering occurs during the migration, the electron will lose energy, and will contribute to form a tail of background signal with a characteristic step shape (Figure 2.8).

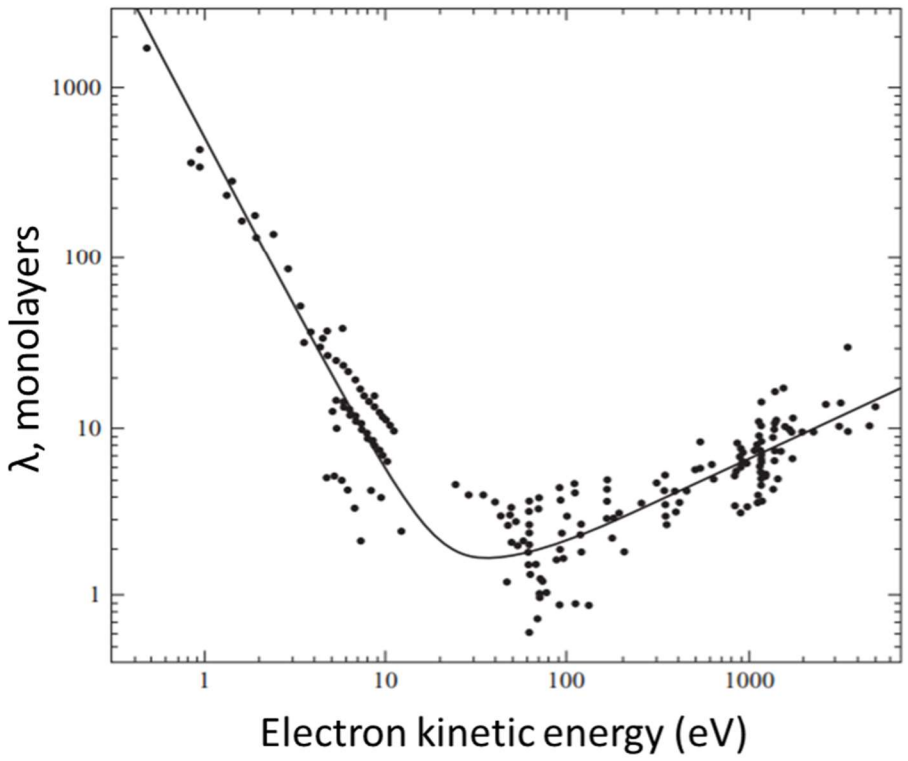

Figure 2.9: Compilation of results for the IMFP for elements as a function of electron energy (reproduced from Seah,[15] with permission of John Wiley and Sons)

The ability of an electron to propagate without losing energy (hence information from which initial state it was in) is measured by the inelastic mean free path (IMFP), which depends on both the energy E and the direction of propagation $\vec{k}$. It is not uncommon to find the IMFP index reported only as a function of the energy, as in Figure 2.9. On the other hand, it is important to take in account the nature of the material: the presence of plasmons in metals, as an example, gives a IMFP twice as small as the one of a wide band gap organic insulator.[16]

Lastly, for all the orbitals except the s, a characteristic doublet feature peak is present, due to the spin-orbital splitting. In fact, for $l > 0$ two possible states are possible, each characterized by the quantum number $j = l + s$. The doublet has different binding energies, with the anti-parallel alignment appearing at higher binding energy. The two peaks also have specific area ratios based on the degeneracy of each spin state, *i.e.* the number of different spin combinations that can give rise to the total j. These ratios are very helpful, as they can be used as constrain when fitting the spectra for p, d and f core levels.

2.3 Experimental equipment

All of the experiments presented in this PhD thesis were performed in the NanoFemtoLab (NFL) facilities at the INRS-EMT of Varennes. The NFL instrumentation consists in two multichamber UHV systems, which allows for the preparation and *in situ* characterization of the samples.

In the SPECS one, shown in Figure 2.10a, a turbomolecular pumping system connected to a fast entry air lock allows to insert samples without breaking the vacuum of the main system. In order to do so, the samples, mainly metal single crystals, are caged inside a sample holder that can be transferred through the whole UHV system. The fast entry is connected to two separate chambers, each one equipped with their own pumping system combining an ion pump and titanium sublimation pump. The two chambers are interconnected with normally closed gate valves and the base pressure is in the low 10^{-10} mbar range. One of them hosts the STM apparatus, an Aarhus 150 VT instrument (SPECS Surface Nano Analysis), along with a parking stage that offers the possibility of storing five samples/substrates and one tip sputtering-plate simultaneously. The lowest parking stage level accommodates the sample with its face perpendicular to a sputtering gun and is connected to a heating system that allows the sample thermal annealing. The deposition of the molecules takes place in the second chamber, (Figure 2.10b) in order to avoid contamination of the STM equipment. In this MBE chamber, the substrate is placed in a main stage, whose position can be lowered to be approach several resistively heated crucibles. A quartz crystal microbalance (QCM) instrument can be positioned between the sample and the evaporators, allowing to measure the deposition rate and ensuring repeatable preparation of molecular layers. The precursors are dosed on the substrates kept at room-temperature from an alumina (Al_2O_3) crucible in a Knudsen-type effusion. The temperature of deposition was chosen in function of the molecular precursor and substrate sticking coefficient, as reported in Table 2.1.

Table 2.1: The evaporation temperature for the different molecules

Molecular precursor	T evaporation
I2CA on Au(111)	70°C
DHI on Au(111)	70°C
DHI on Ag(111)	60°C
DHICA on Au(111)	85°C

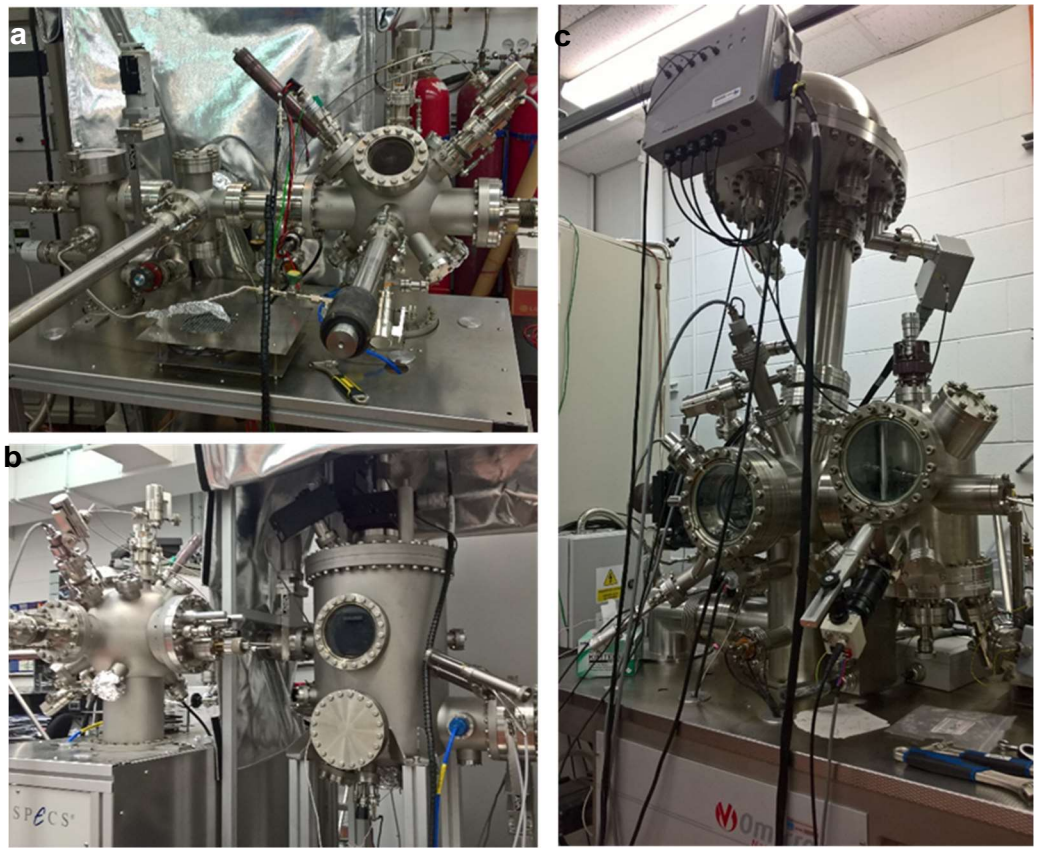

Figure 2.10: the two UHV system used in this thesis work

The second UHV chamber (Figure 2.10c) is a STM/XPS system commercially available from Scienta Omicron Gmbh. The low vacuum is maintained by a pump system combining an ion pump and titanium sublimation pump, supported by two turbomolecular pump during high pressure operations (*i.e.* Argon sputtering, molecular dosing or O_2 oxidation). A small chamber is present on the back, which is used also as a separate preparation chamber for precursors with low evaporation temperature. From this fast-entry chamber, the sample can be transferred to a mechanical arm in the main chamber, which can rotate and move along the three axes in order to reach all the characterization equipment. The chamber includes an STM system (VT-STM), a LEED apparatus (SpectaLEED), an Al and Mg XPS source along with its analyser (SPHERA II U5) and a sputtering gun.

2.3.1 Experimental procedures

The standard course of an experiment in the SPECS system involves the preparation and cleaning of the metallic substrates. The sample is transferred in the SPECS chamber, that is equipped with a sputter gun and annealing system. The Ar gas is injected in the chamber

through a leak valve until a partial pressure of $1x10^{-6}$ mbar is obtained, and then the sample's metal surface is bombarded with Ar^+ ions for 10-15' at 1-2 keV, removing any adsorbates and impurities. After sputtering, the surface will be very rough, and is smoothen by thermal annealing at 450-550 C for 30'. The process is repeated several times until an atomically flat surface is obtained. The sample is characterized by STM, in order to confirm the quality of the surface and to record high resolution images of the surface to be used as calibration in the successive steps. To trigger oxidation, the same procedure was adopted in both UHV chambers: samples were exposed to O_2 gas by dosing through a leak valve in the main chamber, at a pressure of 10^{-6} mbar for 30 minutes. Similar preparation procedures were adopted for the XPS characterization of the sample, that was carried out in the Omicron system.

2.4 Chapter Bibliography

1. G. Binnig, H. Rohrer, C. Gerber and E. Weibel, *Phys. Rev. Lett*, 1982, **49**, 57
2. R. M. Feenstra, *Surf. Sci*, 1994, **299-300**, 965.
3. R. Wiesendanger and H. J. Güntherodt, in *Scanning Tunneling Microscopy III: Theory of STM and Related Scanning Probe Methods*, Springer Berlin, 1993.
4. J. Bardeen, *Physical Review Letters*, 1961, **6**, 57.
5. A. D. Gottlieb and L. Wesoloski, *Nanotechnology*, 2006, **17**, R57.
6. Picture credit to U. Starke; http://nymag.com/vindicated/2016/11/an-idea-that-stuck-how-george-de-mestral-invented-velcro.html; accessed 18/04/19.
7. J. Tersoff and D. R. Hamann, *Phys. Rev. Lett*, 1983, **50**, 1998.
8. J. Tersoff and D. R. Hamann, *Phys. Rev. B*, 1985, **31**, 805.
9. C. J. Chen, in *Scanning Tunneling Microscopy III: Theory of STM and Related Scanning Probe Methods*, eds. R. Wiesendanger and H.-J. Güntherodt, Springer Berlin, 1996.
10. Picture credit to M. Franinović, X-ray photelectron spectroscopy, Figure 2; http://mafija.fmf.uni-lj.si/seminar/files/2013_2014/XPS024.pdf accessed 18/04/19.
11. K. Siegbahn, *Science*, 1982, **217**, 111.
12. I. Lindgren, *J. Electron Spectros. Relat. Phenomena*, 2004, **137-140**, 59.
13. C. N. Berglund and W. E. Spicer, *Phys. Rev*, 1964, **136**, A1030.
14. J. A. Colón Santana, in *Quantitative Core Level Photoelectron Spectroscopy*, Morgan & Claypool Publishers, 2015.
15. M. P. Seah and W. A. Dench, *Surf. Interface Anal*, 1979, **1**, 2.
16. P. J. Cumpson, *Surf. Interface Anal*, 1997, **25**, 447.

CHAPT 3: I2CA, A MODEL SYSTEM FOR INDOLE SELF-ASSEMBLY

In this chapter, we present our study of the self-assembly of indole-2-carboxylic acid (I2CA). Although the molecule is not related to the biochemical process of eumelanin, the investigation of I2CA was a necessary step before tackling more complex catechol precursors. The system was simple enough to provide a good model for the investigation of intermolecular reactions between indole the backbones. In fact, while the supramolecular chemistry of carboxylic acids was well-known and extensively reported, the on-surface stability of indole moieties and their prochiral behaviour had not been investigated before the publication of this work.

I have fulfilled most of the experimental work presented in this paper, except for the liquid/solid interface STM measurements which were performed by Dr. Macleod and Dr. Cui. Dr. Lipton-Duffin supported me with the STM system training, as well as performing the DFT to calculate the energy of the different I2CA prochiral networks together with Dr. Macleod. This work was initially part of a joint project between the research group of prof. Santato (École Polytechnique de Montréal) and prof. Rosei, and as such the two professors participated in the discussions on the data interpretation and manuscript preparation.

Self-assembly of indole-2-carboxylic acid at graphite and gold surfaces

Published in Journal of Chemical Physics 142, 101923 (2015); doi: 10.1063/1.4908143

(Received 6 December 2014; accepted 2 February 2015; published online 24 February 2015)

Fabrizio De Marchi,[1] Daling Cui,[1] Josh Lipton-Duffin,[1] Clara Santato,[2] Jennifer M. MacLeod,[1] and Federico Rosei[1,3]

[1]Centre Énergie, Matériaux et Télécommunications, Institut National de la Recherche Scientifique, 1650 Boulevard Lionel-Boulet, Varennes, Quebec J3X 1S2, Canada

[2]Département de Génie physique, École Polytechnique de Montréal, C.P. 6079, Succ. Centre Ville, Montréal, Quebec H3C 3A7, Canada

[3]Center for Self-Assembled Chemical Structures, McGill University, 801 Sherbrooke Street West, Montreal, Quebec H3A 0B8, Canada

Abstract

Model systems are critical to our understanding of self-assembly processes. As such, we have studied the surface self-assembly of a small and simple molecule, indole-2-carboxylic acid (I2CA). We combine density functional theory gas-phase (DFT) calculations with scanning tunneling microscopy to reveal details of I2CA assembly in two different solvents at the solution/solid interface, and on Au(111) in ultrahigh vacuum (UHV). In UHV and at the trichlorobenzene/highly oriented pyrolytic graphite (HOPG) interface, I2CA forms epitaxial lamellar structures based on cyclic OH···O carboxylic dimers. The structure formed at the heptanoic acid/HOPG interface is different and can be interpreted in a model where heptanoic acid molecules co-adsorb on the substrate with the I2CA, forming a bicomponent commensurate unit cell. DFT calculations of dimer energetics elucidate the basic building blocks of these structures, whereas calculations of periodic two-dimensional assemblies reveal the epitaxial effects introduced by the different substrates.

3.1 Introduction

Supramolecular self-assembly at surfaces is a promising route towards the synthesis of nanoscale materials.[1–4] As in processes that occur in the natural world, molecules deposited on a surface can spontaneously rearrange, bonding to each other non-covalently and creating ordered networks (self-assembled molecular networks, SAMNs) that can be exploited for a variety of applications.[5] The functionalization of the molecular building blocks allows for the introduction of specific interactions in the self-assembled structure; a given functional group can promote certain bonding geometries, or hinder others due to steric constraints.[6] For example, carboxyl groups can stabilize self-assembled networks through a wide range of available hydrogen bonding motifs.[7,8] The surface self-assembly of molecules with two to four carboxyl groups has been extensively studied.[6,9–25] When appropriately disposed, the –COOH groups facilitate the formation of ordered hydrogen-bonded arrays on relatively non-reactive surfaces including highly

oriented pyrolytic graphite (HOPG) and Au(111). These surfaces are typically selected to allow intermolecular interactions, rather than molecule-substrate interactions, and play the most significant role in the formation of the molecular film. Less work has been done on systems with lower degrees of functionalization, since, a priori, their ability to stabilize ordered twodimensional architectures is reduced. A limited literature exists on the surface self-assembly of molecules functionalized with a single –COOH group and suggests that more investigation will prove useful. For example, the simplest benzenebased acid, benzoic acid, has not been found to produce any two-dimensional long range ordered structures.[26] Thiophene2-carboxylic acid similarly failed to produce observable structures.[27] On the other hand, pyridinecarboxylic acids can form ordered layers stabilized by O–H···N and C–H···O interactions at the liquid/HOPG interface,[28] and ferrocenecarboxylic acid has recently been shown to form hydrogen-bonded pentamers[29] and double-row cluster geometries on Au(111).[30] Here, we report on the self-assembly of indole-2-carboxylic acid (I2CA), a small bicyclic planar molecule comprising benzene and pyrrole (Figure 3.1(a)), which has been previously investigated as a possible treatment for spasticity, acting as an antagonist for strychnine-insensitive glycine receptors.[31,32] The molecule is made interesting by its single carboxylic functionalization, which allows only a few possibilities for intermolecular hydrogen bonding (O–H···O, N–H···O, C–H···O), and by the low symmetry of the molecule, which in turn expands the number of possible molecular geometries within the bonding motifs. Indole derivatives are also interesting because of their biological and medical relevance.33 Dihydroxyindoles and their various redox forms constitute the building blocks of eumelanin, a ubiquitous pigment in plant and animals, and as such they are suited to the study of self-assembly in eumelanin.[34] Polyindoles, commonly synthesized electrochemically, are well-investigated organic electronic polymers.[35,36]

We investigated the self-assembly of I2CA under a range of conditions, using scanning tunneling microscopy (STM) and density functional theory (DFT) to study the structures formed. Two substrates were used: Au(111) and HOPG. Vacuum deposition was used to form molecular layers on Au(111), whereas molecular assembly on HOPG was investigated at the solution/solid interface using two different solvents. Gas-phase DFT calculations corroborated our experimental observations and provided insight into the role of epitaxy in the supramolecular assembly and the limitations of using STM for studying these systems.

3.2 Experimental and theoretical methods

3.2.1 Solution/solid STM

Saturated solutions of I2CA (>98%, Tokyo Chemical Industry Co., Ltd.) were prepared in heptanoic acid (99%, Sigma Aldrich) and 1,2,4-trichlorobenzene (TCB, >99%, Sigma Aldrich). Experiments were performed in ambient using a Digital Instruments (DI) STM controlled with a DI Nanoscope IIIa controller. Prior to each experiment, fresh HOPG (Structure Probe grade SPI-2) surfaces were exposed by cleaving with adhesive tape. STM tips were cut from 80/20 PtIr wire (NanoScience Instruments). Molecular solutions were applied drop-wise to the HOPG substrate.

3.2.2 Vacuum STM

Vacuum STM experiments were performed using an Aarhus 150 instrument (Specs Surface Nano Analysis GmbH) at room temperature. The STM is housed in an UHV chamber with a base pressure of 10^{-10} mbar. Prior to each experiment, the (111)-oriented Au crystal (Princeton Scientific) was cleaned by repeated cycles of sputtering under 1.5 kV Ar^+ ions and subsequent annealing to 350°C. The surface was then characterized by STM to verify the presence of the Au(111)- ($22 \times \sqrt{3}$) herringbone reconstruction.[37] I2CA molecules were deposited on room-temperature Au(111) from an alumina (Al_2O_3) crucible in a Knudsen-type effusion cell at a temperature of 70°C and pressure of 10−7 mbar.

3.2.3 Image processing and analysis

All image processing and analysis were done using the free WSxM software.[38] Image calibrations were based on the known lattice constants of the HOPG (0.246 nm) and Au(111) (0.288 nm) substrates. Molecular unit cells were obtained starting from images in which both the molecular layer and the underlying surfaces were imaged in the same frame. On HOPG, we identified the exact epitaxy matrix for the molecular overlayer structures using image autocorrelation. On Au(111), we performed a real-space lattice correction described in the supplementary material[39] (section 3.6.1).

3.2.4 DFT calculations

Gas-phase molecular bonding geometries and energetics were identified with DFT calculations of molecular dimers and trimers using the Gaussian09 software[40] at the B3LYP/6- 31G(d,p) level. For all calculations, the highest possible symmetry constraints were imposed and the molecules were kept planar. DFT calculations of the extended structures of the molecular layers were made using periodic boundary condition (PBC) calculations under the open-source code QUANTUM ESPRESSO,[41] version 5.0.3, using ultrasoft pseudopotentials with a 680 eV cutoff for the plane-wave basis. The generalized gradient approximation in the Perdew-BurkeErnzerhof parameterization (GGA-PBE) was used for the exchange-correlation functional.[42] The exchange-correlation was augmented by adding an ab initio nonlocal van der Waals correlation contribution (vdW-DF).[43–45] Comparison between the standard GGA-PBE methods and the vdW-DF correction is provided. No substrate was considered during the optimization, so the calculated geometries can be considered gas-phase only. As such, all parameters including atomic positions and cell dimensions were free to vary during the calculations. Optimization was performed until the total force on the ions was below 0.001 Ry/Bohr, and the total pressure on the unit cell was below 0.5 kbar. Starting geometries and results were prepared and visualized with the VESTA[46] and XcrySDen[47] software packages.

3.3 Results

3.3.1 Calculated hydrogen-bonding geometries

The single functional group of I2CA limits the number of possible structures accessible through hydrogen bonding, yet the low symmetry of the molecule means that a number of geometries exist for a given bonding arrangement. Gas-phase DFT elucidated the energetics and geometries of a number of possible structures. The geometries are shown in Figure 3.1, and the bond energies are summarized in Table 3.1. I2CA is shown as structures (a) and (b), with the two molecules distinguished by the rotation of the –COOH group. Cyclic dimerization of the –COOH groups of two molecules produces a linear dimer with either trans- (Figures 3.1(c) and 3.1(e)) or cis- (structure (d)) symmetries determined by the relative orientation of the two pyrrole rings. Structures (c) and (e) are distinguished by the relative orientation of the –COOH groups with respect to the nitrogen in the pyrrole.

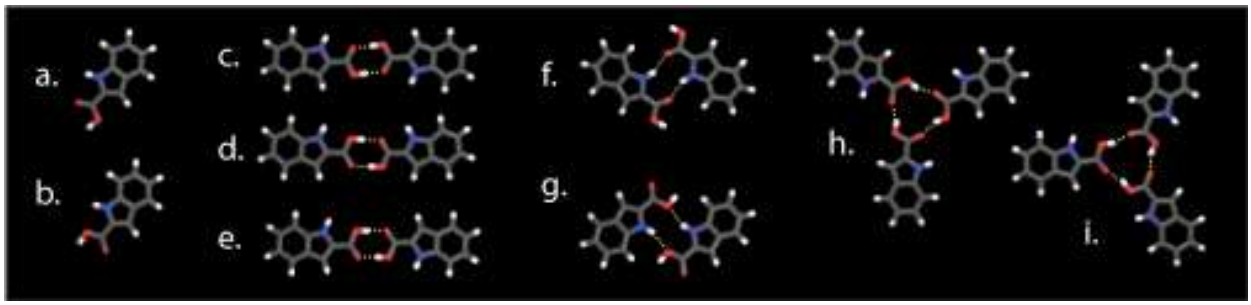

Figure 3.1: I2CA and some of its possible hydrogen bonding associations. These geometries have been optimized at the B3LYP/6-31G(d,p) level. Hydrogen bonds are indicated as dashed yellow lines. ((a) and (b)) I2CA, (c) –COOH dimer (trans-symmetry), (d) –COOH dimer (cis-symmetry), (e) –COOH dimer (trans-symmetry), ((f) and (g)) NH· · ·O dimer, ((h) and (i)) –COOH trimers (high-symmetry).

Cyclic NH···O bonding (Figures 3.1(f) and 1(g)) produces high-symmetry dimers that we refer to as "offset dimers", and which can again be distinguished by the rotation of the –COOH groups. Cyclic trimerization of the –COOH groups of three molecules is shown in structures (h) and (i). These high-symmetry trimers are distinguished from one another by the rotation of the –COOH groups. Calculations of lower-symmetry trimers, where two pyrrole nitrogens faced one another, revealed that the structure was unstable with respect to the formation of a low-symmetry –COOH dimer (Figure 3.1(d)) with the third I2CA molecule forming a weak O–H···O bond to the dimer. Similar to other calculations of –COOH bond energetics, we find that the cyclic dimer bond (Figures 3.1(c)–3.1(e)) is the most stable at approximately −10 kcal/mol per –COOH.16,25

Table 3.1: DFT-calculated bond energies for I2CA associations shown in Figure 3.1. The *Monomer units* column indicates which of the two isomers is present in the multimer structure. The bond energy per molecule, as well as the total energy (normalized to the energy of isolated I2CA in its lowest energy conformation), is also given.

Structure	Figure 3.1	Monomer units	Bond energy (kcal/mol per molecule)	Relative total energy (kcal/mol per molecule)
Monomer	**a**		-	0
Monomer	**b**		-	1.17
trans –COOH dimer (C2h)	**c**	a/a	-10.17	-10.17
cis –COOH dimer	**d**	a/b	-10.45	-9.87
trans –COOH dimer (C2h)	**e**	b/b	-10.8	-9.64
Offset NH…O dimer	**f**	a/a	-6.6	-6.6
Offset NH…O dimer	**g**	b/b	-4.17	-0.92
High symmetry (C3h) –COOH trimer	**h**	a/a/a	-8.75	-8.75
High symmetry (C3h) –COOH trimer	**i**	b/b/b	-9.4	-8.23

3.3.2 Au(111) in UHV

After deposition onto room temperature Au(111), I2CA molecules spontaneously arrange into a well-defined molecular layer (Figure 3.2(a)). The internal contrast of high-resolution STM images suggests that the molecules form –COOH dimers that align into lamellae. The I2CA dimers are oriented with their long axes tilted with respect to the lamellar short axis, with neighboring lamellae mirror-reflecting the tilt angle. The dimers thus form a chevron-like structure with a unit cell indicated in Figure 3.2(b). Images where the substrate and the molecular overlayer could be imaged simultaneously (see supplementary material[39] , figure 3.8-10) allow us to identify the unit cell of the molecular overlayer structure as u=0.77 nm and v=3.17 nm, with an angle γ=91.1° between them. Since the presence of the Au(111)-(22×√3) herringbone reconstruction implies a uniaxial compression of the surface atoms along ⟨1-10⟩[37,48] an anisotropic surface unit cell must be used to calculate the molecular overlayer lattice.[49] The above values are based on this anisotropic surface lattice (see supplementary material[39] section 3.6.1).

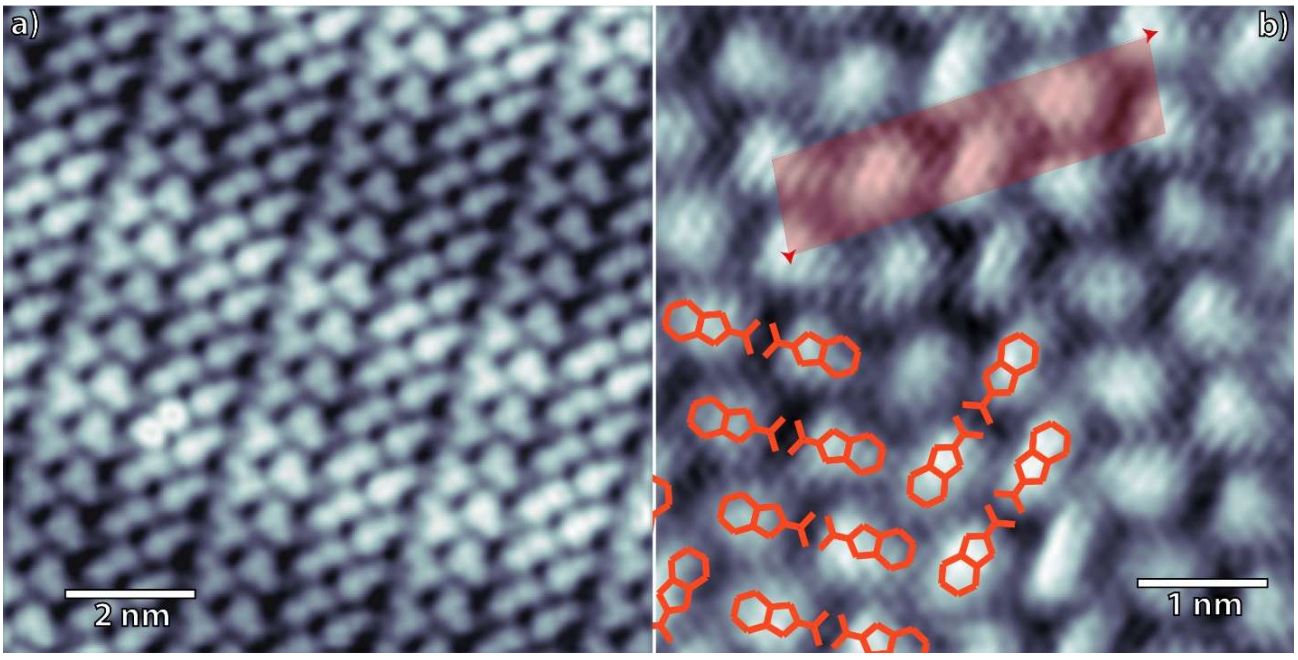

Figure 3.2: SAMN of I2CA on Au(111) in UHV. The I2CA forms a double-lamellar structure. The modulation of contrast in the images is due to the underlying herringbone reconstruction of the surface. (a) 10 nm image. (b) Detailed (5 nm) image, showing both a proposed molecular model and the unit cell of the structure. Image parameters: −1.40 V, −0.10 nA (a) and 0.81 V, 0.12 nA (b).

3.3.3 TCB/HOPG interface

The dominant structure formed from a solution of I2CA in TCB comprises a lamellar structure qualitatively similar to the one seen on Au(111) in UHV (Figure 3.3). Analysis of images containing both the molecular structure and the underlying HOPG lattice reveals epitaxial growth and allows the determination of the following epitaxy matrix:

$$\begin{pmatrix} \boldsymbol{u} \\ \boldsymbol{v} \end{pmatrix} = \begin{pmatrix} 0 & 3 \\ 15 & 5 \end{pmatrix} \begin{pmatrix} \boldsymbol{a_{HOPG}} \\ \boldsymbol{b_{HOPG}} \end{pmatrix}, \tag{3.1}$$

which corresponds to a unit cell with u=0.74 nm, v=3.25 nm, and γ=93.5°. The dimers in adjacent lamellae are inclined by differentangles,withalternatinglamellaeexhibiting+60° /−45° (±3°) tilts with respect to the lamellar long axis.

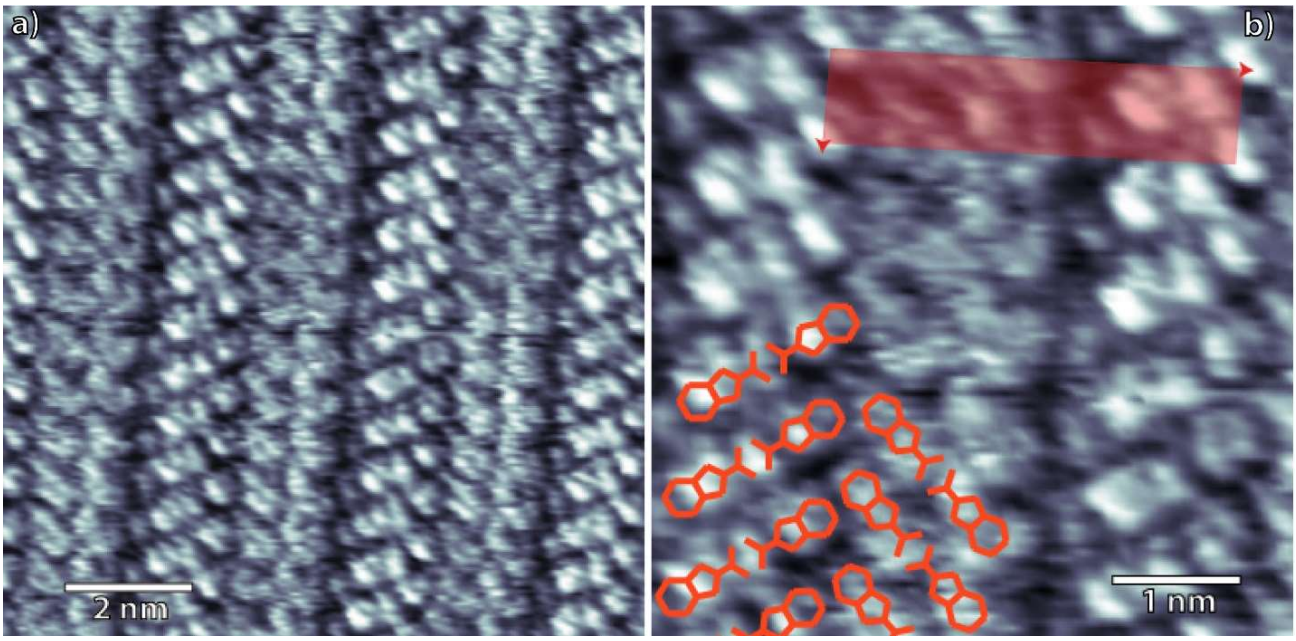

Figure 3.3: Double-lamellar SAMN of I2CA at the TCB/HOPG interface. (a) 10 nm image. (b) Detailed image (5 nm) showing proposed molecular models for the structure, along with a unit cell. Image parameters: −1.12 V, 0.2 nA (both images).

In a minority of experiments, we observed the formation of a structure in which each lamella contained I2CA dimers with identical tilt angles (Figure 3.4). In this case, the following epitaxy matrix describes the overlayer structure:

$$\begin{pmatrix} \boldsymbol{u} \\ \boldsymbol{v} \end{pmatrix} = \begin{pmatrix} 7 & 4 \\ 0 & -3 \end{pmatrix} \begin{pmatrix} \boldsymbol{a_{HOPG}} \\ \boldsymbol{b_{HOPG}} \end{pmatrix}. \tag{3.2}$$

This matrix corresponds to a unit cell with u=1.50 nm, v=0.74 nm, γ=94.7°. The dimers are tilted by 50° (±3°) with respect to the long lamellar axis.

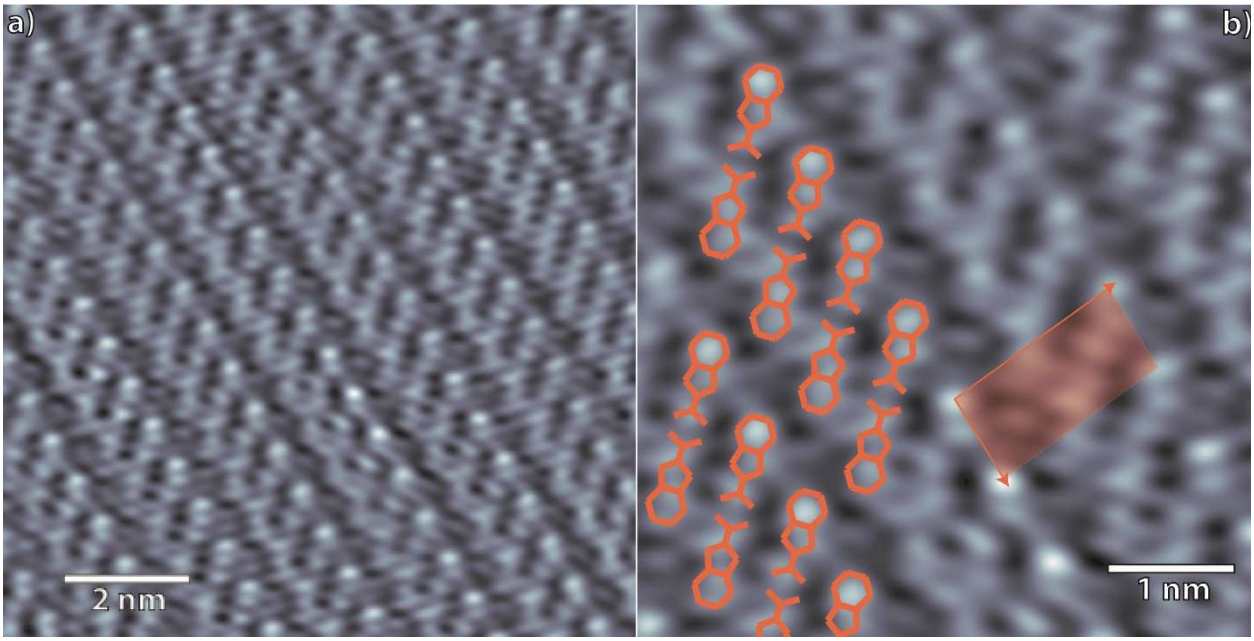

Figure 3.4: Single-lamellar structure of I2CA at the TCB/HOPG interface. (a) 10 nm image. (b) Detailed (5 nm) image, showing proposed molecular models and a unit cell. Image parameters: 0.59 V, 0.13 nA (both images).

3.3.4. Heptanoic acid/HOPG interface

Using heptanoic acid as the solvent, we observe a different structure on HOPG, as shown in Figure 3.5. The structure does not have the well-defined lamella seen at the TCB/HOPG interface. The image contrast suggests a pairing of I2CA molecules inconsistent with the –COOH dimerization seen on Au(111), or when TCB was used as a solvent. Images with substrate resolution allow us to identify the epitaxy matrix as

$$\begin{pmatrix} \boldsymbol{u} \\ \boldsymbol{v} \end{pmatrix} = \begin{pmatrix} 5 & -1 \\ 2 & 8 \end{pmatrix} \begin{pmatrix} \boldsymbol{a_{HOPG}} \\ \boldsymbol{b_{HOPG}} \end{pmatrix} \tag{3.3}$$

which corresponds to a unit cell with *u*=1.37, *v*=1.77 nm and γ=115°.

3.3.5 Calculated 2D molecular layer structures

Starting from the bonding geometries implied by our measurements at the TCB/HOPG interface, we performed DFT calculations of the 2D layer structures using periodic boundary conditions. The optimized calculated geometry for the structure corresponding to the chevron double lamellar structure observed on Au(111) and at the TCB/HOPG interface consists of one cis- and one trans-symmetric –COOH dimers, , shown in (d) in

Figure 3.6, and the structure constrained to the unit cell observed at the TCB/HOPG interface is shown in (b).

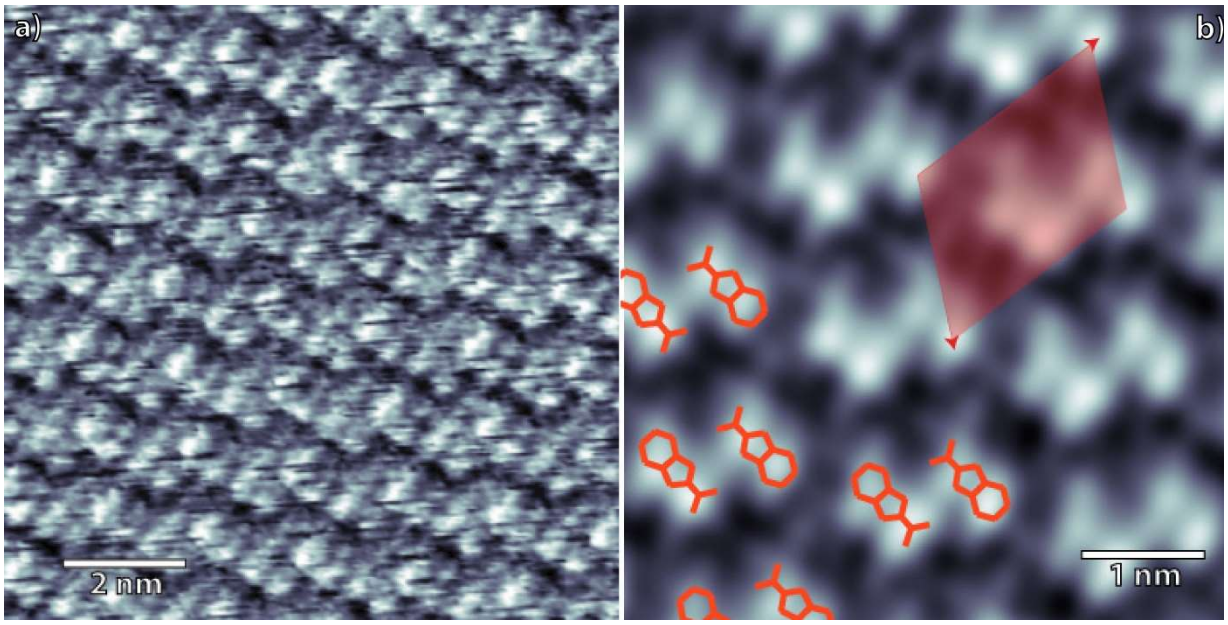

Figure 3.5: SAMN of I2CA at the heptanoic acid/HOPG interface. (a) 10 nm image. (b) Detailed (5 nm) image, with superimposed molecular models and a unit cell. Image parameters: −1.32 V, 0.15 nA (a) and −1.65 V, 0.15 nA (b).

The single- lamella structure observed at the TCB/HOPG interface with trans –COOH dimers is shown as (a) (constrained to the TCB/HOPG unit cell) and (c) (optimized) in Figure 3.6.

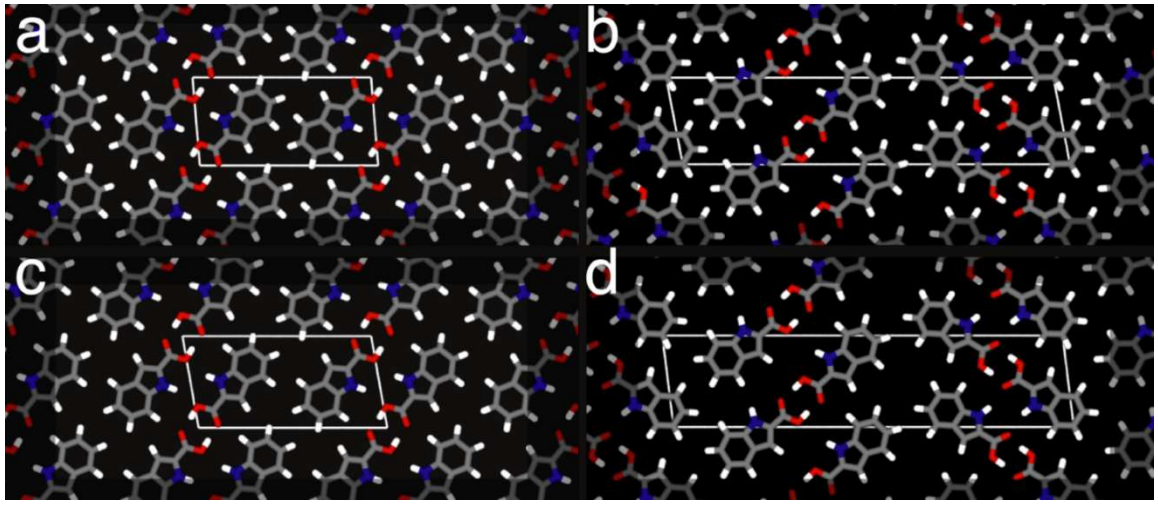

Figure 3.6: Results of DFT relaxations showing the minimum energy configurations for I2CA on HOPG for the (a) single lamella and (b) double lamella structures. The configuration for unconstrained unit cells in the same starting geometry is shown for (c) the single lamella and (d) double lamella structures. All the schematics are presented on the same scale, and the unit cell for each is outlined in white.

Table 3.2 reports the energetics and unit cells for these structures as well as both the total bonding energy and the *cohesive* energy (the energy required to assemble the candidate structure from hydrogen-bonded dimers). Because of the subtleties of the surface reconstruction, we did not consider the geometry observed on Au(111) in the calculations, but we note that the observed unit cell on Au(111) is quite close to the relaxed gasphase geometry and thus will produce total energies intermediate between those found using the observed HOPG unit cell and gas-phase relaxation.

TABLE 3.2. Summary of calculated unit cells for the two lamellar packing motifs of I2CA.

Unit cell	u (nm)	v (nm)	γ (deg)	Dimer tilt angle (deg)	Bond energy (kcal/mol per molecule)	Cohesive energy (kcal/mol per molecule)
Double lamellar structure						
HOPG unit cell	3.26	0.74	101	57.1/-46.4	-6.94	+1.29
Gas phase optimized	3.36	0.77	97.1	57.9/-48.3	-12.9	-4.59
Single lamellar structure-trans dimers						
HOPG unit cell	1.5	0.74	94.7	44.5	-7.73	+0.14
Gas phase optimized	1.58	0.78	100	46.4	-12.49	-4.62

3.4. Discussion

Cluster DFT calculations of dimeric and trimeric associations of I2CA reveal energetics consistent with those found for other carboxylated molecules.[16,25] Dimeric association via –COOH cyclic bonding leads to the most stable architecture. Of the different –COOH dimer conformations investigated, the strongest hydrogen bond energy is achieved for transsymmetric dimers of I2CA for which the monomers have their hydroxyl groups oriented towards the pyrrole nitrogen (Figure 3.1(e)). However, this geometry comprises a less-stable conformation of I2CA, and accordingly the lowest total energy structure is found for dimerization of the other I2CA isomer (Figure 3.1(c)). The offset dimer structures are less stable and have a large enough energy difference between the two I2CA isomers (−6.60 kcal/mol per molecule vs. −0.92 kcal/mol per molecule) that we can reasonably assume that only the structure shown in Figure 3.1(f) should be observable. The trimeric associations in Figures 3.1(h) and 3.1(i) are included mostly for interest, since these trimeric structures are unlikely to form extended two-dimensional films due to the difficulty in doing so at an adequate molecular density. The self-assembly of I2CA at surfaces is

consistent with the formation of expanded films of hydrogen bonded structures predicted from gas-phase DFT. On Au(111) in vacuum, and at the TCB/HOPG interface, the I2CA SAMN comprises the energetically favored –COOH dimers, which pack into ordered lamellae. However, even with the high-resolution imaging afforded by UHV, it was not possible to distinguish between the three possible dimer conformations shown in Figures 3.1(c)–3.1(e).

SAMN of I2CA at the heptanoic acid/HOPG interface. (a) 10 nm image. (b) Detailed (5 nm) image, with superimposed molecular models and a unit cell. Image parameters: −1.32 V, 0.15 nA (a) and −1.65 V, 0.15 nA (b).The I2CA molecules consistently appear pearshaped, with no evident asymmetry from which the position of the nitrogen could be inferred, and negligible contrast exists in the region of the –COOH bonds. The lamellar structures differ on Au(111) and HOPG. On Au(111), the short unit vector, which corresponds to the intralamellar spacing between dimers, is u=0.77 nm. This spacing is reduced on HOPG, where it is lattice-matched to three HOPG lattice constants (0.74 nm). This has implications for the interactions between the lamellae. On HOPG, the lamellae can stack symmetrically (Figure 3.4), leading to a molecular lattice vector v approximately half the length of the one observed on Au(111). The dimer tilt angle of 50° (±3°) is identical between the single lamellar structure on HOPG and the double-lamella structure on Au(111). In the double lamellar structure on HOPG (Figure 3.3), the 0.74 nm dimer spacing is retained, but the tilt angle is different in each of the two lamellae spanned by the unit cell (45°±3°/60±3°), which presumably minimizes the repulsive interactions between adjacent lamellae and leads to an expansion of the lattice along the direction perpendicular to the long axis of the lamellae (v=3.17 nm on Au(111), and v=3.25 nm on HOPG). For the single lamellar phase, observed on HOPG, DFT calculations in PBC show that the system must gain a significant energy contribution from surface interaction to stabilize itself; the predicted cohesive energy ($E_C=E_{Total} - 2E_{I2CA} - E_{dimer\text{-}Hbond}$) is positive, and thus this repulsive energy barrier must be overcome by molecule-substrate interactions. The calculated cohesive energy is somewhat less positive (almost zero) for the trans-symmetric –COOH dimers in the single lamellar geometry shown in Figure 3.6(a), due to intra-lamellar H-bonding channels between the N–H and COOH moieties available in this configuration. This holds even in the gas-phase optimized unit cell, where the (negative) cohesive energy is largest for this dimer conformation. The conformation of these dimers is analogous to the one shown in the cluster calculations (above), in Figure 3.1(e). The energetics in Table 3.1 do not

suggest this geometry as the most stable, but the cluster calculations do not account for the intra-lamellar bonding. The dimer tilt angle predicted for the geometry in Figure 3.6(a) is not within the error bars of the measurement, but this is also the case for all of the other candidate geometries (see supplementary material[39]). Nevertheless, the results of the total energy calculations in periodic boundary conditions strongly suggest that the single lamellar structure observed in our experiments comprises the trans-dimer configuration predicted as less favorable by the cluster calculations. The double-lamellar structure contains four molecules in its unit cell, which gives sixteen possible geometrical conformations for each of the dimers. All of these geometries were relaxed in both fixed (corresponding to the observed epitaxy matrix on HOPG) and variable cell geometries. We find the lowest energy structure in both cases corresponds to a unit cell containing one cis- and one trans-dimer pair, as shown in Figures 3.6b and 3.6d. When constrained to the unit cell observed on HOPG, this geometry was found to be 0.52 kcal/mol per molecule more stable than the next most favorable conformation, which suggests this geometry should dominate at room temperature. For calculations where the unit cell was allowed to relax, the energetic difference between geometries is much smaller (see supplementary material[39] section 3.6.2). The energy penalties for forming the ordered 2D layers are largely governed by van der Waals interactions between dimer pairs, while the OH···O bonding length is found to vary between 2% and 10% between the constrained and unconstrained unit cell geometries; the increase in unit cell area cannot be explained by lengthening of these bonds alone. The cohesive energy for the single-lamellar structure is calculated to be significantly more positive than for the double-lamellar structure, and based on this consideration alone, it is not surprising that it is only observed occasionally. However, its inverse areal density of 0.55 nm^2/molecule is somewhat smaller than the 0.59 nm^2/molecule observed for the double-lamellar structure, indicating that the energy gained from adsorption is higher in the single-lamellar geometry. It is also possible that kinetic limitations may drive the growth of these types of domains once seeded, with the energy barrier associated with converting a single-lamellar domain to double-lamellar too high to be crossed at the temperatures involved in these experiments. The drastically different molecular geometry observed at the heptanoic acid/HOPG interface must be attributable to the choice of solvent. The coadsorption of heptanoic acid and its analogues has previously been observed in a number of self-assembled systems at the solution/solid interface.[16,17,50–53] Some of this previous work reports structures that are interpreted in the

context of coadsorbed solvent molecules, even though the latter are difficult to unambiguously resolve in STM images.[16,17,53] In the present case, the energetics of the observed structure are intractable in the absence of coadsorbed solvent molecules: the hydrogen bond energy of the most stable OH···N dimer is still 3.57 kcal/mol per molecule weaker than the bond energy of the OH···O dimer, and the large unit cell reduces the areal density of I2CA by one-half compared to the single lamellar structure on HOPG, shown in Figure 3.5 (0.55 nm^2 per molecule in TCB compared to 1.10 nm^2 per molecule in heptanoic acid). Clearly, these deficiencies in intermolecular and substrate-molecule enthalpies must be compensated for the structure to be energetically feasible (and therefore observable). Hence, we postulate the adsorption of heptanoic acid on the HOPG surface (a possible geometry is given in the supplementary material[39]). In this way, the total bond enthalpy of the SAMN becomes more favorable, and the total molecular density on the surface is increased.

3.5 Conclusions

Indole-2-carboxylic acid self-assembles to form ordered SAMNs on both HOPG and Au(111). The molecules form hydrogen-bonded assemblies built from molecular dimers. On both Au(111) (in UHV) and at the TCB/HOPG interface, OH···O bonded I2CA dimers pack tightly on the surface, forming long lamellar structures that exhibit slight differences in the lamellar stacking due to the differing epitaxial constraints on the two surfaces. In the presence of the carboxylated solvent heptanoic acid, a different phase is formed. The large spacing between the OH···N bonded I2CA dimers implies that the heptanoic acid solvent coadsorbs with the I2CA. All of the observed substrates have substrate-commensurate unit cells. Total energy calculations suggest that substrate epitaxy drives the assembly of the overlayers; in the absence of the substrate, cohesive energy calculations show that a 2D assembly is unlikely to be stable. Energetic considerations lead us to predict that the double-lamellar structure contains one cis- and one trans-symmetric dimer in the unit cell, while the single lamellar structure contains a single trans-symmetric –COOH dimer, but in a conformation predicted to be less stable in single dimer calculations. These suppositions cannot be verified by our STM images, which do not distinguish the orientation of the indole. The double lamellar structure is calculated to be more favorable than the single lamellar structure, but occasional observation of the latter can be explained by its slightly more favorable packing density and/or by kinetic considerations. Our new insights on the

self-assembly process in H-bonded indole molecular building blocks contribute to establish guidelines to engineer the molecular structure of the building blocks for organic bioelectronic applications, e.g., protonic devices and implantable electrodes, and contribute to advance the knowledge on the functions of materials obtained from indole building blocks in biological systems. Further work focused on the investigation of the temperature stability of these structures, both in UHV and at the solution/solid interface,[54,55] would give more details about the thermodynamics underlying the system.

3.6 Supporting information

3.6.1 Calibration of STM images

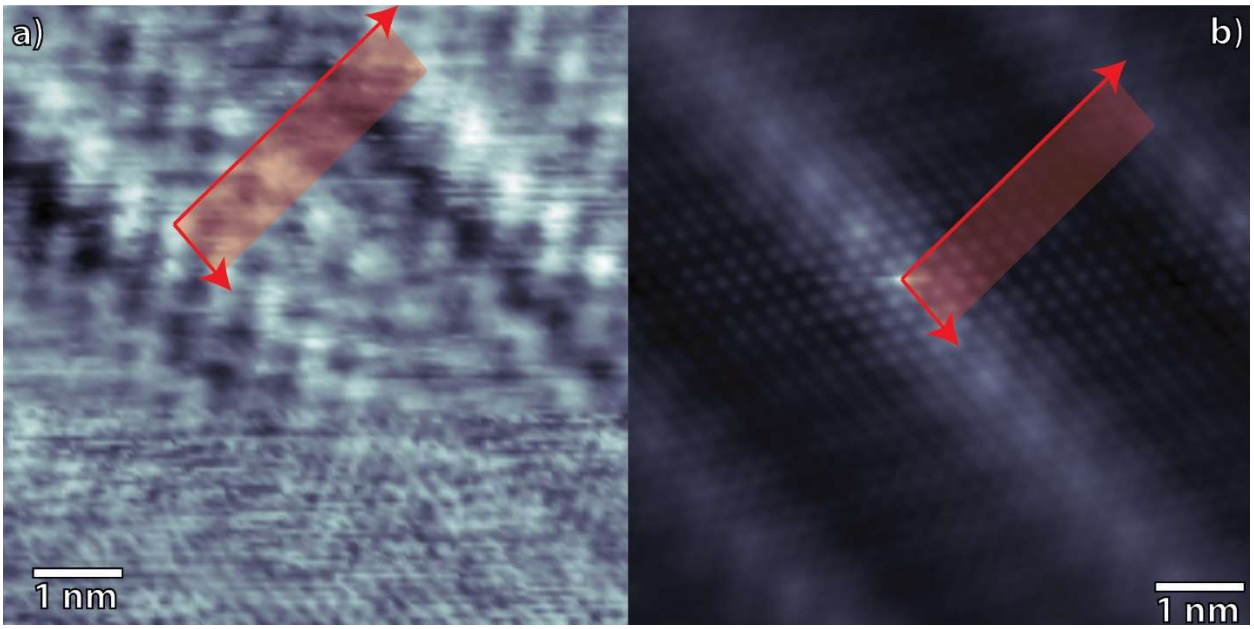

Figure 3.7: Unit cell determination of I2CA on TCB/HOPG for double lamella. a) The STM parameters are toggled from V_b=-19mV, I_t = 2.0 nA to V_b=-600 mV, I_t = 0.15 nA as the image is scanned from bottom to top. b) Autocorrelation of the image in a. The enhancement of the periodicities inherent in the image allow the easy reading-off of the molecular unit cell, from the bright points overlaid on the HOPG periodicity. The unit cell, shown in red, is identical in both a and b parts.

For all overlayers observed, the STM data were calibrated by creating conditions where the substrate lattice and the molecular lattice were observed in the same image, by switching the bias voltage and tunelling current settings partway through the acquisition. Typically molecular lattices are observed at large values of the bias voltage and small tunnel currents (leading to an increased tip-sample gap), whereas the substrate is

observed at small bias voltages and high tunneling current (giving a decreased tip-sample gap).

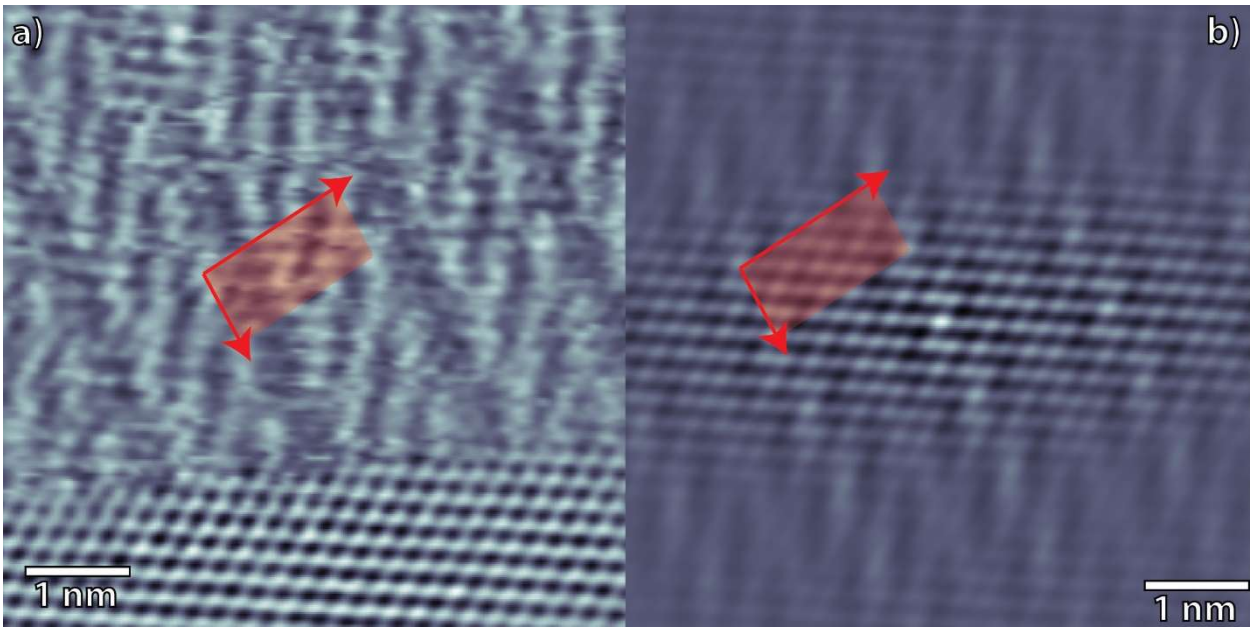

Figure 3.8: Unit cell determination of I2CA on TCB/HOPG for single lamella. a) The STM parameters are toggled from V_b=-19mV, I_t = 2.0 nA to V_b=700 mV, I_t = 0.13 nA as the image is scanned from bottom to top. b) Autocorrelation of the image in a. The enhancement of the periodicities inherent in the image allow the easy reading-off of the molecular unit cell, from the bright points overlaid on the HOPG periodicity. The unit cell, shown in red, is identical in both a and b parts.

For overlayers on HOPG, where the substrate presents no reconstruction, an autocorrelation filter applied to may be employed to determine the exact epitaxy matrix for a given overlayer. An example is presented in Figure 3.7 for I2CA in TCB at the solution/solid interface. This method allows the reconstruction matrix to be easily read off the autocorrelation filter without need for correcting for drift or creep artifacts, if present.

For calibration of molecular overlayers on Au(111), the same procedure for data collection is applied. However, due to the large unit cell of the (22×√3) reconstruction, it is not possible to use the above technique to determine an exact epitaxy matrix, because a precise determination requires many repeated molecular periods along a single soliton direction, and it is not experimentally tractable to collect such data. Instead, we corrected the instrumental distortion of the STM by fitting a (22×√3) cell to the region where the gold lattice is visible, as shown in Figure 3.8. The molecular unit cell was then determined by hand from this corrected image.

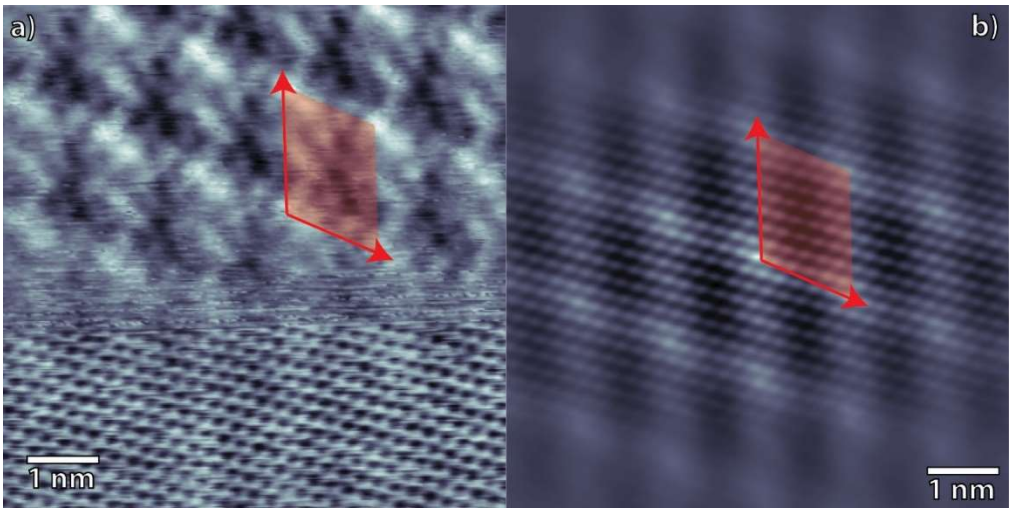

Figure 3.9: Unit cell determination of I2CA on heptanoic acid/HOPG. a) The STM parameters are toggled from V_b=-19mV, I_t = 2.0 nA to V_b=-1300 mV, I_t = 0.15 nA as the image is scanned from bottom to top. b) Autocorrelation of the image in a. The enhancement of the periodicities inherent in the image allow the easy reading-off of the molecular unit cell, from the bright points overlaid on the HOPG periodicity. The unit cell, shown in red, is identical in both a and b parts.

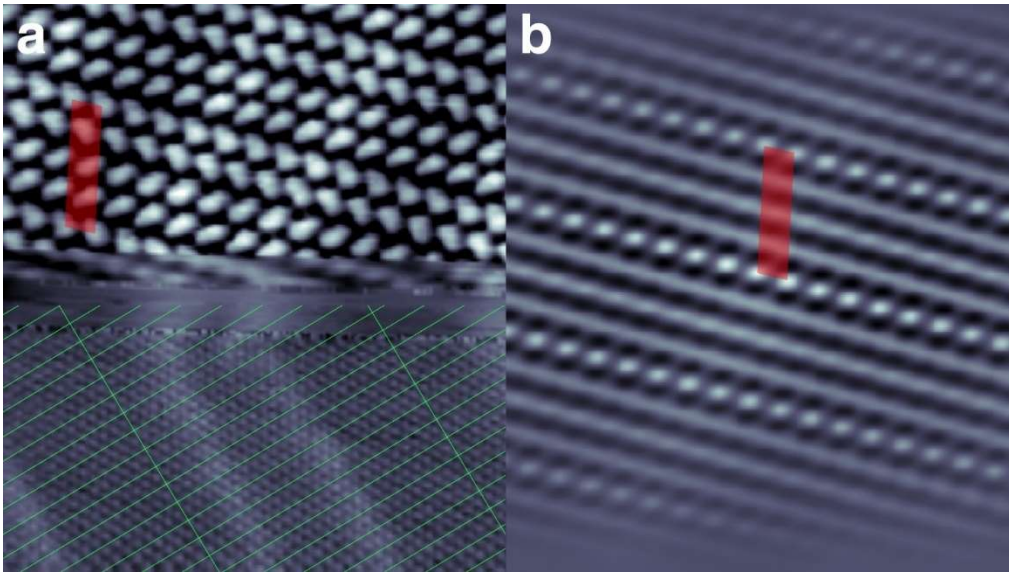

Figure 3.10: Calibration of STM images on Au(111). a) STM image where the bias voltage is changed partway through acquisition. At the bottom of the image the (22×√3) is clearly visible, and the image has been corrected to these known dimensions (green lines), where 23 surface atoms are contained within each unit cell. b) Autocorrelation of the image in a). The molecular unit cell can easily be determined from the position of the bright features. The same unit cell (in red) is overlaid on both images.

3.6.2 Full results of 2D relaxations

The STM data give the approximate location and orientation of the molecules, but are not able to resolve the adsorption geometry, particularly the relative orientation of the pyrrole group. To determine the most stable conformation of the trans vs cis dimer pairing in both the single-lamellar and double-lamellar structure, we examined the full set of permuted structures. We adopt a shorthand notation as illustrated by the schematic in Figure 3.9 to keep track of the permutations.

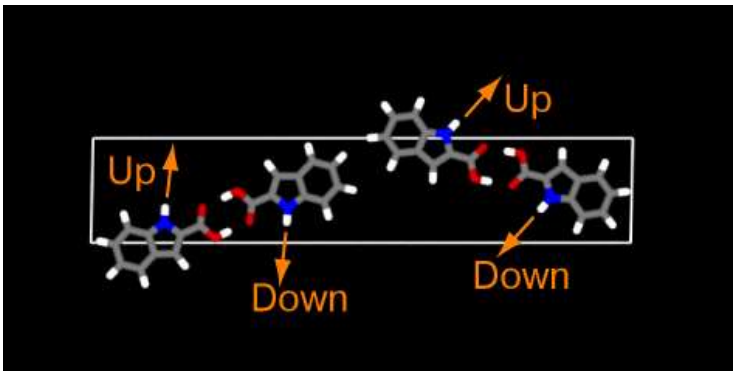

Figure 3.11: Details of nomenclature for each of the dimer pairing geometries in the double lamellar structure. The arrows indicate the direction of the N-H group in the pyrrole ring. This conformation is assigned the shorthand notation "UDUD" for "up-down-up-down".

The energetics are summarized in the tables below. The total binding energy (E_B) is computed via the standard relation $E_B = E_{Total} – nE_{I2CA}$, where E_{Total} is the total energy per unit cell, E_{I2CA} is the energy of a single I2CA molecule, and n is the number of molecules per unit cell. The cohesive energy (E_C) is calculated by EC = ETotal - n_{UU}EUU – n_{DD}EDD-$n_{UD}E_{UD}$, where n_{UU}, n_{DD}, n_{UD}, E_{UU}, E_{DD}, and E_{UD} are the numbers and energies of each type of trans/cis dimer conformation in the unit cell. The results of the fixed-cell calculations (corresponding to the geometry observed on HOPG) are summarized in Table S 1 for the double-lamellar structure and in Table S 3 for the single-lamellar structure. The total energies and final unit cell geometries are reported in Table S 2 for the double-lamellar structure and in Table S 4 for the single-lamellar structure. All of the four following tables are calculated in the GGA using the PBE/VDW-DF functional. The geometries do not reflect permutations involving dihedral twists of the COOH groups; test cases show that the changes in energy between identical geometries with flipped carboxylic acid groups are of the order of 0.2 kcal/mol/molecule, significantly less than the energies involved in trans/cis permutations of the whole molecule.

Table 3.3: Total energy calculations for relaxation of the double-lamellar conformation in a fixed cell corresponding to the observed epitaxy matrix on HOPG. The highlighted green row is the most stable conformation, and is the one presented in the manuscript.

Conformation	Binding energy (kcal/mol/molecule)	Cohesive energy (kcal/mol/molecule)
DDDD	-5.38	+2.83
DDDU	-5.22	+3.05
DDUD	-6.41	+1.86
DDUU	-5.77	+2.41
DUDD	-5.53	+2.74
DUDU	-5.03	+3.28
DUUD	-6.33	+1.98
DUUU	-6.09	+2.14
UDDD	-5.62	+2.65
UDDU	-4.56	+3.75
UDUD	-6.42	+1.89
UDUU	-5.06	+3.16
UUDD	-5.62	+2.56
UUDU	-4.66	+3.57
UUUD	-6.94	+1.28
UUUU	-5.54	+2.61

Table 3.4: Total energies and geometries of variable-cell calculations for the double-lamellar structures. The rows highlighted in green represent the lowest energy structures within kT at room temperature.

Conformation	Binding energy (kcal/mol/molecule)	Cohesive energy (kcal/mol/molecule)	*u* (nm)	*v* (nm)	γ (°)
DDDD	-12.05	-3.84	3.40	0.77	97.0
DDDU	-12.08	-3.82	3.41	0.76	97.3
DDUD	-12.33	-4.06	3.40	0.76	97.3
DDUU	-12.32	-4.14	3.42	0.76	97.3
DUDD	-12.22	-3.95	3.38	0.77	97.8
DUDU	-12.37	-4.06	3.40	0.77	97.2
DUUD	-12.90	-4.59	3.32	0.77	96.1
DUUU	-12.67	-4.44	3.38	0.77	96.4
UDDD	-11.98	-3.71	3.41	0.76	97.3
UDDU	-11.79	-3.47	3.43	0.76	96.7
UDUD	-12.29	-3.98	3.39	0.76	97.6
UDUU	-11.87	-3.64	3.40	0.76	97.5
UUDD	-12.40	-4.22	3.39	0.77	97.0
UUDU	-12.07	-3.84	3.40	0.77	97.0
UUUD	-12.71	-4.48	3.36	0.77	97.1
UUUU	-12.22	-4.08	3.37	0.77	97.3

Table 3.5: Total energy calculations for relaxation of the single-lamellar conformation in a fixed cell corresponding to the observed epitaxy matrix on HOPG. The highlighted green row is the most stable conformation, and is the one presented in the manuscript.

Conformation	Binding energy (kcal/mol/molecule)	Cohesive energy (kcal/mol/molecule)	Dimer tilt angle (°)
DD	-5.81	2.41	45.6
UD	-3.95	4.36	46.7
DU	-7.73	0.14	44.5
UU	-5.83	2.31	45.4

Table 3.6: Total energies and geometries of variable-cell calculations for the single-lamellar conformation.

Conformation	Binding energy (kcal/mol/molecule)	Cohesive energy (kcal/mol/molecule)	*u* (nm)	*v* (nm)	γ (°)
DD	-12.02	-3.80	1.60	0.77	99.7
UD	-11.62	-3.30	1.61	0.78	100.1
DU	-12.49	-4.62	1.58	0.78	100.0
DU	-12.20	-4.06	1.60	0.78	100.6

3.6.3 Effect of VDW-DF density functional

The same geometries were all calculated using the standard PBE exchange correlation functional without vdW-DF, to assess what role the van der Waals forces might have in stabilizing the observed geometries. The results of the optimizations are found in the following tables, which follow the same form and use the same shorthand as the ones above. Overall we find no significant change in the trends, in that the same geometries predicted to be most energetiacally stable with vdW-DF are also predicted to be the most stable with PBE alone.

Table 3.7: Total energy calculations for relaxation of the double-lamellar conformation in a fixed cell corresponding to the observed epitaxy matrix on HOPG, using the standard PBE exchange-correlation functional (without the vdW-DF density functional).

Conformation	Binding energy (kcal/mol/molecule)	Cohesive energy (kcal/mol/molecule)
DDDD	-4.86	4.71
DDDU	-4.69	5.00
DDUD	-5.81	3.87
DDUU	-5.09	4.48
DUDD	-5.13	4.55
DUDU	-4.69	5.09
DUUD	-5.77	4.01
DUUU	-5.56	4.10
UDDD	-5.19	4.49
UDDU	-4.10	5.68
UDUD	-5.87	3.92
UDUU	-4.58	5.09
UUDD	-5.39	4.17
UUDU	-4.26	5.41
UUUD	-6.30	3.36
UUUU	-5.08	4.48

Table 3.8: Total energies and geometries of variable-cell calculations for the double-lamellar structures, using the standard PBE exchange-correlation functional (without the vdW-DF density functional).

Conformation	Binding energy (kcal/mol/molecule)	Cohesive energy (kcal/mol/molecule)	*u* (nm)	*v* (nm)	γ (°)
DDDD	-10.46	-0.88	3.32	0.78	96.0
DDDU	-10.43	-0.99	3.38	0.78	96.7
DDUD	-10.62	-0.94	3.40	0.78	96.5
DDUU	-10.87	-1.31	3.36	0.78	96.8
DUDD	-10.68	-1.24	3.40	0.79	96.8
DUDU	-10.59	-1.30	3.39	0.78	97.2
DUUD	-10.96	-1.42	3.42	0.78	97.3
DUUU	-10.93	-1.51	3.37	0.78	96.5
UDDD	-10.31	-0.63	3.37	0.77	97.1
UDDU	-10.20	-0.66	3.41	0.77	97.6
UDUD	-10.46	-0.68	3.40	0.78	96.7
UDUU	-10.13	-0.46	3.43	0.77	97.1
UUDD	-10.79	-1.22	3.38	0.78	97.3
UUDU	-10.36	-0.94	3.41	0.78	96.9
UUUD	-10.86	-1.19	3.38	0.79	96.0
UUUU	-10.59	-1.04	3.40	0.77	97.7

Table 3.9: Total energy calculations for relaxation of the single-lamellar conformation in a fixed cell corresponding to the observed epitaxy matrix on HOPG, using the standard PBE exchange-correlation functional (without the vdW-DF density functional).

Conformation	Binding energy (kcal/mol/molecule)	Cohesive energy (kcal/mol/molecule)	Dimer tilt angle (°)
DD	-5.03	4.52	45.4
DU	-3.16	6.14	43.9
UD	-6.97	2.81	46.3
UU	-5.10	4.48	45.3

Table 3.10: Total energies and geometries of variable-cell calculations for the single-lamellar conformation, using the standard PBE exchange-correlation functional (without the vdW-DF density functional).

Conformation	Binding energy (kcal/mol/molecule)	Cohesive energy (kcal/mol/molecule)	*u* (nm)	*v* (nm)	γ (°)
DD	-9.90	-0.35	1.60	0.79	101.0
UD	-10.18	-0.40	1.60	0.78	100.7
DU	-10.63	-1.33	1.59	0.77	100.4
DU	-10.32	-0.75	1.58	0.78	100.7

3.7 Chapter bibliography

1. S. De Feyter and F. C. De Schryver, *Chem. Soc. Rev,* 2003, **32**, 139-150.
2. R. Otero, J. M. Gallego, A. L. V. de Parga, N. Martín, and R. Miranda, *Adv. Mater,* 2011, **23**, 5148-5176
3. F. Cicoira, C. Santato, and F. Rosei, *Top. Curr. Chem,* 2008, **285**, 203-267.
4. F. Rosei, M. Schunack, Y. Naitoh, P. Jiang, A. Gourdon, E. Laegsgaard, I. Stensgaard, C. Joachim, and F. Besenbacher, *Prog. Surf. Sci,* 2003, **71**, 95-146.
5. J. V. Barth, *Annu. Rev. Phys. Chem,* 2007, 58, 375-407 .
6. M. Lackinger, S. Griessl, T. Markert, F. Jamitzky, and W. M. Heckl*, J. Phys. Chem. B,* 2004, **108**, 13652-13655.
7. O. Ivasenko and D. F. Perepichka, *Chem. Soc. Rev,* 2011, **40**, 191-206.
8. M. Lackinger and W. M. Heckl, *Langmuir,* 2009, **25**, 11307-11321.
9. I. Cebula, E. F. Smith, M. D. Gimenez-Lopez, S. H. Yang, M. Schroder, N. R. Champness, and P. H. Beton, *J. Phys. Chem. C,* 2013, **117**, 18381-18385.
10. T. SchmitzHubsch, T. Fritz, F. Sellam, R. Staub, and K. Leo, *Phys. Rev.* B, 1997, **55**, 7972-7976.
11. A. Hoshino, S. Isoda, H. Kurata, and T. Kobayashi, *J. Appl. Phys*, 1994, **76**, 4113-4120.
12. R. Strohmaier, C. Ludwig, J. Petersen, B. Gompf, and W. Eisenmenger, *Surf. Sci,* 1996, **351**, 292-302.
13. S. Mannsfeld, M. Toerker, T. Schmitz-Hubsch, F. Sellam, T. Fritz, and K. Leo, *Org. Electron,* 2001, **2**, 121-134.
14. Y. C. Ye, W. Sun, Y. F. Wang, X. Shao, X. G. Xu, F. Cheng, J. L. Li, and K. Wu, *J. Phys. Chem. C,* 2007, **111**, 10138-10141.
15. S. Griessl, M. Lackinger, M. Edelwirth, M. Hietschold, and W. M. Heckl, *Single Mol,* 2002, **3**, 25-31.
16. J. M. MacLeod, Z. Ben Chaouch, D. F. Perepichka, and F. Rosei, *Langmuir,* 2013, **29**, 7318-7324.
17. J. F. Dienstmaier, K. Mahata, H. Walch, W. M. Heckl, M. Schmittel, and M. Lackinger, *Langmuir, 2010,* **26**, 10708-10716.
18. R. Gutzler, S. Lappe, K. Mahata, M. Schmittel, W. M. Heckl, and M. Lackinger, *Chem. Commun,* 2009, 680-682.
19. C. Heininger, L. Kampschulte, W. A. Heckl, and M. Lackinger, *Langmuir, 2009,* **25**, 968-972.
20. N. Zhu, T. Osada, and T. Komeda, Surf. Sci, 2007, **601**, 1789–1794.
21. Y. L. Yang, K. Deng, Q. D. Zeng, and C. Wang, *Surf. Interface Anal, 2006,* **38**, 1039-1046.
22. H. Dang, T. Maris, J. H. Yi, F. Rosei, A. Nanci, and J. D. Wuest, *Langmuir,* 2007, **23**, 11980- 11985.
23. S. De Feyter, A. Gesquiere, P. C. M. Grim, F. C. De Schryver, S. Valiyaveettil, C. Meiners, M. Sieffert, and K. Mullen, *Langmuir,* 1999, **15**, 2817-2822.
24. J. Adisoejoso, K. Tahara, S. Okuhata, S. Lei, Y. Tobe, and S. De Feyter, *Angew. Chem, Int. Ed,* 2009, **48**, 7353-7357.
25. J. M. MacLeod, O. Ivasenko, C. Fu, T. Taerum, F. Rosei, and D. F. Perepichka, *J. Am. Chem. Soc,* 2009, **131**, 16844-16850.
26. Y. G. Kim, S. L. Yau, and K. Itaya, *Langmuir,* 1999, **15**, 7810-7815.
27. L.-P. Xu, Y. Liu, J. Zhao, S. Wang, C.-S. Lin, R.-Q. Zhang, Y. Wen, H. Du, and X. Zhang, J. *Nanosci. Nanotechnol,* 2013, **13**, 1226-1231.

28. A. Duong, M. A. Dubois, and J. D. Wuest, *Langmuir,* 2010, **26**, 18089-18096.
29. N. A. Wasio, R. C. Quardokus, R. P. Forrest, C. S. Lent, S. A. Corcelli, J. A. Christie, K. W. Henderson, and S. A. Kandel, *Nature,* 2014, **507**, 86-89.
30. R. C. Quardokus, N. A. Wasio, J. A. Christie, K. W. Henderson, R. P. Forrest, C. S. Lent, S. A. Corcelli, and S. A. Kandel, *Chem. Commun,* 2014, **50**, 10229-10232.
31. T. Tonohiro, T. Kaneko, M. Tanabe, and N. Iwata, Gen. Pharmacol.: *Vasc. Syst,.* 1997, **28**, 555-560.
32. J. Huettner, *Science,* 1989, **243**, 1611-1613.
33. N. K. Kaushik, N. Kaushik, P. Attri, N. Kumar, C. H. Kim, A. K. Verma, and E. H. Choi, *Molecules,* 2013, **18**, 6620-6662.
34. S. P. Nighswander-Rempel, S. Olsen, I. B. Mahadevan, G. Netchev, B. C. Wilson, S. C. Smith, H. Rubinsztein-Dunlop, and P. Meredith, *Photochem. Photobiol,* 2008, **84**, 613-619.
35. G. Tourillon and F. Garnier, *J. Electroanal. Chem*. *Interfacial Electrochem*, 1982, **135**, 173-178.
36. B. B. Berkes and G. Inzelt, *Electrochim. Acta,* 2014, **122**, 11-15.
37. J. V. Barth, H. Brune, G. Ertl, and R. J. Behm, Phys. Rev. B, 1990, **42**, 9307-9318.
38. I. Horcas, R. Fernandez, J. M. Gomez-Rodriguez, J. Colchero, J. GomezHerrero, and A. M. Baro, *Rev. Sci. Instrum*, 2007, **78**, 013705.
39. See supplementary material at http://dx.doi.org/10.1063/1.4908143 for additional information about STM image calibration and energy calculation.
40. M. J. Frisch, G. W. Trucks, H. B. Schlegel, G. E. Scuseria, M. A. Robb, J. R. Cheeseman, G. Scalmani, V. Barone, B. Mennucci, G. A. Petersson, H. Nakatsuji, M. Caricato, X. Li, H. P. Hratchian, A. F. Izmaylov, J. Bloino, G. Zheng, J. L. Sonnenberg, M. Hada, M. Ehara, K. Toyota, R. Fukuda, J. Hasegawa, M. Ishida, T. Nakajima, Y. Honda, O. Kitao, H. Nakai, T. Vreven, J. A. Montgomery, J. E. Peralta, F. Ogliaro, M. Bearpark, J. J. Heyd, E. Brothers, K. N. Kudin, V. N. Staroverov, R. Kobayashi, J. Normand, K. Raghavachari, A. Rendell, J. C. Burant, S. S. Iyengar, J. Tomasi, M. Cossi, N. Rega, J. M. Millam, M. Klene, J. E. Knox, J. B. Cross, V. Bakken, C. Adamo, J. Jaramillo, R. Gomperts, R. E. Stratmann, O. Yazyev, A. J. Austin, R. Cammi, C. Pomelli, J. W. Ochterski, R. L. Martin, K. Morokuma, V. G. Zakrzewski, G. A. Voth, P. Salvador, J. J. Dannenberg, S. Dapprich, A. D. Daniels Farkas, J. B. Foresman, J. V. Ortiz, J. Cioslowski, and D. J. Fox, GAUSSIAN 09, Revision B.01, Gaussian, Inc., Wallingford, CT, 2009.
41. P. Giannozzi, S. Baroni, N. Bonini, M. Calandra, R. Car, C. Cavazzoni, D. Ceresoli, G. L. Chiarotti, M. Cococcioni, I. Dabo, A. Dal Corso, S. de Gironcoli, S. Fabris, G. Fratesi, R. Gebauer, U. Gerstmann, C. Gougoussis, A. Kokalj, M. Lazzeri, L. Martin-Samos, N. Marzari, F. Mauri, R. Mazzarello, S. Paolini, A. Pasquarello, L. Paulatto, C. Sbraccia, S. Scandolo, G. Sclauzero, A. P. Seitsonen, A. Smogunov, P. Umari, and R. M. Wentzcovitch*, J. Phys.: Condens. Matter* 2009 **21**, 395502.
42. J. P. Perdew, K. Burke, and M. Ernzerhof, *Phys. Rev. Lett*, 1996, **77**, 3865-3868.
43. M. Dion, H. Rydberg, E. Schroder, D. C. Langreth, and B. I. Lundqvist, *Phys. Rev. Lett*, 2004, **92**, 246401. T. Thonhauser, V. R. Cooper, S. Li, A. Puzder, P. Hyldgaard, and D. C. Langreth, *Phys. Rev. B,* 2007, **76**, 125112.
44. G. Roman-Perez and J. M. Soler, *Phys. Rev. Lett,* 2009, **103**, 096102.
45. K. Momma and F. Izumi, *J. Appl. Crystallogr*, 2011, **44**, 1272- 1276.
46. A. Kokalj, Comput. *Mater. Sci*, 2003, **28**, 155-168.
47. F. Hanke and J. Björk, *Phys. Rev. B*, 2013, **87**, 235422. pdf
48. S. Clair, S. Pons, A. P. Seitsonen, H. Brune, K. Kern, and J. V. Barth, *J. Phys. Chem. B,* 2004, **108**, 14585-14590.

49. T. Sirtl, W. Song, G. Eder, S. Neogi, M. Schmittel, W. M. Heckl, and M. Lackinger, *ACS Nano,* 2013, **7**, 6711-6718.
50. F. Tao, J. Goswami, and S. L. Bernasek, *J. Phys. Chem B,* 2006, **110**, 19562-19569.
51. K. S. Mali, K. Lava, K. Binnemans, and S. De Feyter, *Chem. - Eur. J*, 2010, **16**, 14447-14458.
52. R. Gatti, J. M. MacLeod, J. Lipton-Duffin, A. G. Moiseev, D. F. Perepichka, and F. Rosei*, J. Phys. Chem. C,* 2014, **118**, 25505- 25516.
53. J. M. MacLeod and F. Rosei, *Aust. J. Chem,* 2011, **64**, 1299-1300.
54. K. Doi, H. Takeuchi, R. Nii, S. Akamatsu, T. Kakizaki, and S. Kawano, *J. Chem. Phys*, 2013, **139**, 085102.

CHAPTER 4: THE REACTIVITY OF DHI CATECHOL GROUP

Following our investigation on I2CA, we have confirmed that indole precursors adsorb planarly on the Au(111) surface. We have also seen that side interactions given by the pyrrole ring allow the formation stable of 2D networks, and that the interaction with the surface plays a major role in the absorption of the molecule. Armed with this increased knowledge, we are now ready to study indole molecules with more complex functionalization. We have investigated the self-assembly of DHI, this time only in the UHV since the molecule is prone to polymerization if left in air. This particular behaviour encouraged us to investigate more reactive surface, such as the Ag(111), and to attempt a controlled polymerization by exposure to O_2 gas.

For this work, I share the first author contribution with Mr. Gianluca Galeotti, as we have acquired the experimental dataset together. Dr. Ebrahimi and Dr. Macleod both supervised the experimental work, and supported our hypothesis with gas-phase PBC calculations. Dr. Pezzella helped us by providing fresh molecular precursor as well as sharing his experience on eumelanin polymerization. Prof. Tornau and Dr. Simenas instead worked on the MC modelling of the DHI system.

Room-temperature surface-assisted reactivity of a melanin precursor: silver metal-organic coordination versus covalent dimerization on gold

Published in Nanoscale, 11, 5422 (2019); doi: 10.1039/ C8NR09810G

F. De Marchi,[1] G. Galeotti,[1] M. Simenas,[2] E. E. Tornau,[3] A. Pezzella,[4,5] J. MacLeod,[6] M. Ebrahimi[1] and F. Rosei[1,7]

[1]Centre Energie, Materiaux et Telecommunications, Institut National de la Recherche Scientifique, 1650 Boulevard Lionel-Boulet, Varennes, QC, Canada J3X 1S2.

[2]Faculty of Physics, Vilnius University, Saulėtekio 9, LT-10222 Vilnius, Lithuania

[3]Semiconductor Physics Institute, Center for Physical Sciences and Technology, Saulėtekio 3, LT-10222 Vilnius, Lithuania

[4]Institute for Polymers, Composites and Biomaterials (IPCB), CNR, Via Campi Flegrei 34, I-80078 Pozzuoli (NA), Italy

[5]National Interuniversity Consortium of Materials Science and Technology (INSTM), Florence 50121, Italy

[6]School of Chemistry, Physics and Mechanical Engineering and Institute for Future Environments, Queensland University of Technology (QUT), 2 George Street, Brisbane, 4001 QLD, Australia.

[6]Institute for Fundamental and Frontier Science, University of Electronic Science and Technology of China, Chengdu 610054, PR China

Abstract

The ability of catecholamines to undergo oxidative self-polymerization enables an attractive preparation route of coatings for biotechnology and biomedicine applications. However, efforts toward developing a complete understanding of the mechanism that underpins polymerization have been hindered by the multiple catechol crosslinking reaction pathways that occur during the reaction. Scanning tunneling microscopy allows the investigation of small molecules in a reduced-complexity environment, providing important insight into how the intermolecular forces drive the formation of supramolecular assemblies in a controlled setting. Capitalizing on this approach, we studied the self-assembly of 5,6 dihydroxy-indole (DHI) on Au(111) and Ag(111) to investigate the interactions that affect two-dimensional growth mechanism and to elucidate the behavior of the catechol group on these two surfaces. X-ray photoelectron spectroscopy, together with density functional theory and Monte Carlo modeling, help unravel the differences between the two systems. The molecules form large ordered domains, yet with completely different architectures. Our data reveal that some of the DHI molecules deposited on Ag are in a modified redox state, with their catechol group oxidized into quinone. On Ag(111), the molecules are disposed in long-range lamellar patterns stabilized by metal-organic coordination, while covalent dimer pairs are observed on Au(111). We also show that the oxidation susceptibility is affected by the substrate, with the DHI/Au remaining inert even after being exposed to O_2 gas.

4.1 Introduction

The development of efficient bottom-up approaches for the production of organic nanomaterials goes hand in hand with our progress in supramolecular chemistry, as we improve our understanding of the parameters that drive the self-organization of the small molecular building blocks into complex structures.[1] The investigation of small model systems with limited functionalities is a crucial step,[2] as it allows to gain mechanistic insight on the molecular behaviour and learn how the intermolecular interactions affect the process,[3, 4] getting us closer to gain predictive control over this type of complex molecular assembly.

Molecular imaging done by scanning tunneling microscopy (STM) is often the starting point for the investigation of such systems.[5, 6] The ability to observe individual molecules at the atomic scale, along with the reduced complexity due to the presence of a substrate and the ultra-high vacuum (UHV) environment, makes STM an invaluable tool to explore the molecule-molecule and molecule-surface interactions.[7, 8]

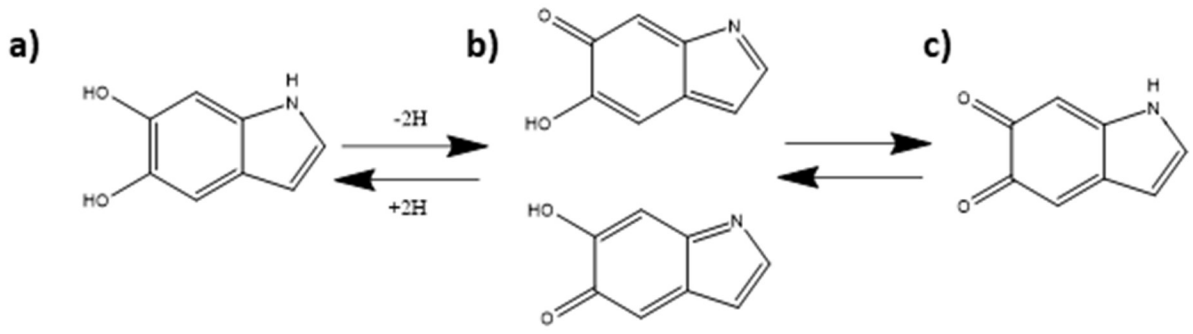

Figure 4.1: a) DHI and its oxidized forms b) indole semiquinone (SQ); c) indolequinone (IQ).

Within this view, we continue our investigation over the self-assembled monolayer networks (SAMNs) of functionalized indoles[9] by presenting our work on 5,6-dihydroxyindole (DHI,[10] Figure 4.1a), in which a pyrrole ring is fused with a catechol. Catechol (o-dihydroxybenzene) and its derivatives have gained increased attention in polymer chemistry in the past few years due to their versatile adhesiveness.[11, 12] In spite of that, the possible exploitation of catechol functional groups for applications in 2D self-assembly has not been investigated in detail, although their chemistry allows several interactions that would help the formation of stable nanostructures. While hydroxyl groups can create SAMNs stabilized by hydrogen bonding,[13-15] catechols can furthermore undergo reversible redox reactions, transforming into semiquinone and quinone forms (Figure 4.1);

partial dehydrogenation can induce a phase transition to more robust architectures,[16-18] by exploiting the interactions between catechol and its oxidized forms.

The catechol-quinone pair reactivity is also behind the self-polymerization reactions of catecholamines,[19] of which the most prominent example is polydopamine.[20] While the reaction mechanism is still under debate, it is believed to involve the redox forms of catechol in a reverse dismutation reaction.[21] These ambiguities are reflected in the polydopamine's final structure, but it is commonly agreed that it consists of a supramolecular aggregate of different oligomers.[21]

DHI is also one of the last monomer intermediate products of the biochemical process that transforms tyrosine into melanin[22] - a promising material for bioelectronics applications.[20, 23, 24] Similar to polydopamine, the polymerization process and final structure of melanin are not yet completely understood,[25] however, it is known that different redox forms of DHI (Figure 4.1b-c) play an important role in the polymerization.[26] The 111 facets of noble metals are chosen as the substrates since the interaction between the surface and the aromatic rings allows the molecule to adsorb in a planar geometry, with the molecules free to diffuse and form self-assembled networks. By comparing the results on the Ag(111) and Au(111) surface we gain insight on how the different surface reactivity affect the 2D growth.[27, 28]

Using STM we determine the structure of DHI SAMNs, while x-ray photoelectron spectroscopy (XPS) gives information on the chemical state of the molecule. Density functional theory (DFT) and Monte Carlo (MC) simulations are then used to corroborate the experimental hypothesis. In this work, we present an investigation of the intermolecular interactions between catechol molecules as well as their reaction with the surface. We demonstrate that, along with intermolecular interactions, additional surface-mediated processes including catechol-quinone redox series of DHI play an essential role in the formation and structure of the SAMNs. On Au(111), our STM and Time-of-Flight Secondary Ion Mass Spectrometry (TOF-SIMS) data show the formation of DHI covalent dimers under ultra-high vacuum conditions at room temperature (RT).

4.2 Experimental

DHI was obtained commercially from Ark-pharm (95+% purity), and also synthesized (95+% purity) following the reaction of L-DOPA in a K3Fe(CN)6 and NaHCO3 solution.[29]

DHI was stored at −20 °C to avoid polymerization. All the experiments were performed under UHV conditions with a base pressure of 10−10 mbar. Both Ag(111) and Au(111) surfaces were cleaned by sequential sputtering (0.8 to 1.2 keV at 10−5 mbar of Ar for 15 minutes) and annealing (480 °C for 30 minutes) prior to deposition. DHI was deposited in a dedicated molecular beam epitaxy (MBE) chamber using an effusion (Knudsen) cell. To obtain monolayer coverage, an evaporator was kept at 60 °C for 15 minutes when dosing on Ag(111). To achieve a similar coverage on Au(111), it was necessary to keep the evaporator at 70 °C and deposit for 30 minutes. Samples were transferred between the preparation and analysis (MBE and STM) chambers through a load-lock transfer arm within the same UHV system. STM images were recorded using a SPECS Aarhus 10 STM. All STM data were collected in constant-current mode. Bias voltages are reported with respect to the STM tip. Similar deposition conditions were applied to prepare the samples in a separate UHV chamber, followed by in situ XPS characterization with a SPHERA II U5 analyser from Scienta Omicron Gmbh, with a Mg source (pass energy 20 eV and 1 second of dwell time).

To trigger oxidation, the same procedure was adopted in both UHV chambers: samples were exposed to O2 gas by dosing through a leak valve in the main chamber, at a pressure of 10−6 mbar for 30 minutes.All image processing and analysis were done using the free WSxM software.30 Image calibrations were performed using the STM images of the clean surface obtained on the same day and based on the known lattice constants of the substrates. More details on the lattice correction are described in the ESI.

TOF-SIMS was carried out using a TOF-SIMS IV (IONTOF Gmbh) with a base pressure of 10^{-10} mbar. A 15 keV Bi^{+} beam was used to sample an area of approximately 50 × 50 μm^2. Both positive and negative SIMS were performed at three different locations of the surface.

DFT calculations were performed with Vienna Ab-initio Simulation Package (VASP)[31, 32] using the Perdew-Burke-Ernzerhof[33] approximation (PBE) of the exchange-correlation potential, the projector augmented wave (PAW) method,[34, 35] and a plane-wave basis set with an energy cut-off of 450 eV. The dispersion forces were included in the calculations using DFT-D3 methods of Grimme.[36, 37] For the simulations of the reported SAMNs, gas phase calculations were performed in which all atoms were relaxed. All the calculations were performed at the gamma point until the net force on each atom was less than 0.02

eV/Å and the energy change between the two steps was smaller than 0.01 meV. The optimized structures are presented using VESTA software.[38]

Dimerization reaction energies were calculated under Gaussian09 software[39] by DFT using B3LYP hybrid functional approximation method with 6-311G(d,P) and 6-31G(d) basis set.

MC simulations[40] were performed on a square lattice of size L × L (L = 96) using Metropolis algorithm and Kawasaki dynamics. During the simulations, the number of molecules was fixed, and periodic boundary conditions were implemented. A randomly selected molecule was allowed to jump into an unoccupied lattice site. Such move was accepted with a probability exp(−ΔE/kT), where ΔE is the energy difference between the final (after the jump) and the initial (before the jump) state of the system. The Boltzmann constant is denoted as k. Up to 107 MC steps per site were performed to ensure a proper equilibration at each temperature. In the calculations, the thermodynamic temperature (T) and interaction energies are normalized by the strongest molecular interaction.

4.3 Results and discussion

4.3.1 DHI on Ag(111)

After depositing DHI on Ag, the molecules assemble into lamellar structures across the surface (Figure 4.2a), which presents multiple orientation domains that extend up to hundreds of nanometres across the surface (Figure 4.10). Multi-domain STM images suggest the existence of six equivalent domains, reflecting the threefold symmetry of the substrate. The lamellae are formed by molecular pairs whose dimensions suggests a non-covalently bonded assembly. The separation between the lamellae decreases as the molecular coverage increases (Figure 4.11), until reaching a close-packed structure with the unit cell dimension of u= 0.65 ± 0.05 nm, v= 1.65 ± 0.05 nm and angle of θ= 110 ± 2°. The contrast and shape of the molecules forming the dimer is not identical (Figure 4.2b). At positive bias an additional bright feature, likely a silver adatom, seems to be accommodated between the two molecules within the lamella (Figure 4.2c), which we tentatively assign as a metal-organic structure.[41, 42]

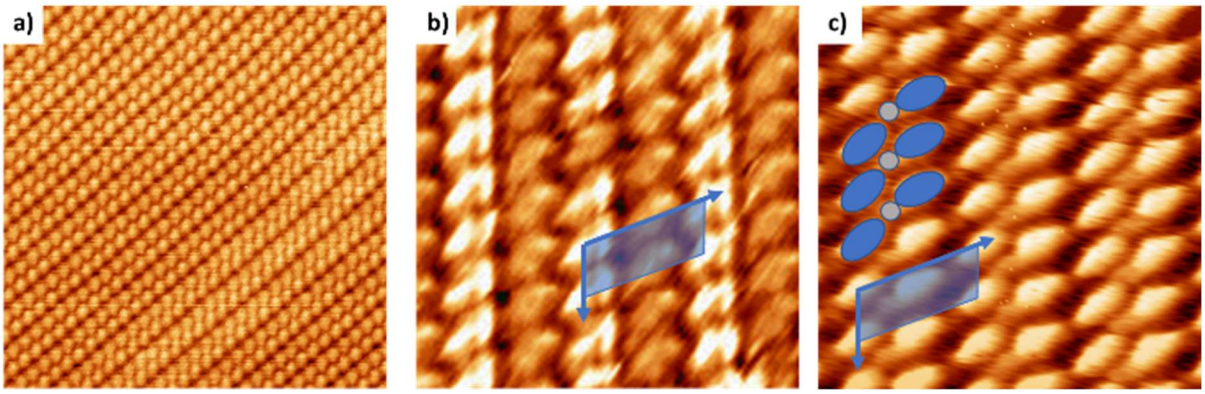

Figure 4.2: STM images of the as-deposited DHI/Ag(111) system; a) 20×20 nm^2 lamellar structures (0.23 nA, 0.51V); 5×5 nm^2 of the lamellar phase taken at b) negative (-1.1 nA, -0.79 V) and c) positive (1 nA, 0.83 V) bias.

Although the STM im ages provide general insight into the molecular conformation on the surface, the specifics of the redox state of the molecule cannot be identified directly from the images. Furthermore, the molecule is prochiral, i.e., once deposited on the surface, two different isomers can be found, increasing the number of possible molecular conformations. The contrast difference of these features may be due to having several conformations of DHI, due to its prochiral geometry, or to different oxidation states as the result of catechol-quinone redox. To properly characterize the lamellar structure, XPS measurement of the DHI molecular networks on Ag(111) was performed, described hereafter (Figure 4.3).

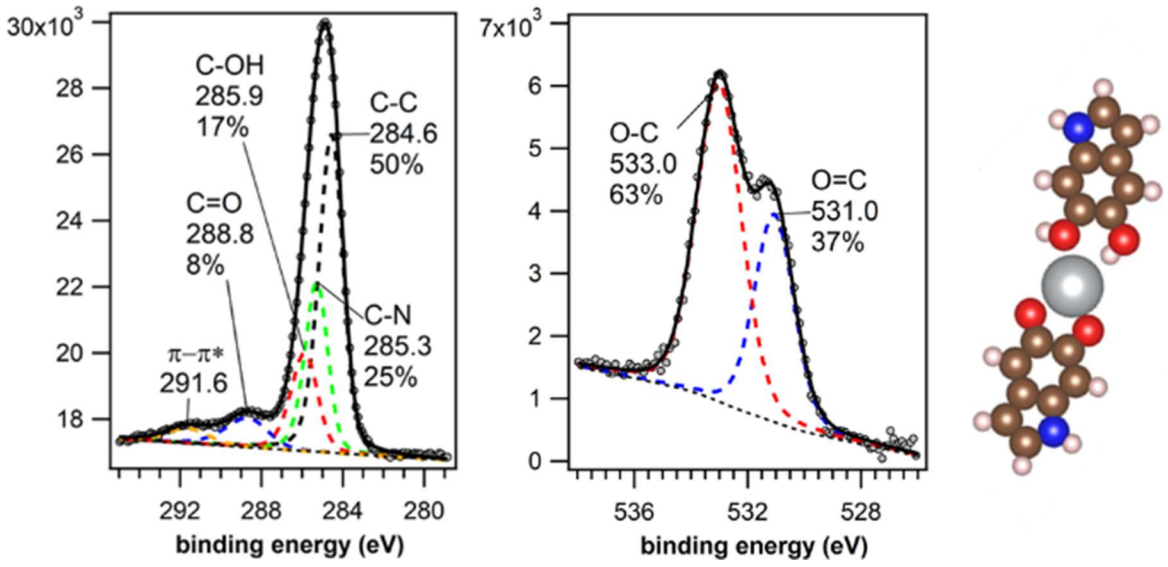

Figure 4.3: XPS spectra of the as-deposited DHI/Ag111 sample a) C 1s; b) O 1s; the components' peak position and overall ratio are reported; DFT model of the catechol-quinone metal-coordination dimer is shown in c).

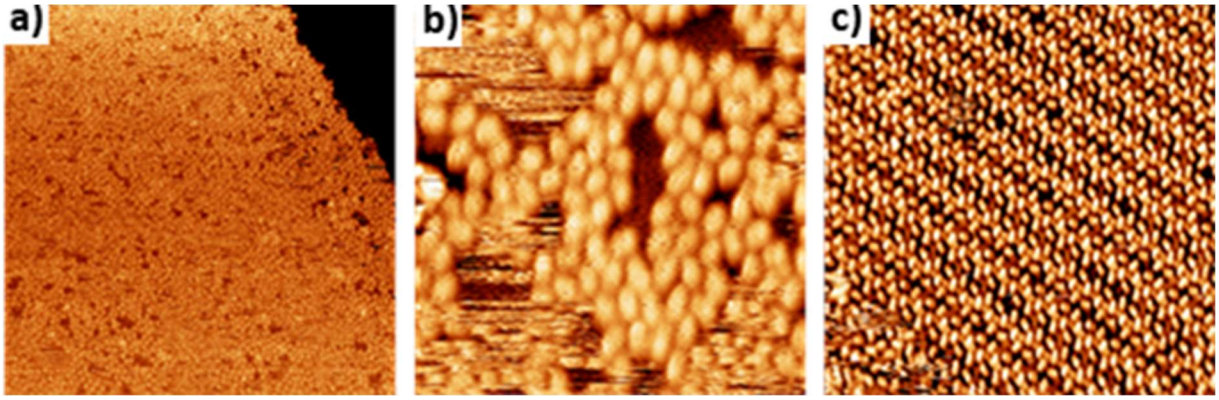

Figure 4.4: STM images of the DHI/Ag(111) after exposure to O_2 a) 45×45 nm^2 and (1.0 nA, 0.81 V) b) 7×7 nm^2 (0.1 nA, 0.32 V) c), 20×20 nm^2 mixed DHI and IQ ordered structure after O_2 exposure (0.1 nA, 0.24 V).

O 1s spectra reveal the presence of both catechol and quinone peaks at binding energies (BE) – whose peak position is in close agreement with values reported in the literature.[43, 44] The main peak at 533.0 eV (Figure 4.3b) is attributed to the hydroxyl group (O-C) of the catechol, while the peak at 2.0 eV lower BE (531.1 eV), is attributed to O=C, suggesting that some of the hydroxyl groups are oxidized to carbonyl. This is consistent with the corresponding C 1s spectra in which a peak at 288.7 eV, assigned to C=O, is identified (Figure 4.3a).[45] Analysis of the N 1s spectral region is challenging due to the proximity to the Ag 3d peak. Nevertheless, our fitting suggests a single peak at 400.0 eV, which can be related to C-N pyrrole[46, 47] (Figure 4.13). According to these data, we infer that DHI adsorbed on Ag(111) is present in two forms: the catechol and its oxidized counterpart as indole-5,6-quinone (IQ, Figure 4.1c). We can determine the proportion of the two redox forms from the 4:7 ratio between the area of the O=C (IQ) and O-C (DHI) components of the O 1s fit in Figure 4.3b.

Based on the STM and XPS result, we simulated by DFT calculations mixed catechol-quinone configurations, shown in Figure 4.3c and 4.15, including the surface in the simulation, in which the proposed metal-organic structure would represent a better geometry due to the interaction with surface atoms. In these models, the lamella is formed by a dimeric unit composed of one DHI and one IQ. A silver adatom is incorporated in the assembly, located between the quinone and the catechol. Based on the starting position of the hydrogen on the hydroxyl groups, the simulations converge towards the formation of a linear dimer (As shown in Figure 4.15a), or a more asymmetrical one (Figure 4.3c and 4.15d), with very similar energy (Δ=0.01 eV). In both of the cases, IQ is located closer to

the substrate to maintain coordination with the Ag adatom, and the silver adatom lies closer to the oxygens of IQ than those of DHI. The DFT models suggest that the quinone strongly interacts with Ag adatoms, and the catechol hydroxyl groups further stabilize the assembly by forming hydrogen bonds between neighbouring O-H, C=O, and N-H groups. While both of the obtained DHI-Ag-IQ structure arrangements match the experimental data in term of dimensions, the asymmetric one better fits the molecular features and contrast of the STM image (as shown in Figure 4.17). While this model reproduces the features of the STM image, it does not match the ratio between DHI and IQ obtained from XPS. However, this disparity may be explained by the fact that XPS averages over a macroscopic area, and all smaller phases and defects ((i.e. the pure DHI lamellae shown in Figure 4.12) contribute to the quantification, affecting the ratio between the two redox species.

Annealing the surface did not produce any further oxidization nor the formation of a different self-assembly. The SAMNs are stable up to 250 °C, after which the molecules start to desorb from the surface. This result is in contrast with other reports in the literature,[17] where molecular moieties with hydroxyl groups show dehydrogenation already upon gentle annealing (< 100 °C).

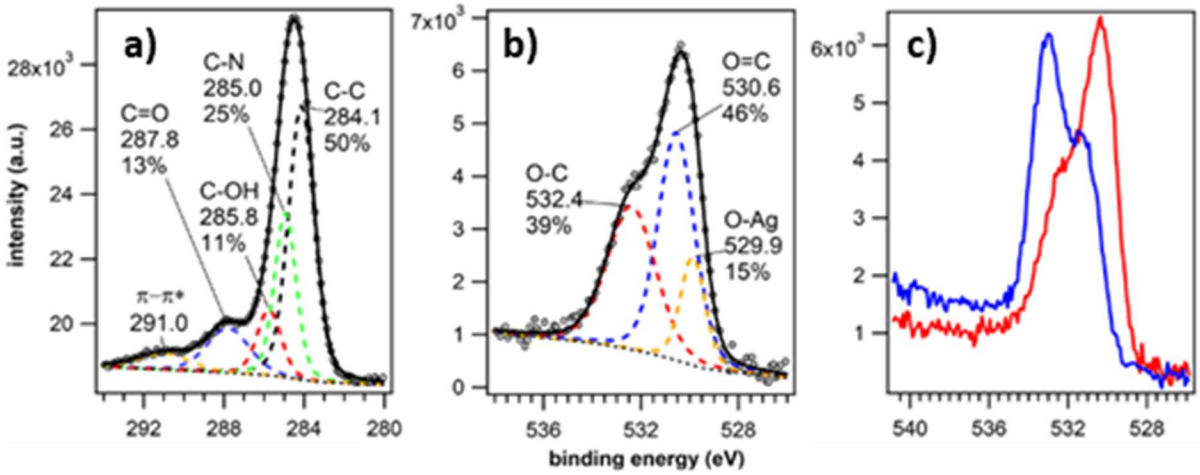

Figure 4.5: High resolution XPS spectra for the a) C 1s and b) O 1s components of DHI/Ag(111) exposed to O2 for 30 minutes. In addition, c) the comparison of the O 1s spectra before (blue) and after (red) O2 exposure; the components' peak position and overall ratio are reported.

Given our motivation to assess the catechol's reactivity on the surface, we attempted to trigger oxidation by exposing the 2D SAMNs on Ag(111) to oxygen.

Following oxygen exposure, our XPS spectra exhibit an obvious change in the O 1s peak (Figure 4.5c). An increase of the O=C peak at the expense of O-C was observed (Figure

4.5b). The FWHM of the O-C peak also strongly increased, which may be due to the multiple hydrogen bonding conformation adopted by the hydroxyl group.[48, 49] In addition, a third peak appears at 529.9 eV, which is related to the formation of silver oxide on the surface. When exposed to O_2, the bare surface of Ag forms only a small amount of AgO even after long exposure times. This is probably due to kinks and defects on the surface that are more prone to oxidation. On the other hand, once the molecule is on the surface, the quantity of formed Ag-O is much higher.

The transformation of catechol into quinone can also be deduced from the C 1s spectra (Figure 4.5a and 4.14), where, in line with the O 1s data, there is an increase in the peak area assigned to C=O. The spectrum undergoes an overall shift of 0.2 eV towards lower BE, possibly due to the change in the work function of the Ag surface related to its partial oxidation as well as to the molecular rearrangement after the lamella disruption,[49, 50] and also shows an intensity loss due to molecular desorption.

From the morphological point of view, we see that the exposure to oxygen destroys the lamellar self-assembly, with the majority of the molecules assembled into disordered clusters, as shown in Figure 4.4a and b. There is a lack of long-range ordering and it is often possible to see small dots close to multiple molecules, suggesting that Ag adatoms are still incorporated in a metal-organic structure.

Small patches of ordered molecules with less than 50 nm^2 size were occasionally found on the surface, as shown Figure 4.4c, in which chains of alternating brighter molecules are disposed around a darker molecular moiety. This variation in STM contrast may be due to a different oxidation state of DHI, similar to what was shown in Figure 4.2b, or to a different disposition of the molecule with respect to its neighbours. The unit cell of this structure contains 14 molecules, and neither annealing nor further O_2 exposure led to larger ordered domains; for higher exposure (i.e. higher concentration of IQ) no ordered phase was either witnessed. This is consistent with the work of Giovanelli et al.[16] where, after partial dehydrogenation, larger catechol containing molecules were able to reassemble in different ordered structures. Similar to the present report, further dehydrogenation did not improve the ordering, suggesting that a minimum catechol to quinone ratio was necessary for the stability of the structure.

We investigated the proposed ordered structures using MC simulations. Such calculations take entropic effects into account and help to identify the most important molecular

interactions that are responsible for ordering.[51, 52] We obtained the experimental molecular arrangement using three interactions depicted in Figure 4.6. The main interaction is the catechol-quinone dimer (see the model shown in Figure 4.3c) characterized by energy e_d. We believe that this is the strongest interaction as the STM images mostly show chains of dimers and not of single molecules. The dimers are coupled together into chains with two side interactions es_1 and es_2 (Figure 4.6). We expect es_1 and es_2 to be significantly weaker than e_d. Interaction energies are kept as variable model parameters and normalized by the strongest catechol-quinone dimer interaction.

The snapshots of the MC simulations are presented in Figure 4.6 for different values of side interaction energies. The experimentally observed lamellar structure is obtained for a rather wide range of interaction parameters ($es_1 < es_2 < e_d$). Compared with other similar models,[53] a reasonable set of parameters is $e_d = 1.0$, $es_1 = 0.2$ and $es_2 = 0.4$ (see Figure 4.6e). Note that condition $es_1 < es_2$ is necessary to obtain the experimental phase. Otherwise, a less dense, higher symmetry structure, which is not observed in the experiment, is formed (Figure 4.18). More details about the model and MC simulations are given in the supplementary material.

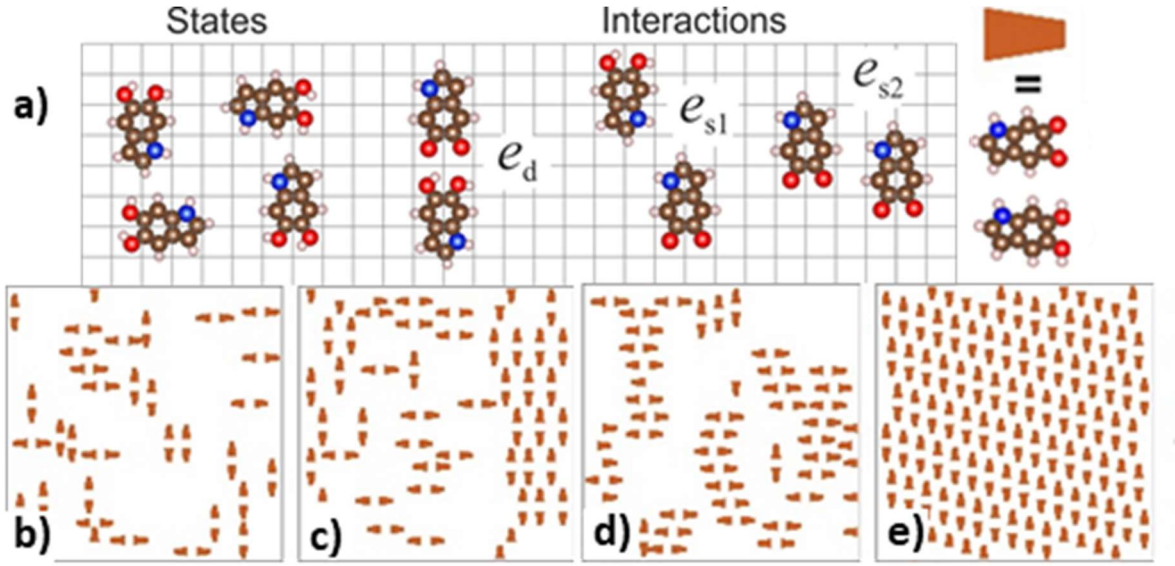

Figure 4.6: a) Four molecular states of DHI molecule and intermolecular interactions used for MC simulations. Snapshots of MC simulations obtained for b) es1 = es2 = 0, c) es1 = 0.2, es2 = 0, d) es1 = 0, es2 = 0.4 and e) es1 = 0.2, es2 = 0.4. Other simulation parameters: ed = 1, T = 0.1. Experimentally observed lamellar structure is presented in d).

4.3.2 DHI on Au(111)

When deposited on Au, DHI molecules self-assemble in a structure different from the one observed on Ag(111). The unit cell is rectangular with the dimensions of u= 1.40 ± 0.1 nm, v= 1.53 ± 0.1 nm and θ= 90 ± 3° (Figure 4.7).

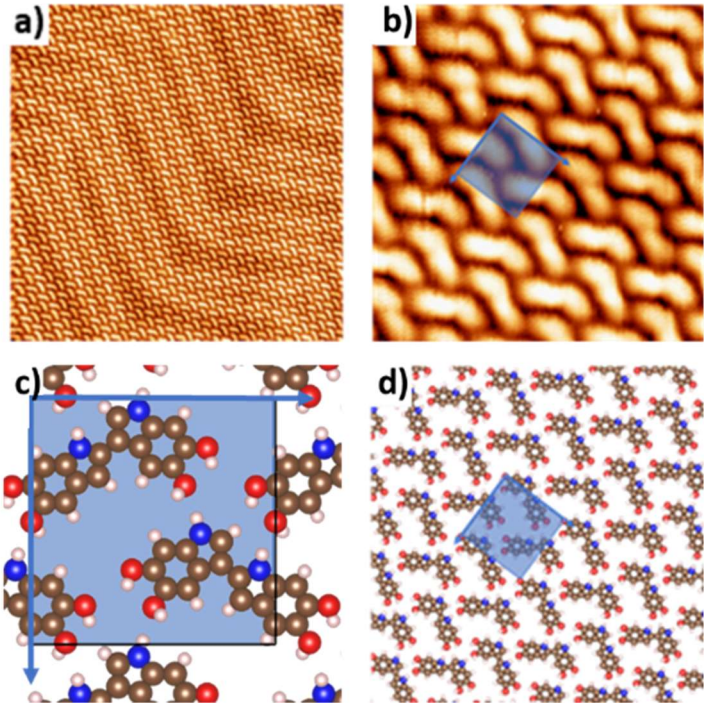

Figure 4.7: STM detail of the DHI/Au(111) a) 25×25 nm^2 (-0.1 nA, -0.83 V) b) 7×7 nm^2 (-1 nA, 0.14 V) c) and d) are simulated model for the banana-shape phase over the STM image of the DHI/Au(111) system.

Each cell contains a pair of banana-shape molecular dimers in a close-packed arrangement, disposed perpendicular to each other. The short length of these features (less than 1.3 nm) is not consistent with non-covalent assembly, thus we propose a covalent dimeric structure. The XPS analysis of the DHI/Au(111) samples shows that the molecule is pure catechol. Although the O 1s peak is very close to the Au 4p peak, it is still evident by comparison with the spectrum of DHI/Ag(111) that only one component is present for DHI on Au(111). As additional confirmation, the C 1s (Figure 4.8a) does not show any peak related to a C=O component. The position of the C-C component is close to the one obtained for Ag, therefore discounts the presence of a C-Au organometallic bond, whose presence would be indicated by a component at a lower BE.[54] Again, the N 1s peak position is close to the pyrrole one at 400.0 eV. The lack of an additional peaks at

399.0 eV related to the aromatic C=N-C bond excludes the presence of the semiquinone form.[55]

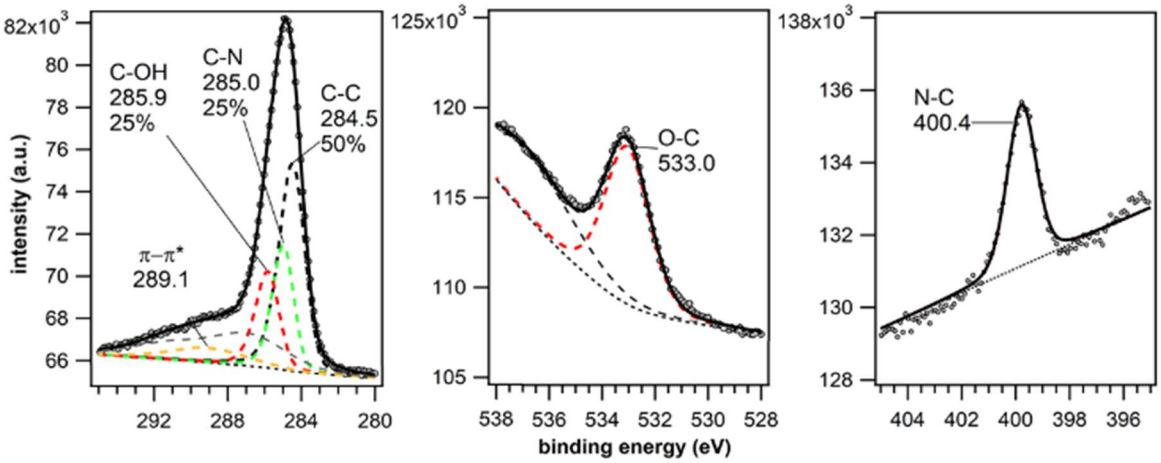

Figure 4.8: High resolution XPS spectra of the DHI/Au(111) a) C 1s, b) O 1s and c) N 1s; the components' peak position and overall ratio are reported. The XPS spectra of the Au sample before deposition is reported with a dashed grey line and has been taken in account during the fitting.

Similar to Ag, annealing does not affect molecular self-assembly on Au; however, unlike the Ag case, the molecular structures on Au remain unchanged following oxygen dosing, even after being exposed to atmospheric conditions.

Based on these experimental results, we hypothesize that the DHI/Au(111) system is composed of DHI-DHI covalently bonded dimers. While it is not unusual for molecules to polymerize on the Au surface, an annealing step is often required to trigger the polymerization.[56-58] To confirm that the structure observed by STM are DHI dimers, TOF-SIMS analysis of the sample was conducted (Figure 4.9). It is evident from the spectra that both the monomer and the dimer are present on the surface. TOF-SIMS also confirms different susceptibility to oxidation of the structures formed on the two studied substrates. On Au(111), no peak associated to IQ can be seen, thus confirming that the DHI/Au(111) remained stable during the transfer between the two UHV systems, without any oxidation process. An opposite result is obtained for Ag(111), where no dimer is visible, and the IQ peak is stronger than its reduced counterpart (Figure 4.19).

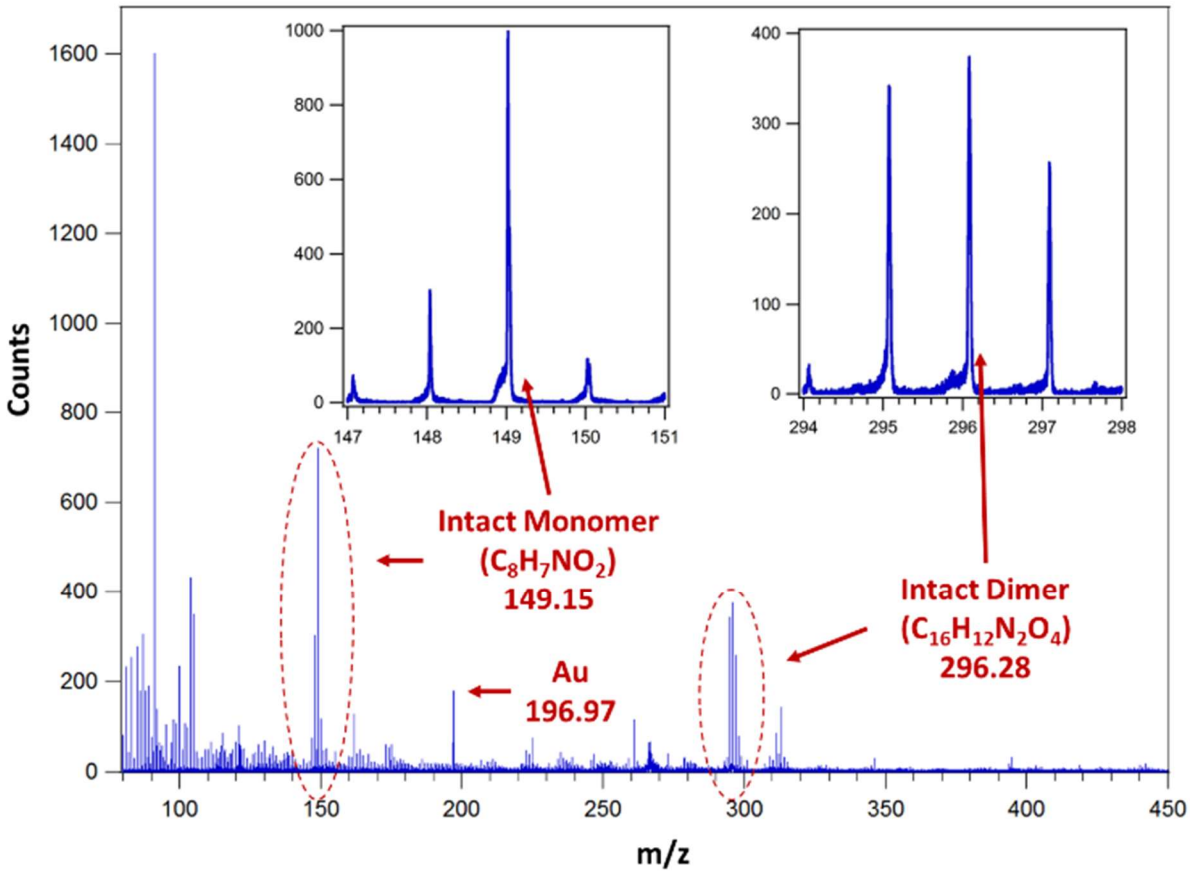

Figure 4.9: TOF-SIMS of the DHI/Au sample. The insets zoom over the area related to DHI monomer and dimers.

Although TOF-SIMS demonstrates the presence of dimerized DHI, the dimer geometry is not self-evident from STM. Different bonding conformations may lead to a planar dimer and a diversity of configurations had to be taken in account due to the prochirality of the molecule. These factors create the possibility for several regioisomers (presented in Figure 4.23). However, only one of the dimers, shown in Figure 4.23c, matches the dimensions and shape of the STM features, as it can be seen in Figure 4.7d. These results show that the reaction of DHI on the (111) surfaces is strongly affected by the nature of the substrate itself. While on Ag the molecules react to form metal-organic structures, on Au they are instead able to bond with each other and form covalently bonded dimers.

The proposed covalent dimerization reaction on the surface has not been previously reported for 2D on-surface molecular study. Although DHI is well-known for its ability to polymerize under suitable conditions,[10, 25, 59] this is the first report presenting the polymerization of indole moieties, carried out under UHV at RT. On the other hand, while

DHI oxidative polymerization usually leads to a range of products with different chain length and bonding motifs,[60] the presence of a surface constrains the process, producing only dimers that exhibit a bond at their 2-3 positions. The peculiar conformation of the dimers on the surface suggests that the dimerization is triggered by the indole ring reactivity. In an acidic environment, indole molecules may undergo a polymerization reaction that leads to their trimerization,[61] whose intermediate products are similar to the dimers shown in Figure 4.7c. On the other hand, since our STM and XPS analysis can only retrieve information on the already formed products, we have to account for the fact that different redox forms of DHI may be present during the dimerization process. This would allow for multiple possible reaction pathways and mechanisms (radical, ionic or even a combination of the two), such as SQ radical coupling[62] and DHI/IQ nucleophilic attack.[63] While being unable to discern between these different possibilities, we retrieved the reaction energy in the gas phase and we find that the dimerization is energetically more favourable for SQ > IQ > DHI. The dimerization of the catechol form, in particular, is not thermodynamically favoured in the gas phase. In addition, our data shows that the same polymerization reaction does not occur on Ag(111). In contrast to the Au surface, the molecular structures imaged by STM do not indicate any dimer or polymer formation on Ag. The main difference between the two systems is in the redox state of the molecule. DHI is already partially oxidized into its IQ counterpart upon deposition on silver, and is further converted to IQ when exposed to O_2 gas. While a catechol group is not necessary to obtain the aforementioned acid polymerization,[64, 65] the oxidation in IQ enables new interactions that hinder the continuation of the polymerization process. As we have seen in our DFT data, IQ instead strongly interacts with the surface, bonding with adatoms and incorporating them into a self-assembled metal-organic network. This limits the diffusion of the molecule across the surface and prevents further reaction.

From the point of view of supramolecular chemistry, we have also seen that the presence of non-oxidized DHI molecules contributes to the formation of wide ordered domains, while after their conversion to IQ the molecules are arranged in disordered clusters. This inability to form long-range order may be due to the reduced diffusion of IQ molecules on the surface, hampered by metal-organic coordination, as well as the presence of silver oxide on the surface. It was previously reported for catechol-containing molecules deposited on Ag[16-18] that similar dehydrogenation reactions can be thermally induced and used to create strong interactions between catechols and quinone. However, in our study, thermal

annealing did not lead to dehydrogenation: no visible change in the structure was obtained until the desorption temperature was reached (200°C). This is probably due to the lower adsorption energy of smaller molecules such as DHI, where the temperature of the dehydrogenation/oxidation process is higher than the desorption one. In contrast with what was previously reported, our data suggest that Ag adatoms might be incorporated in the networks, while the other studies have disregarded this possibility.[16, 17]

The possibility of achieving the same oxidation of the molecule on surface both thermally and by exposure to O_2 gas is promising, as it may open new reaction pathways for systems that do not tolerate thermal annealing. As we have seen in Figure 4.4c, variations in the IQ/DHI ratio may drive the system towards the formation of a different self-assembled architecture. With a judicious choice of molecule and surface, this on-surface oxidation may be triggered and better controlled, as well as used as a tool for engineering of the chemistry and topology of biologically-relevant molecular layers at surfaces.

4.4 Conclusions

We have reported our investigation of the self-assembly of DHI over the (111) surfaces of Ag and Au. When deposited on Ag(111), the molecule partially oxidizes upon adsorption, forming long-range ordered metal-organic structures composed of a mixture of catechols and quinones. Further exposure to oxygen leads to additional conversion of the catechol species into quinone. Oxygen exposure causes an increase in IQ and can trigger a phase transition of the SAMNs, however a full layer of IQ does not create structures with long-range order.

On Au(111), DHI bonds into covalent dimers, and does not undergo further oxidation, even if exposed to O_2. The exposure does not lead to any morphological or chemical change in the molecule. The size of the imaged features in STM does not match with single molecule but suggests a covalent dimer structures which is consistent with species present in TOF-SIMS measurements of the surface. The dimer shape and dimension suggest that a mechanism similar to indole polymerization in acid solution is involved. However, unlike the solution case, a cyclic trimer was not obtained.

Our study demonstrates that the UHV STM is a convenient approach for the investigation of the multiple chemical reactions that lead to the catecholamine polymerization. The reduced complexity environment helps us better understand how the molecule-surface

interactions strongly affect the catechol group, driving the formation of different 2D structures with different chemical bondings. By investigating other eumelanin precursors, we may be able to gain important insight on the pigment complex structure, as well as understand the differences with other synthetic eumelanin-like polymers preparation routes.

Furthermore, our study revealed an interesting coupling reaction that leads to the DHI dimerization o Au. This may be exploited for the preparation of 2D conjugated polymers, but further investigation is required, to better clarify the mechanism of the reaction and the role of the catechol group in the process.

4.5 Supporting Information

4.5.1 DHI/Ag(111) – STM

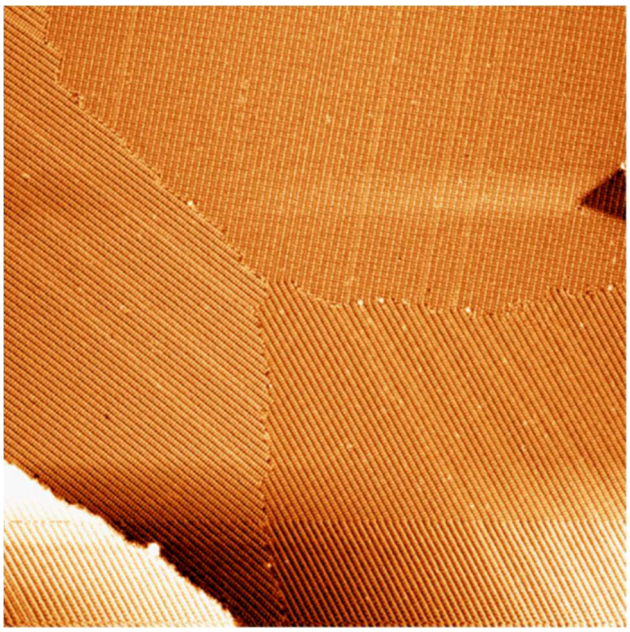

Figure 4.10: Large scale image of the DHI /Ag111 lamellar phase (0.23 nA, 0.51 V, 170x170 nm^2)

After deposition on Ag(111), DHI forms extended domains, with dimensions up to hundreds of nanometers, (Figure 4.10). For lower coverage, DHI still organizes in lamellae, with increased spacing (Figure 4.11b). At very low coverage, it is possible to find single lamellae on the surface, but their imaging is difficult due to molecular diffusion (figure 4.12a).

Even for full monolayers, it is often possible to observe some lamella with different contrast or orientation within the domains (Figure 4.10 and 4.12). These variations are probably due to the presence of a pure DHI lamella, with the dimensions and geometry that are different from the IQ/DHI lamella.

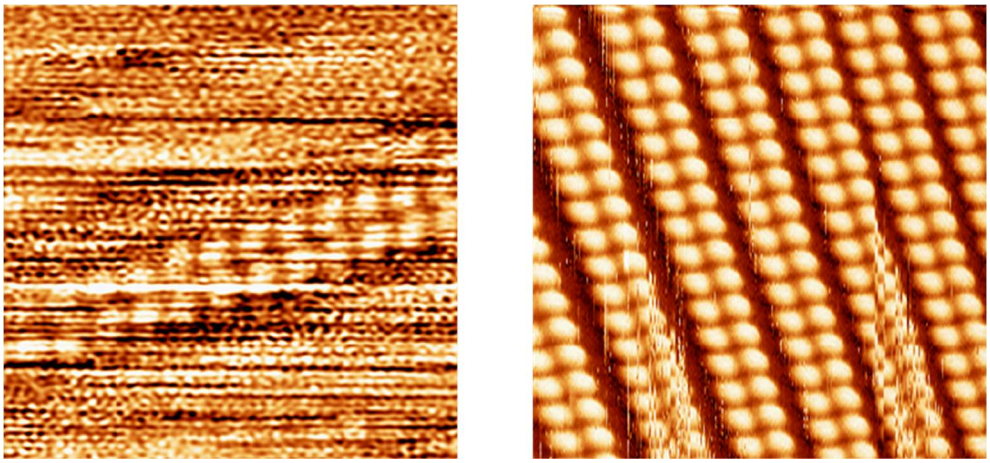

Figure 4.11: Different lamellar phases of DHI/Ag111, obtained at coverages lower than 1 ML. a) (0.1 nA, -0.5 V, 8x8 nm2) b) (0.11 nA, -0.52 V, 12x12 nm^2)

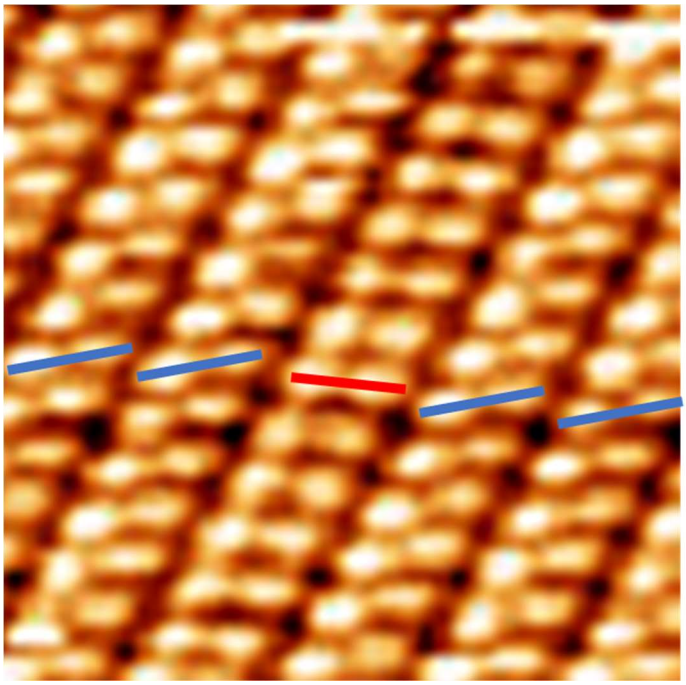

Figure 4.12: Pure DHI lamella (in red) surrounded by DHI/IQ lamellae (0.2 nA, -0.51 V, 10x10 nm^2). The dimers are overlaid with short lines, to underline the different orientation of the lamella with respect to their neighbors.

4.5.2 DHI/Ag(111) – XPS

For the purpose of peak fitting, the value of each FWHM was not fixed but it was left free to vary within a reasonable range (Table 4.2) to reflect the different bonding environments due to the chemical/structural diversity of the system. After the exposure to O_2, the difference in peak widths strongly increases (2.35 eV vs 1.77 eV) and reflects the disorder of the sample: the FWHM of the O-C component gets larger to reflect the multiple bonding pattern that the molecule adopts across the surface.

Table 4.1: Peak position for the fitted XPS spectras in figures 4.3, 4.5 and 4.8.

		Ag(111)		Au(111)
		As deposited	After O2	As deposited
O1s	C-OH	533.0	532.8	533.0
	C=O	531.0	531.2	-
	O-Ag	-	530.1	-
C1s	C-C	284.6	284.1	284.5
	C-N	285.3	255.0	285.0
	C-OH	285.9	285.8	285.9
	C=O	288.7	287.8	-

Table 4.2: FWHM of the fitted peak in figures 4.3, 4.5 and 4.8.

		Ag(111)		Au(111)
		As deposited	After O2	As deposited
O1s	C-OH	1.94	2.00	2.0
	C=O	1.66	2.00	-
	O-Ag	-	1.49	-
C1s	C-C	1.40	1.53	1.67
	C-N	1.35	1.27	1.38
	C-OH	1.61	1.42	1.53
	C=O	2.50	2.50	-

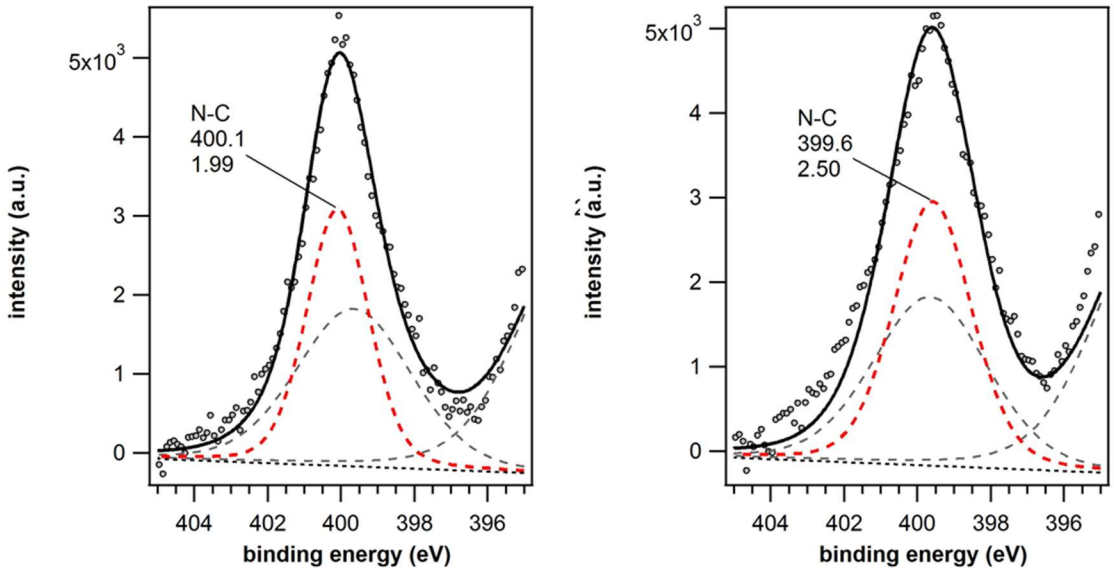

Figure 4.13: XPS spectra of DHI/Ag(111) before and after exposure to O_2. The displayed grey component accounts for the spectral weight contributed by the clean substrate.

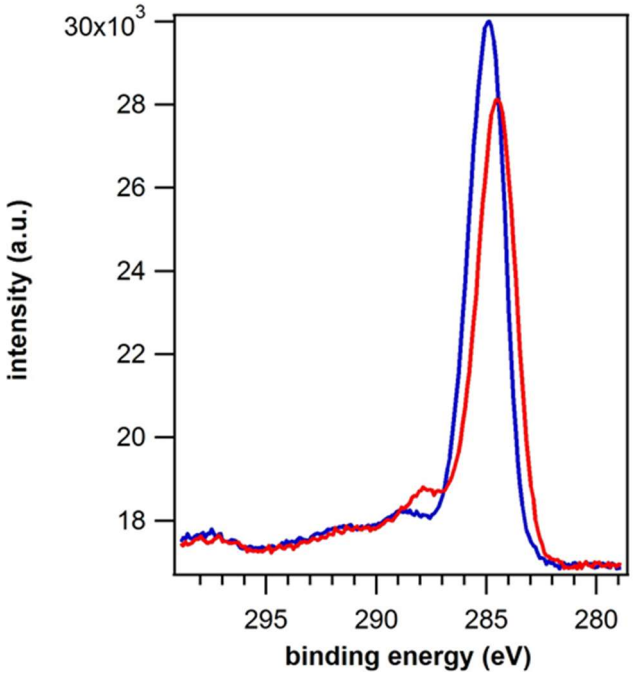

Figure 4.14: Comparison of the C 1s spectra of the DHICA/Ag111 before (blue) and after (red) O2 exposure

4.5.3 DHI/Ag(111) – DFT model for DHI-Ag-IQ

We have simulated different possible configurations of the metal-organic DHI dimer. Since we have not been able to identify the commensurate unit cell associated with the observed metal-organic molecular structure, a simulation of a proper model, with a supercell containing both the metal-organic structures and the surface representing the experimental data, was not feasible due to the limitation imposed by PBC. In spite of that, to explore a more advanced model, we included the surface in the simulation, in which the proposed metal-organic structure would represent a better geometry due to the interaction with surface atoms.

Based on the starting position of the hydrogen on the hydroxyl groups, the simulation converges towards the formation of a linear dimer (as shown in Figure 4.15a), or a more asymmetrical one (Figure 4.15d). In both of the cases, IQ is located at a closer distance to the substrate to maintain a coordination with the Ag adatom (Figure 4.15c & f), and the silver adatom lies closer to the IQ oxygens respect to the DHI ones.

The linear dimer displays an angle ϑ between the carbons in position 2 and the silver (C2-Ag-C2') to be equal to 176.7° (vs the experimental value of 172 ±5°), and the silver adatom lies almost perfectly in between the IQ oxygens (O•••Ag=2.34 Å & 2.37 Å) and the DHI ones (HO•••Ag= 2.63 A & 2.81 Å).

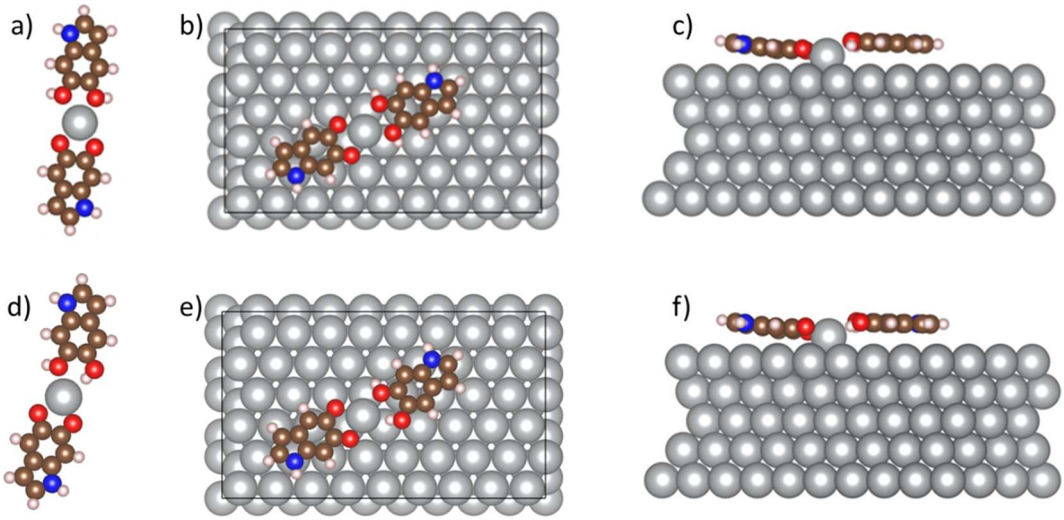

Figure 4.15: Top-view and side-view for DFT simulation of one metal-organic DHI-Ag-IQ dimer on a 5-layer Ag(111) slab of 270 silver atoms.

In the asymmetric configuration instead, one of hydrogen lies in between the silver adatom and the hydroxyl oxygen, leading to a dimer with an angle ϑ equal to 170.5°. The silver adatom coordinates with only one of the catechol oxygens (HO•••Ag= 2.64 A & 3.38 Å) and also a minor asymmetry is present in the Ag position respect to the quinone oxygens (O•••Ag=2.36 Å & 2.29 Å).The two models have very similar energy, with the asymmetrical one being more stable by ΔE=0.01 eV which is well below the kT value at room temperature. The simulations were repeated with a two dimer pairs (Figure 4.16), and this time the energy difference between the two increased to Δ=0.1 eV.

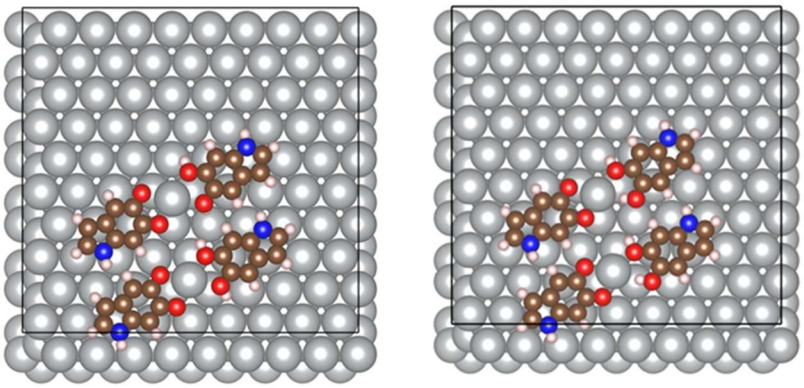

Figure 4.16: DFT simulation of two DHI-Ag-IQ dimers in the a) linear and b) asymmetrical configurations.

We have superimposed both the obtained metal-organic dimer with the STM image, and while both of the proposed DHI-Ag-IQ structure arrangements match the experimental data dimension, the asymmetric one better fits the contrast of the image (as shown below in Figure 4.17).

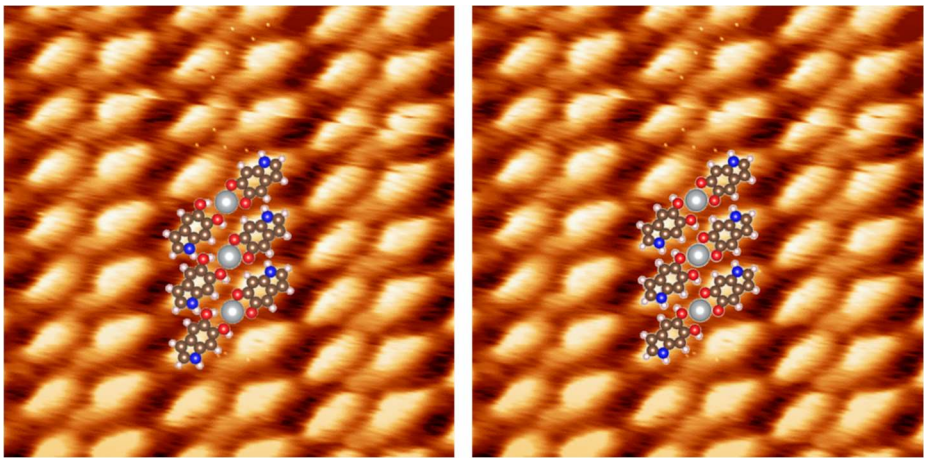

Figure 4.17: a) Overlay of the simulated DHI-Ag-IQ dimer over the STM image. b) detail of the DHI-Ag-IQ metal-organic dimer.

4.5.4 DHI/Ag(111) – MC model

In the MC model, the center of the DHI molecule (and its rotation axis) is assumed to occupy one site of a square lattice as shown in Figure 4.6. The molecule is assumed to have four molecular states which differ in 90 ° rotation of a molecule (Figure 4.6, left). The fifth state is a vacancy state (no molecule on a site). The molecule is free to move over the sites of the lattice and rotate to one of the four mentioned states. There are three intermolecular interactions that drive the ordering in the model (Figure 4.6a).

We note that for simplicity, the Ag adatoms in our model act as interaction mediators and are not explicitly considered. We also ignored the chiral nature of the DHI molecules, as nitrogen atom barely affects the side interactions (DFT calculations for gas-phase using B3LYP D3 6-31G(d,p) reveals a difference of 0.11 kcal/mol between the different configurations). Additionally, the side interactions are the same for the catechol and quinone molecules.

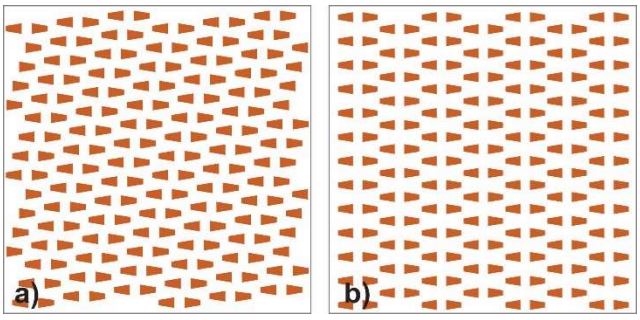

Figure 4.18: Snapshots of MC simulations obtained for a) $e_{s1} < e_{s2}$ (experimental structure) and b) $e_{s1} > e_{s2}$. Other simulation parameters: $e_d = 1$, T = 0.1.

4.5.5 DHI/Ag(111) – TOF-SIMS

Reported in Figure 4.19 is the result of the TOF-SIMS measurements on the DHI/Ag(111) sample. As it is evident from Figure 4.199b, no peak is visible for mass close to DHI dimer. On the other hand, several peaks are present at mass 149.15 and lower. These peaks are related to DHI and IQ, and to their deprotonated counterparts.

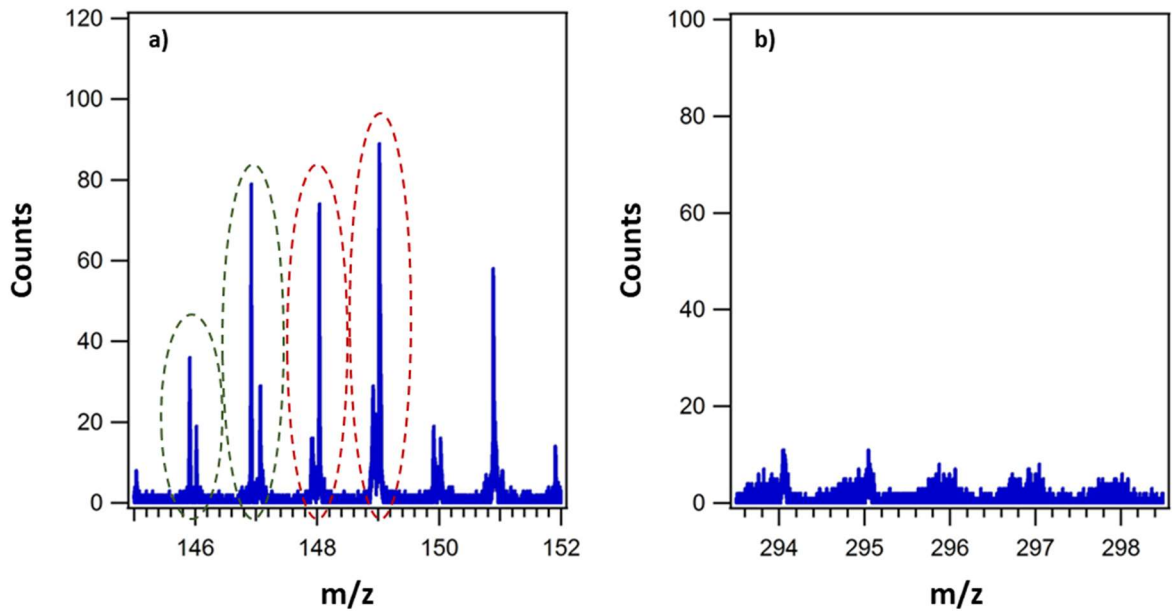

Figure 4.19: Detail of the TOF-SIMS analysis of the DHI/Ag sample. a) shows the region around the monomer mass, where the peaks associated with DHI (in red-dash) and IQ (in green-dash) are highlighted. b) No peak associated with dimer species is detected.

4.5.6 DHI/Au(111) – STM

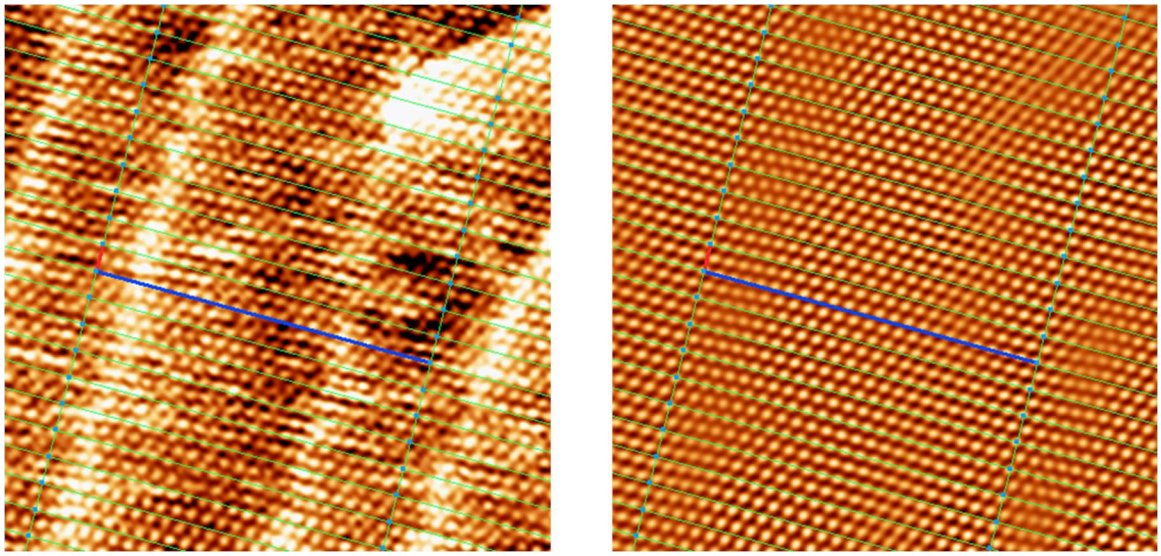

Figure 4.20: an example of the calibration adopted for the DHI/Au(111) phase, where the clean Au substrate image. (3.30 nA, 0.01 V, 10x10 nm^2) has been processed and filtered until the single atoms are properly visible. The image has been calibrated by using the 6.23 nm herring bone reconstruction dimension (1-10, blue vector in the image) at 90° respect to the direction of the solitons (112, red vector in the image) as the distance between 23 atoms.

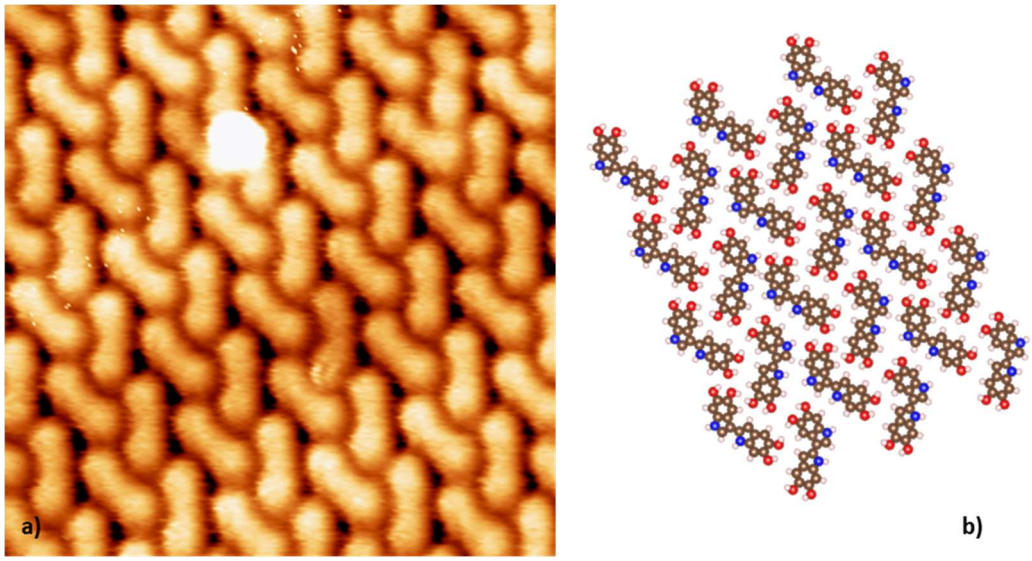

Figure 4.21: The banana shaped dimers occasionally adopted a different conformation, with identical lattice dimensions, but with one of the dimer in its mirror geometry respect to the common case, as depicted in the a) STM image (1.20 nA, 0.20 V, 8x8 nm^2). b) A proposed molecular structure for this phase.

4.5.7 DHI/Au(111) – XPS

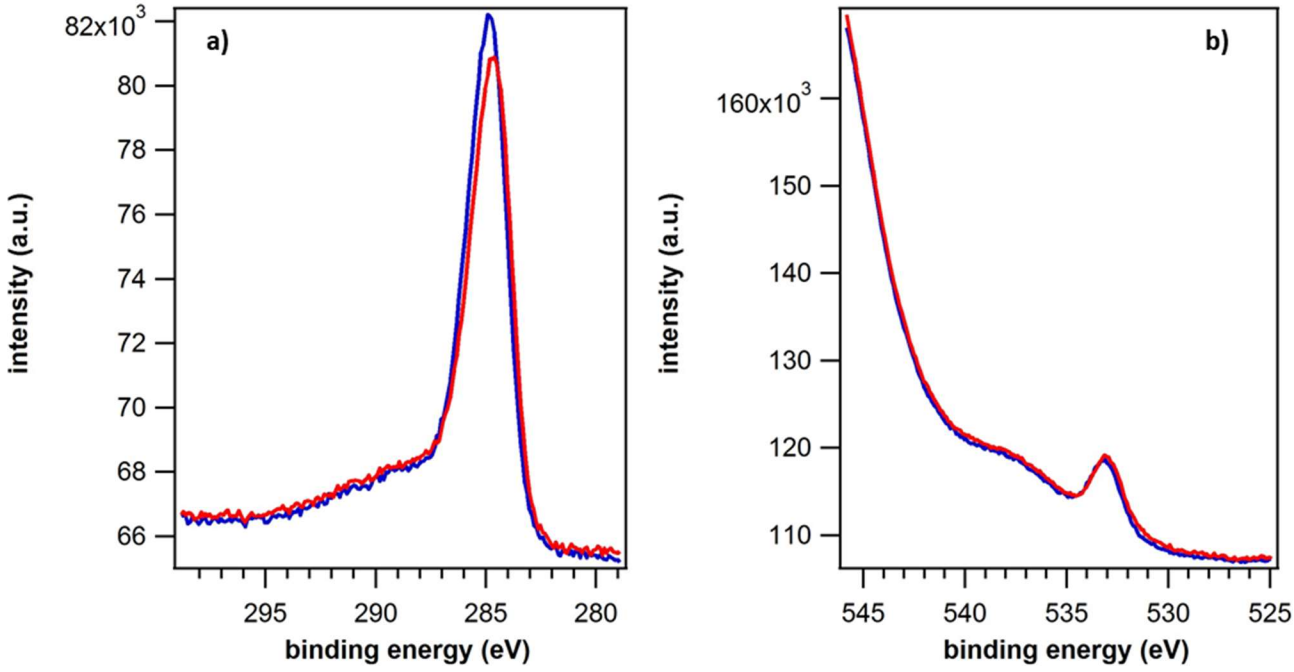

Figure 4.22: Comparison of the a) C 1s spectra and b) O1s before (blue) and after (red) O_2 exposure

4.5.8 DHI/Au(111) – DFT simulated structures for DHI dimer (banana-shape)

	Dimer length (Å)	ΔE (eV)
a	12.97	0.00
b	13.25	0.11
c	12.59	0.11
d	12.51	0.20
e	10.24	0.11
f	10.23	0.05
g	10.34	0.15

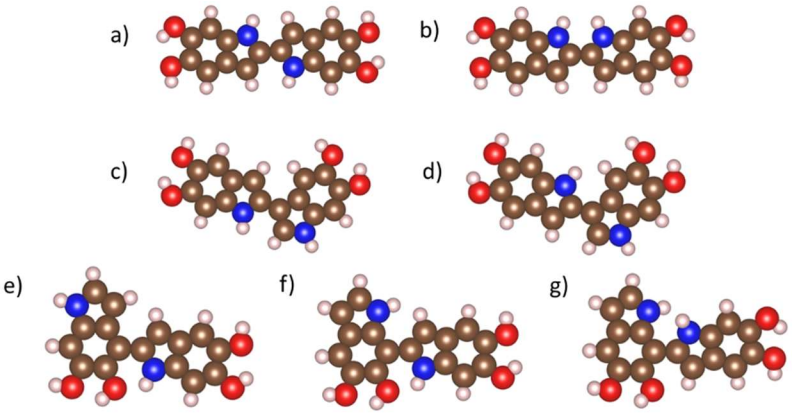

Figure 4.23: Possible regioisomers for a planar DHI dimer. The table reports the length of the dimer in A, calculated as the distance between the two farthest atoms, and the energetic difference respect to the dimer (a). The dimers a-b (linear-shape) do not fit the banana-shape. Both dimers c-d (banana-shape) similarly fit the imaged features, while dimers e-g (T-shape) do not match the experimental data. The difference of the free energy of each structure (DFT calculation by the described method in the MS) with respect to the most energetically stable dimer structure (a)is reported, all of which are within the available energy at room-temperature. The dimer structure (c) which best fits the STM imaged features was further simulated in the slab-model (Figure 4.7).

Table 4.3: Calculated energies for DHI monomer, dimer, H_2 molecules and the dimerization reactions

	B3LYP/ basis set:			
	6-311G(d,P)		*6-31G(d)*	
Molecule	**eV**	**kcal/mol**	**eV**	**kcal/mol**
DHI monomer	-13997.66	-321946.22	-13993.69	-321854.87
SQ monomer	-13963.19	-321153.29	-13959.56	-321069.86
IQ monomer	-13963.57	-321162.18	-13959.98	-320849.43
DHI dimer	-27962.86	-643145.72	-27955.14	-642968.17
H_2	-32.10	-738.30	-31.99	-735.70
ΔE = (dimer + H_2) - (2×DHI)	**0.37**	**8.42**	**0.26**	**5.87**
ΔE = (dimer) - (H_2 + 2×SQ)	**-4.38**	**-100.84**	**-4.03**	**-92.76**
ΔE = (dimer) - (H_2 + 2×IQ)	**-3.61**	**-83.07**	**-3.20**	**-73.62**

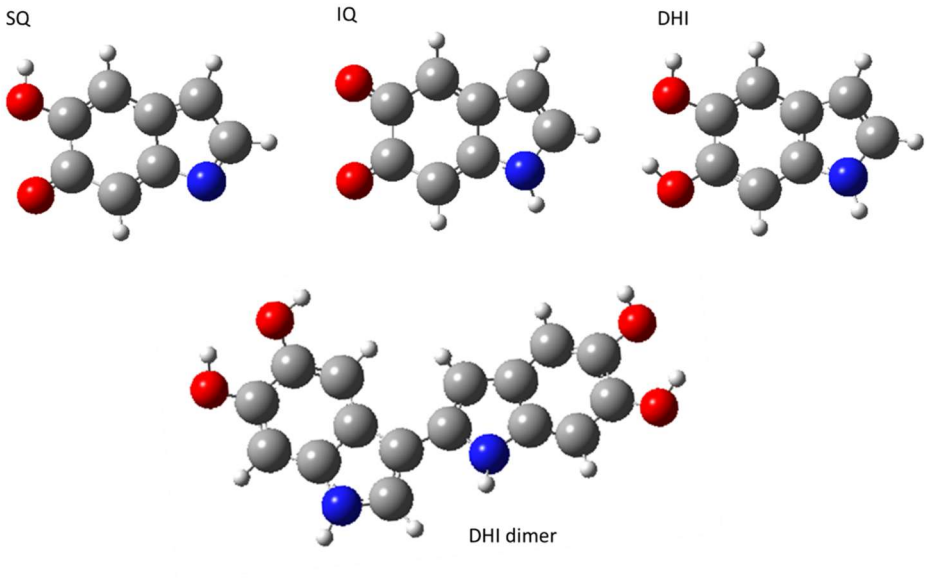

Figure 4.24: Simulated DFT structures: DHI dimer, DHI and its redox forms, IQ and SQ

4.6 Chapter bibliography

1. G. M. Whitesides and M. Boncheva, *Proc. Natl. Acad. Sci.*, 2002, **99**, 4769-4774.
2. C. Heininger, L. Kampschulte, W. A. Heckl and M. Lackinger, *Langmuir*, 2009, **25**, 968-972.
3. J.-M. Lehn, *Proc. Natl. Acad. Sci.*, 2002, **99**, 4763-4768.
4. F. Rosei, M. Schunack, Y. Naitoh, P. Jiang, A. Gourdon, E. Laegsgaard, I. Stensgaard, C. Joachim and F. Besenbacher, *Prog. Surf. Sci*, 2003, **71**, 95-146.
5. J. V. Barth, *Annu. Rev. Phys. Chem*, 2007, **58**, 375-407.
6. J. K. Gimzewski and C. Joachim, *Science*, 1999, **283**, 1683-1688.
7. R. Otero, J. M. Gallego, A. L. V. de Parga, N. Martín and R. Miranda, *Adv. Mater*, 2011, **23**, 5148-5176.
8. R. Otero, W. Xu, M. Lukas, R. E. A. Kelly, E. Lægsgaard, I. Stensgaard, J. Kjems, L. N. Kantorovich and F. Besenbacher, *Angew. Chem*, 2008, **120**, 9819-9822.
9. F. De Marchi, D. Cui, J. Lipton-Duffin, C. Santato, J. M. MacLeod and F. Rosei, *J. Chem. Phys*, 2015, **142**, 101923.
10. M. D'Ischia, A. Napolitano, A. Pezzella, E. J. Land, C. A. Ramsden and P. A. Riley, in *Advances in Heterocyclic Chemistry*, ed. R. K. Alan, Academic Press, 2005, vol. Volume 89, pp. 1-63.
11. Q. Ye, F. Zhou and W. Liu, *Chem. Soc. Rev*, 2011, **40**, 4244-4258.
12. E. Faure, C. Falentin-Daudré, C. Jérôme, J. Lyskawa, D. Fournier, P. Woisel and C. Detrembleur, *Prog. Polym. Sci*, 2013, **38**, 236-270.
13. A. C. Marele, I. Corral, P. Sanz, R. Mas-Ballesté, F. Zamora, M. Yáñez and J. M. Gómez-Rodríguez, *J. Phys. Chem. C*, 2013, **117**, 4680-4690.
14. H.-M. Zhang, J.-W. Yan, Z.-X. Xie, B.-W. Mao and X. Xu, *Chem. Eur. J*, 2006, **12**, 4006-4013.

15. S. Buchholz and J. P. Rabe, *Angew. Chem. Int. Ed*, 1992, **31**, 189-191.
16. L. Giovanelli, O. Ourdjini, M. Abel, R. Pawlak, J. Fujii, L. Porte, J.-M. Themlin and S. Clair, *J. Phys. Chem. C*, 2014, **118**, 14899-14904.
17. R. Pawlak, S. Clair, V. Oison, M. Abel, O. Ourdjini, N. A. A. Zwaneveld, D. Gigmes, D. Bertin, L. Nony and L. Porte, *ChemPhysChem*, 2009, **10**, 1032-1035.
18. S. Clair, S. Pons, A. P. Seitsonen, H. Brune, K. Kern and J. V. Barth, *J. Phys. Chem. B*, 2004, **108**, 14585-14590.
19. D. G. Graham, *Mol. Pharmacol*, 1978, **14**, 633-643.
20. Y. Liu, K. Ai and L. Lu, *Chem. Rev*, 2014, **114**, 5057-5115.
21. J. Yang, M. A. Cohen Stuart and M. Kamperman, *Chem. Soc. Rev*, 2014, **43**, 8271-8298.
22. S. Hong, Y. S. Na, S. Choi, I. T. Song, W. Y. Kim and H. Lee, *Adv. Funct. Mater*, 2012, **22**, 4711-4717.
23. M. Ambrico, P. F. Ambrico, T. Ligonzo, A. Cardone, S. R. Cicco, M. D'Ischia and G. M. Farinola, *J. Mater. Chem. B*, 2015, **3**, 6413-6423.
24. J. Wünsche, L. Cardenas, F. Rosei, F. Cicoira, R. Gauvin, C. F. O. Graeff, S. Poulin, A. Pezzella and C. Santato, *Adv. Funct. Mater*, 2013, **23**, 5591-5598.
25. S. J. Orlow, M. P. Osber and J. M. Pawelek, *Pigment Cell Melanoma Res*, 1992, **5**, 113-121.
26. M. D'Ischia, K. Wakamatsu, A. Napolitano, S. Briganti, J. C. Garcia-Borron, D. Kovacs, P. Meredith, A. Pezzella, M. Picardo, T. Sarna, J. D. Simon and S. Ito, *Pigment Cell Melanoma Res*, 2013, **26**, 616-633.
27. J. Björk, F. Hanke and S. Stafström, *J. Am. Chem. Soc*, 2013, **135**, 5768-5775.
28. J. Björk, Y.-Q. Zhang, F. Klappenberger, J. V. Barth and S. Stafström, *J. Phys. Chem. C*, 2014, **118**, 3181-3187.
29. A. Corani, A. Huijser, T. Gustavsson, D. Markovitsi, P.-Å. Malmqvist, A. Pezzella, M. D'Ischia and V. Sundström, *J. Am. Chem. Soc*, 2014, **136**, 11626-11635.
30. I. Horcas, R. Fernandez, J. M. Gomez-Rodriguez, J. Colchero, J. Gomez-Herrero and A. M. Baro, *Rev. Sci. Instrum*, 2007, **78**.
31. G. Kresse and J. Hafner, *Phys. Rev. B*, 1993, **47**, 558-561.
32. G. Kresse and J. Furthmüller, *Phys. Rev. B*, 1996, **54**, 11169-11186.
33. J. P. Perdew, M. Ernzerhof and K. Burke, *J. Chem. Phys.*, 1996, **105**, 9982-9985.
34. P. E. Blöchl, *Phys. Rev. B*, 1994, **50**, 17953-17979.
35. G. Kresse and D. Joubert, *Phys. Rev. B*, 1999, **59**, 1758-1775.
36. S. Grimme, J. Antony, S. Ehrlich and H. Krieg, *J. Chem. Phys.*, 2010, **132**, 154104.
37. S. Grimme, *J. Comput. Chem.*, 2006, **27**, 1787-1799.
38. K. Momma and F. Izumi, *J. Appl. Crystallogr*, 2011, **44**, 1272-1276.
39. Frisch, M.; Trucks, G.; Schlegel, H. B.; Scuseria, G.; Robb, M.; Cheeseman, J.; Scalmani, G.; Barone, V.; Mennucci, B.; Petersson, G., Gaussian 09, revision a. 02, gaussian. *Inc., Wallingford, CT* **2009,** *200*.
40. D. Landau and K. Binder, *A Guide to Monte Carlo Simulations in Statistical Physics*, Cambridge University Press, 2005.
41. S. Stepanow, N. Lin, D. Payer, U. Schlickum, F. Klappenberger, G. Zoppellaro, M. Ruben, H. Brune, J. V. Barth and K. Kern, *Angew. Chem*, 2007, **119**, 724-727.
42. A. C. Papageorgiou, J. Li, S. C. Oh, B. Zhang, O. Saglam, Y. Guo, J. Reichert, A. B. Marco, D. Cortizo-Lacalle, A. Mateo-Alonso and J. V. Barth, *Nanoscale*, 2018, DOI: 10.1039/C8NR02537A.
43. F. Bebensee, K. Svane, C. Bombis, F. Masini, S. Klyatskaya, F. Besenbacher, M. Ruben, B. Hammer and T. Linderoth, *Chem. Comm*, 2013, **49**, 9308-9310.

44. B. Yang, J. Björk, H. Lin, X. Zhang, H. Zhang, Y. Li, J. Fan, Q. Li and L. Chi, *J. Am. Chem. Soc*, 2015, **137**, 4904-4907.
45. S. Yumitori, *Journal of Materials Science*, 2000, **35**, 139-146.
46. G. Beamson and D. Briggs, High Resolution XPS of Organic Polymers: The Scienta ESCA300 Database, Wiley, 1992.
47. R. J. J. Jansen and H. van Bekkum, *Carbon*, 1995, **33**, 1021-1027.
48. S. Garcia-Gil, A. Arnau and A. Garcia-Lekue, *Surf. Sci*, 2013, **613**, 102-107.
49. M. Chen, J. Xiao, H.-P. Steinrück, S. Wang, W. Wang, N. Lin, W. Hieringer and J. M. Gottfried, *J. Phys. Chem. C*, 2014, **118**, 6820-6830.
50. D. A. Hutt and C. Liu, *Appl. Surf. Sci*, 2005, **252**, 400-411.
51. M. Šimėnas and E. E. Tornau, *J. Chem. Phys*, 2013, **139**, 154711.
52. S. J. Stoneburner, V. Livermore, M. E. McGreal, D. Yu, K. D. Vogiatzis, R. Q. Snurr and L. Gagliardi, *J. Phys. Chem. C*, 2017, **121**, 10463-10469.
53. A. Ibenskas, M. Šimėnas and E. E. Tornau, *J. Phys. Chem. C*, 2018, **122**, 7344-7352.
54. A. Basagni, L. Ferrighi, M. Cattelan, L. Nicolas, K. Handrup, L. Vaghi, A. Papagni, F. Sedona, C. D. Valentin, S. Agnoli and M. Sambi, *Chem. Comm*, 2015, **51**, 12593-12596.
55. L. Jiang, A. C. Papageorgiou, S. C. Oh, Ö. Sağlam, J. Reichert, D. A. Duncan, Y.-Q. Zhang, F. Klappenberger, Y. Guo, F. Allegretti, S. More, R. Bhosale, A. Mateo-Alonso and J. V. Barth, *ACS Nano*, 2016, **10**, 1033-1041.
56. Q. Li, B. Yang, H. Lin, N. Aghdassi, K. Miao, J. Zhang, H. Zhang, Y. Li, S. Duhm, J. Fan and L. Chi, *J. Am. Chem. Soc*, 2016, **138**, 2809-2814.
57. L. Lafferentz, V. Eberhardt, C. Dri, C. Africh, G. Comelli, F. Esch, S. Hecht and L. Grill, *Nat. Chem*, 2012, **4**, 215.
58. D. Zhong, J.-H. Franke, S. K. Podiyanachari, T. Blömker, H. Zhang, G. Kehr, G. Erker, H. Fuchs and L. Chi, *Science*, 2011, **334**, 213-216.
59. D. Billaud, E. B. Maarouf and E. Hannecart, *Synth. Met*, 1995, **69**, 571-572.
60. A. Pezzella, A. Napolitano, M. D'Ischia and G. Prota, *Tetrahedron*, 1996, **52**, 7913-7920.
61. L. Panzella, A. Pezzella, M. Arzillo, P. Manini, A. Napolitano and M. D'Ischia, *Tetrahedron*, 2009, **65**, 2032-2036.
62. A. Pezzella, O. Crescenzi, L. Panzella, A. Napolitano, E. J. Land, V. Barone and M. d'Ischia, *J. Am. Chem. Soc*, 2013, **135**, 12142-12149.
63. H. Okuda, K. Wakamatsu, S. Ito and T. Sota, *J. Phys. Chem. A*, 2008, **112**, 11213-11222.
64. P. Manini, V. Criscuolo, L. Ricciotti, A. Pezzella, M. Barra, A. Cassinese, O. Crescenzi, M. G. Maglione, P. Tassini, C. Minarini, V. Barone and M. D'Ischia, *ChemPlusChem*, 2015, **80**, 919-927.
65. X.-C. Li, C.-Y. Wang, W.-Y. Lai and W. Huang, *J. Mater. Chem. B*, 2016, **4**, 10574-10587.

CHAPTER 5: THE POLYMORPHISM OF DHICA

In the two previous chapters we have shown how the functional group define the final structure of the self-assembled network. While carboxylic acids dominate the self-assembling process by creating very stable non-covalent dimers acid dimers, a variety of 2D architectures are possible because of the multiple weak interactions of the catechol group. But what happens when these two groups are simultaneously present? In this chapter the final eumelanin precursor, the result concerning our investigation over DHICA, will be presented. Compared to the two previous model systems, the presence of both these functional groups in DHICA increases the possible number of interactions, allowing the creation of self-assembled molecular networks (SAMNs) with different bonding motifs.

The STM and XPS characterization of the numerous phases of DHICA was done by Mr. Galeotti and me, hence we share again the first author contribution. Under the supervision of prof. Chi, Mr. Ji repeated some of our experiments, to ensure the reproducibility of the results. Prof. Tornau and Dr. Simenas supported us with the MC modelling of DHICA, based on the DFT gas phase calculation of Dr. Ebrahimi. Dr. Pezzella synthesized more eumelanin precursor for us to test, and participated in the discussion over the manuscript preparation with Dr. MacLeod.

Self-assembly of 5,6-dihydroxyindole-2-carboxylic acid: polymorphism of a eumelanin building block on Au(111)

Published on Nanoscale, 10, 16721 (2018); doi: 10.1039/C8NR04002H

F. De Marchi,[1] G. Galeotti,[1] M. Simenas,[2] P. Ji,[1,3] L. Chi,[3] E. E. Tornau,[4] A. Pezzella,5,6 J. MacLeod,[7] M. Ebrahimi[1] and F. Rosei[1,8]

[1]Centre Energie, Materiaux et Telecommunications, Institut National de la Recherche Scientifique, 1650 Boulevard Lionel-Boulet, Varennes, QC, Canada J3X 1S2.

[2]Faculty of Physics, Vilnius University, Saulėtekio 9, LT-10222 Vilnius, Lithuania

[3]Jiangsu Key Laboratory for Carbon-Based Functional Materials & Devices, Institute of Functional Nano & Soft Materials, Soochow University, Suzhou 215123, PR China

[4]Semiconductor Physics Institute, Center for Physical Sciences and Technology, Saulėtekio 3, LT-10222 Vilnius, Lithuania 5

[5]Institute for Polymers, Composites and Biomaterials (IPCB), CNR, Via Campi Flegrei 34, I-80078 Pozzuoli, NA, Italy

[6]National Interuniversity Consortium of Materials Science and Technology (INSTM), Florence 50121, Italy

[7]School of Chemistry, Physics and Mechanical Engineering and Institute for Future Environments, Queensland University of Technology (QUT), 2 George Street, Brisbane, 4001 QLD, Australia.

[8]Institute for Fundamental and Frontier Science, University of Electronic Science and Technology of China, Chengdu 610054, PR China

Abstract

Investigating two-dimensional (2D) self-assembled structures of biological monomers governed by intermolecular interactions is a prerequisite to understand the self-assembly of more complex biomolecular systems. 5,6-dihydroxyindole carboxylic acid (DHICA) is one of the building blocks of eumelanin - an irregular heteropolymer and the most common form of melanin which has potential applications in organic electronics and bioelectronics. By means of scanning tunneling microscopy, density functional theory and Monte Carlo calculations, we investigate DHICA molecular configurations and interactions underlying the multiple 2D patterns formed on Au(111). While DHICA self-assembled molecular networks (SAMNs) are dominated by the hydrogen bonding of carboxylic acid dimers, a variety of 2D architectures are formed due to the multiple weak interactions of the catechol group. The hydroxyl group also allows for redox reactions, caused by oxidation via O_2 exposure, resulting in molecular rearrangement. The susceptibility of the molecules to oxidation is affected by their SAMNs architectures, giving insights on the reactivity of indoles as well as highlighting noncovalent assembly as an approach to guide selective oxidation reactions.

5.1 Introduction

The design of new organic materials is inspired by observation of biological systems, in which self-assembled structures are fundamental to the complex functions of living cells.[1, 2] Scanning tunneling microscopy (STM) allows the imaging of these systems on atomically flat surfaces at the nanoscale, in a reduced complexity environment, probing the interfacial and intermolecular interactions that regulate the self-assembly processes. This has enabled progress towards the fundamental understanding of these interactions, leading to valuable insights into the macroscopic behaviour of biological systems.[3, 4] In addition, these investigations further improve our ability to predict a priori the outcome of self-assembly processes,[5] which is a critical step toward engineering the properties of 2D nanostructures. For example, the investigation of the nucleic acid self-assembly on Au(111) helped unravel the molecular recognition process in RNA strands,[6] while at the same time laid the foundation for the formation of 2D nucleic acid oligomers.[7,8] In this framework, we investigated the self-assembly of the monomers of eumelanin - an elusive class of black insoluble polymers derived biogenetically from tyrosine, which exist in human and mammalian skin, hair, eyes as well as in cephalopod ink.[9,10] Eumelanin's unique characteristics, such as strong optical absorption and hydration-dependent electrical conductivity,[11] have motivated research towards its potential application in organic electronics and bioelectronics.[12-14] However, in depth study of eumelanin is hampered by its chemical intractability and the multiple cross-linked bonds that its building blocks form upon polymerization.[15, 16] Despite extensive experimental studies, the relation between the structure, composition, and aggregation of eumelanin is still an intriguing open question.[17]

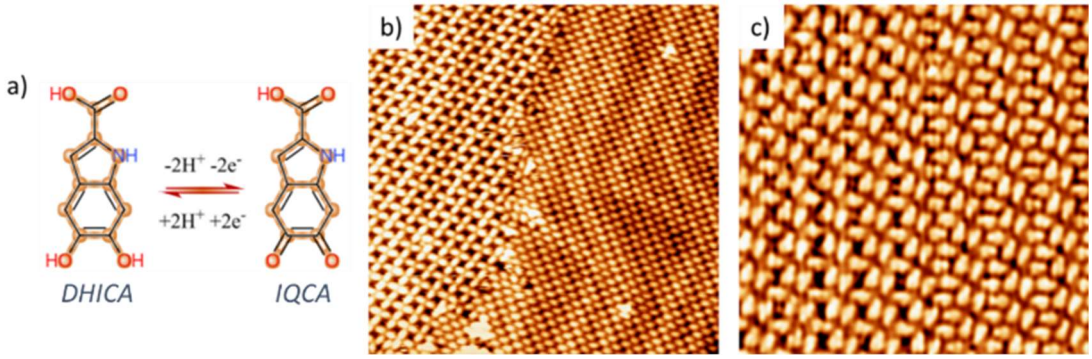

Figure 5.1: a) DHICA oxidation into indolequinone carboxylic acid (IQCA). STM images of the DHICA self-assembled networks on Au(111): b) 30×30 nm² open lattice and brick-wall phase (It=-0.1 nA, Vt=-0.9 V) c) 18×18 nm² ladder phase (It=-0.1 nA, Vt=-0.3 V)

To shed light upon the interactions between eumelanin monomers, we deposited indole molecules on a surface to investigate the effect of each functional group on the selfassembly process. As we have seen for indole 2-carboxylic acid (I2CA), regardless of the preparation condition, a head-head dimer pair is formed by hydrogen bonding between two carboxylic groups that are arranged in lamellae stabilized by weak side interactions between the indole backbones.[18] For 5,6-dihydroxyindole (DHI), the presence of two hydroxyls in ortho position on the phenyl ring (catechol) opens the door to redox reactions.[19] As such, DHI molecules generate metalorganic complexes on silver, while on gold, a covalent dimer of DHI is formed at room temperature (RT).[20-22]

To further extend this investigation, here we report our results regarding the deposition of 5,6-dihydroxyindole-2-carboxylic acid (DHICA) on Au(111) in ultra-high vacuum (UHV) conditions, studying the intermolecular interactions that lead to the formation of DHICA non-covalent 2D nanostructures. DHICA is another intermediate in the biosynthesis of eumelanin which presents the functional groups of both the aforementioned molecules: a carboxylic acid and a catechol similar to I2CA and DHI, respectively (Figure 5.1a). Compared to I2CA and DHI, the presence of both functional groups in DHICA increases the possible number of interactions, allowing the creation of self-assembled molecular networks (SAMNs) with different bonding motifs (Figure 5.1b and c). When exposed to O_2,[23] DHI undergoes an oxidation in which catechol group converts into quinone. Here we show that the susceptibility to this process in DHICA is perturbed by the carboxyl group as its presence affects the redox potential of the molecule.[24] In addition, the position of the -COOH on the pyrrole ring of DHICA avoids the formation of a planar covalent dimer, which was previously witnessed for DHI on Au(111).We show that DHICA SAMNs can be affected by exposure to O_2 on Au, triggering a phase transition toward more complex structures reminiscent of the mixed DHI/indolequinone (IQ) phases.[23, 25, 26] We used STM to gain information about the network architecture, and density functional theory (DFT) as well as Monte Carlo (MC) calculations to corroborate our interpretation of the molecular structures.

5.2 Experimental

DHICA was obtained commercially (Toronto Research Chemicals) and also synthesized by reacting L-DOPA with $K_3Fe(CN)_6$ and $NaHCO_3$.[27] The purity of the chemical was 95+%, and no significant change in the data was witnessed between different manufacturers. DHICA powder was stored at -20 °C to avoid polymerization. All the experiments were

performed under UHV conditions in a system with a base pressure of 10^{-10} mbar. The Au(111) surface (Princeton Scientific Corp.) was cleaned by sequential sputtering (0.8 to 1.2 keV at 10^{-5} mbar of Ar for 15 minutes) and annealing (480°C for 30 minutes) prior to deposition. DHICA was deposited on the surface in a Molecular Beam Epitaxy (MBE) chamber using an effusion (Knudsen) cell. The evaporator was kept at 85°C for 60 minutes to achieve monolayer coverage on Au(111). The STM imaging was performed using a SPECS Aarhus 150 STM. To trigger oxidation, samples were exposed to gaseous O_2 by dosing through a leak valve to a pressure of 10^{-5} mbar for 30 minutes.

STM images were analyzed using WSxM software.[28] The images were calibrated using the known Au(111) lattice constant, either from the same image or from images of the clean surface acquired on the same day. Additional details on how the lattice correction was performed are reported in section 5.5.1 of the supplementary information. DFT calculations were performed with the Vienna Ab-initio Simulation Package (VASP).[29, 30] The calculations were carried out using the Perdew-Burke-Ernzerhof[31] approximation (PBE) of the exchange-correlation potential, the projector augmented wave (PAW) method,[32,33] and a plane-wave basis set with an energy cut-off of 450 eV. DFT-D3 method of Grimme,[34,35] was applied to account for the dispersion forces, the non-covalent interactions between the molecules. For the simulations of the reported SAMNs, the structures were optimized in the gas phase in which all atoms were relaxed. All the calculations were performed at the gamma point until the net force on each atom was less than 0.02 eV/Å and the energy change between the two steps was smaller than 0.00001 eV. The optimized structures are presented using VESTA software.[36] Unless stated otherwise, the reported energies are per molecule. The supercell dimensions were taken from the experimental data (Table 5.1). The bonding energies of the dimer and trimer DHICA arrangements required for MC simulations were performed using B3LYP functional and 6-31G(d,p) basis set with DFT-D3 correction,[34,35] included. To mimic the planar arrangement, the out-of-plane relaxation of the carbon atoms was restrained. MC simulations[37] were performed using the Metropolis algorithm and Kawasaki dynamics keeping the molecular concentration fixed close to the concentration value of the ideal phases. A square lattice with the periodic boundary conditions of size L × L (L = 50-100) was implemented. A randomly selected molecule was allowed to rotate and jump into an unoccupied lattice site with a probability P = min [1, $e^{-\frac{\Delta E}{kT}}$, where ΔE is the energy difference between the final (after the jump) and the initial (before the jump) state of the system. The

Boltzmann constant and temperature are denoted by k and T, respectively. Up to 10^7 MC steps per site were performed to ensure proper equilibration at each temperature.

5.3 Results and discussion

Once deposited on Au(111), DHICA molecules self-assemble into a number of different motifs, with multiple phases, often simultaneously present on the surface. The most abundant ones are shown in Figure 5.2. In all the phases, the unaltered herringbone reconstruction of Au(111) can be seen in the STM images, indicating that the interactions between the molecule and substrate are not strong enough to perturb the surface reconstruction.[38] The most commonly imaged assembly is presented in Figure 5.2a, which we refer to as the open lattice phase. DHICA forms dimer couples, disposed in a square lattice (u = 1.83 ± 0.05 nm, v = 1.83 ± 0.05 nm, θ = 92 ± 3°), forming large 2D domains. Each dimer is oriented almost perpendicular to its neighbours, with its extremities pointing towards the middle of the neighbouring pairs. These observations suggest that the phase is stabilized by the hydrogen bonding between carboxylic groups, as well as being further strengthened by the intermolecular interactions between the catechol and the carboxyl, as shown in Figure 5.2a and d.

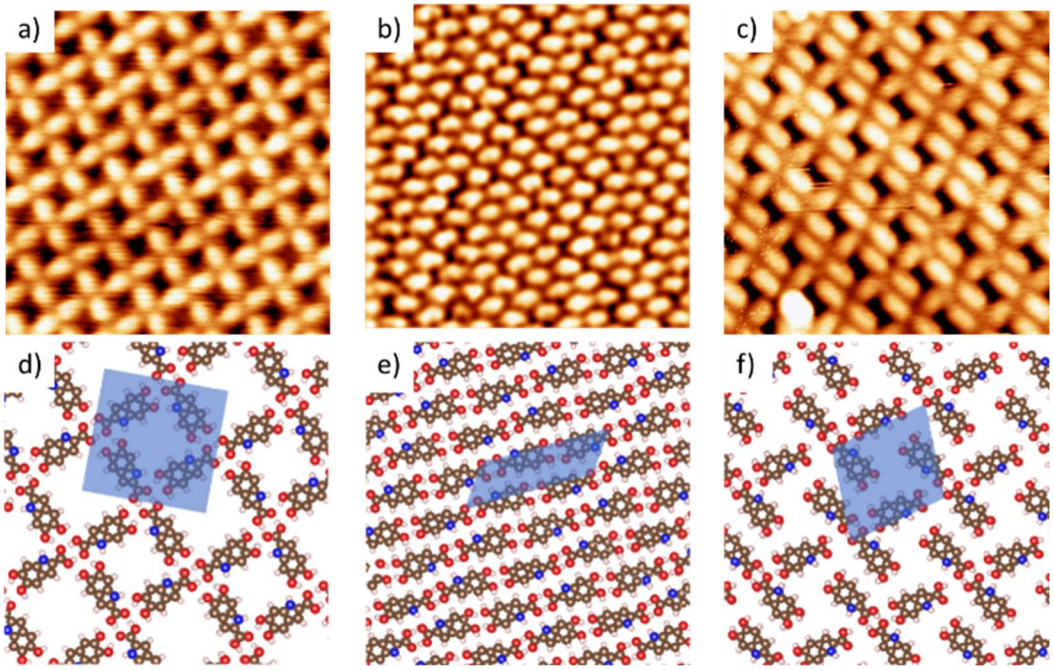

Figure 5.2: 10×10 nm^2 STM images of the DHICA on Au (111) a) open lattice (It=0.1 nA, Vt=0.9 V), b) brick wall (It=0.1 nA, Vt=0.9 V) and c) ladder phases (It=0.1 nA, Vt=0.6 V). DFT simulated structures corresponding to a, b, c are shown in d, e, f, respectively.

DHICA molecules also self-assemble in a brick wall structure, presented in Figure 5.2b, with lattice parameters u= 0.74 ± 0.05 nm, v = 2.06 ± 0.05 nm, θ = 133 ± 3°. In this phase, DHICA molecules are arranged in a tightly packed linear conformation. From the STM images it is not clear how each single molecule is disposed, since both head-head and head-tail conformations could match the unit cell. By comparing the cohesive energy of the two systems simulated by DFT (Figure 5.2e and 5.8), we find that the head-head conformation is more stable by 6.0 kcal/mol. The last major structure, which we refer to as the ladder phase, incorporates DHICA molecules in a conformation similar to the open lattice, composed of perpendicular rows of monomers and dimers disposed to form small porous square in a chain-like motif (u = 1.25 ± 0.05 nm, v = 2.05 ± 0.05 nm, θ = 125± 3°, Figure 5.2c). DFT simulations show that this structure presents bonding motifs common to both the other two self-assembled phases: the molecules are arranged in carboxylic dimer pairs, stacked side by side similarly to the brick wall, surrounded by molecules with their functional groups pointing toward the -COOH dimer as in the open lattice phase (Figure 5.2f).

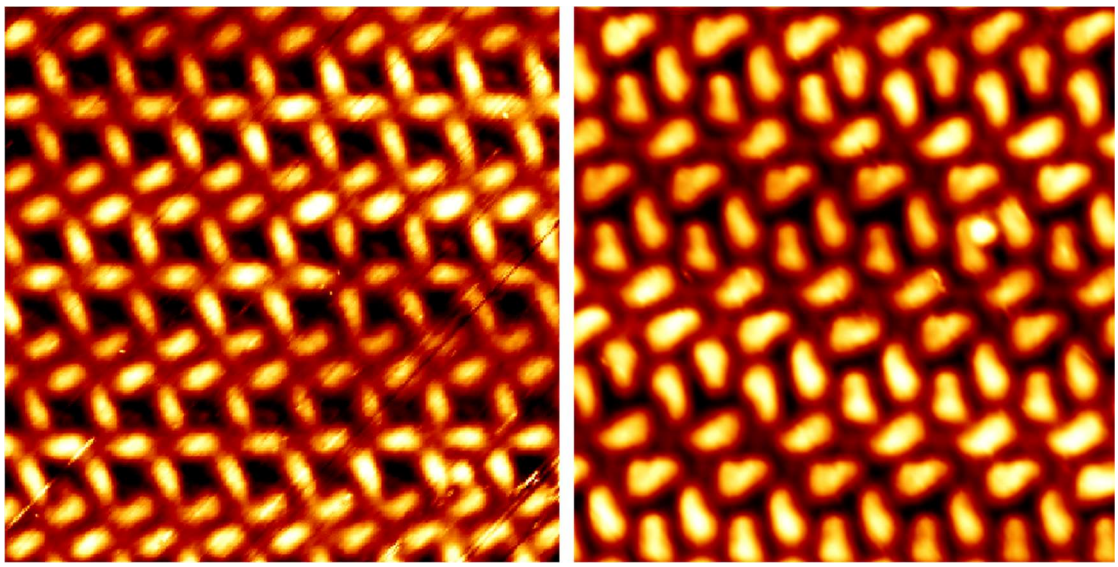

Figure 5.3: Less common self-assembled structure of DHICA on the Au(111) surface a) (I_t=0.1 nA, V_t=1.2 V) b) (I_t=0.1 nA, V_t=0.5 V).

Furthermore, we observed other phases (Figures 5.3 and 5.10) which present bonding motifs very similar to the three phases described in Figure 5.2. Such polymorphism is not uncommon for self-assembled molecular system, and different bonding architectures can be obtained by controlling deprotonation with surface temperature,[39] by varying the molecular density on the surface,[40,41] or by adsorption/desorption of additional chemical

species.[42, 43] In contrast, in our experiments the annealing of the self-assembled phases does not alter the molecular rearrangement. Multiple phases are often simultaneously present on the same terrace, and even the most close-packed arrangements are obtained for submonolayer coverages (Figure 5.11). Furthermore, a phase transition from a porous to a dense phase does not occur by depositing more molecule via subsequent depositions. A possible reason behind the DHICA polymorphism is that we are instead looking into a multicomponent system, with the molecules partially oxidized on the surface. In fact, it has been shown that by changing the ratio between the components of the molecular overlayer, different self-assembled phases can be obtained.[44, 45]

On the other hand, coexistence of multiple phases is not limited to multi-components systems. The molecular interactions that drive the self-assembly process toward different outcomes could be balanced by one another; as a consequence, there would be no predominance of a given phase with respect to another.[46] The presence of multiple functional groups may support this hypothesis and explain the observed molecular polymorphism. Taking a closer look at the bonding geometries of the observed phases, it is apparent that in all cases DHICA is stabilized through strong interactions between the carboxyl groups. The reason can be elucidated by comparing the energies of different hydrogen bonds (Figure 5.4), where the cyclic -COOH dimer is at least twice as strong as the other interactions. On the other hand, the catechol group can adopt several different bonding conformations to form hydrogen bonds, either linear with another catechol or perpendicular by interaction with the nitrogen and oxygen of a neighbouring DHICA. These catechol bonding arrangements are rather close in energy, so multiple phases would be accessible at RT, which is consistent with our experimental observations.

Table 5.1: Energy parameters for the different DHICA/Au(111) self-assembled networks. Values reported are in kcal/mol.

	e_{hh}	e_{ht}	e_{tt}	e_{hh}^{p}	e_{th}^{p}	e_{tt}^{p}	e_{tt}^{p}	e_{tt}^{p}
Open lattice	-25.1	-8.8	-6.3	-11.3	-13.8	-5.0	-3.8	-3.8
Brick Wall	-25.1	-11.6	-8.5	-12.6	-10.0	-5.0	-5.0	-5.0
Ladder	-25.1	-8.8	-6.3	-12.6	-10.0	-5.0	-5.0	-3.8

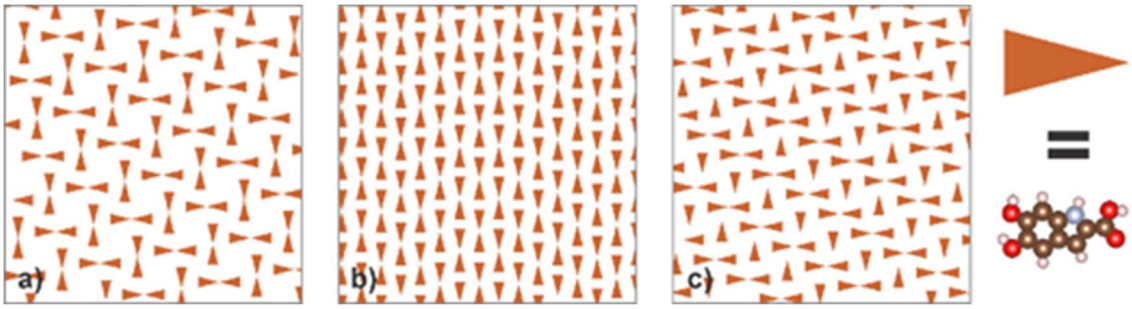

Figure 5.4: The ordered structures of DHICA obtained by MC calculations: a) open lattice, b) brick wall and c) ladder phases

To further support this claim, we performed MC simulations of DHICA self-assembly using a four-state statistical model which includes axial, perpendicular and side dimeric interactions between the molecules (see section 5.5.3). Similar models were previously applied to study the ordering of other molecules, including DHI.[23, 47-49] We were able to obtain the open lattice, brick wall and ladder experimental phases (Figure 5.5) by MC simulation, using slightly different interaction energies as compared with the gas phase DFT calculated energies (Figure 5.4). However, we tried to keep the energy parameters (reported in Table 5.2) as close as possible to the DFT results. It should be noted that the set of parameters for the brick wall phase almost coincides with the values determined by DFT except for smaller e_{hh}^{p} (DFT value is 17.09 kcal/mol). The very close sets of energies support the idea that the polymorphism of DHICA at RT is due to similar interaction energies of these phases rather than different redox state of the molecule.

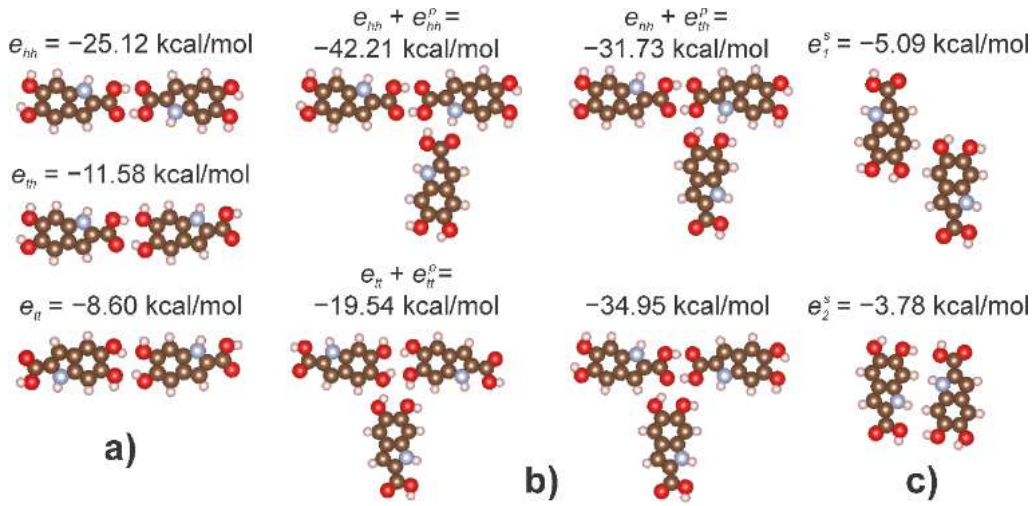

Figure 5.5: Gas-phase DFT calculation of the bonding energies between DHICA molecules in a) axial, b) perpendicular and c) side arrangements. In the denotations of dimeric interaction energies, subscripts "hh", "th" and "tt" indicate carboxyl-carboxyl, carboxyl-catechol and catechol-catechol interactions. Superscripts "p" and "s" denote perpendicular and side arrangements of the molecules.

While this is in agreement with our previous study of DHI,[23] where we did not observe any catechol-to-quinone oxidation conversion for the adsorbed molecules on the gold surface, we cannot exclude the presence of different redox forms of DHICA based only on the simulation results. To evaluate if the network polymorphism is related to different oxidation states ratios in the molecular assembly, we attempted to trigger the oxidation of the catecholic part of the molecule by exposing the molecule to O_2 gas, up to the highest pressure that can sustain UHV conditions. As reported in the literature,[50] the partial pressure of oxygen adopted for such experiments (up to 10^{-5} mbar for 30 minutes) is not high enough to have a significant effect on the clean surface at RT.

We found that the exposure of DHICA/Au(111) samples to O_2 leads to several outcomes, depending on the starting phase Similar to our previous observation on the DHI covalent dimer phase,[23] the DHICA open lattice phase is found to be unaffected by O_2 exposure (Figure 5.12a). The other phases are more strongly affected, becoming disordered as they are exposed to increasing partial pressures of O_2. A phase transition occurs after exposing the molecule to 10^{-5} mbar of O_2, producing a structure with dimer pairs arranged in rows, separated by thin lines that could correspond to the diffusing species (Figure 5.13b).[51] In contrast to the SAMNs unexposed to oxygen, annealing the disordered phases obtained after O_2 exposure leads to a rearrangement of the SAMNs. After thermal annealing at 100 °C, oxygen-exposed DHICA rearranges into a complex honeycomb structure lattice (u = 3.85 ± 0.1 nm, v = 3.85 ± 0.1 nm, θ= 120 ± 3°) whose unit cell contains 18 molecules, as shown in Figure 5.6. Molecules are arranged in a flower-like circular structure, forming two concentric rings: six molecules are located at the centre of the structure, pointing inward toward the centre of the honeycomb, while twelve more are closely packed to form a second concentric ring. The molecules in the outer ring are oriented to accommodate the formation of linear dimer pairs, in an arrangement reminiscent of the ladder structure obtained at RT. In contrast to a similar cyclic structure formed from I2CA,[52] we notice that we have high symmetry (without any apparent chirality) in the assembly. This suggests that the central molecular flower-like arrangement may not arise from hydrogen bonding of the carboxylic moieties, since that has been observed to break the symmetry and induce a chiral twist. Another possible interpretation for this configuration is that the molecules are deprotonated, and six of them are coordinated around one or more Au adatoms, in a conformation similar to the one observed for 1,3,5-benzenetricarboxylic acid on Ag(111) by Lipton-Duffin et al.[53]

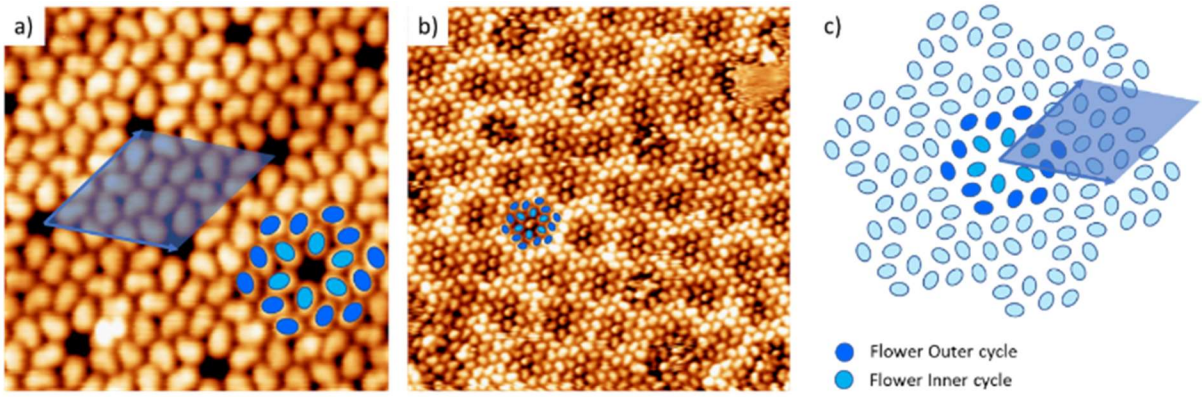

Figure 5.6: STM image of DHICA/Au(111) after been exposed to O_2 and annealed a) 9×9 image (I_t=1.1 nA, V_t=1.7 V) b) 20×20 (I_t=-1.0 nA, V_t=-1.1 V) c) Model of the molecular disposition of the phase.

This hypothesis is further strengthened by lower bias STM images that show the presence of a dot-like feature at the centre of the flower-like structure, that can be inferred to be related to a gold adatom. Although the carboxylic group may deprotonate after annealing,[54, 55] on gold surfaces this phenomenon has not been reported,[56, 57] probably because the used precursors desorb before the required temperature could be achieved. Furthermore, we witness no change when the annealing step is performed without previous O_2 exposure. The deprotonation could have instead taken place on the hydroxyl moieties. In fact, the difference in contrast between the molecules composing the central structure and the one in their surroundings (Figure 5.6a and b), suggests that these inner cycle molecules may be in a different chemical state than their outer cycle counterparts. In line with what is observed for DHI,[23] in which the catechol and quinone forms of the molecule show a different STM contrast, this suggests that a different redox form of DHICA can be formed after exposure to O_2. We can therefore hypothesize that DHICA molecules are still in their catechol form when deposited on the Au(111) surface. Following the O_2 exposure part of the molecules have their catechol group oxidized into quinone, which reduces their capability to form hydrogen bonds and leads to an increased disorder in the molecular overlayer. The additional annealing step allows the molecule to diffuse on the surface and triggers the phase transition into the flower structure. This puts DHICA in contrast with its counterpart, DHI, which is stabilized through covalent dimerization on Au(111) at RT and does not convert into quinone. It is interesting to note how the open lattice phase, which present a more porous structure and relies mainly on the carboxylic cyclic hydrogen bond, is resistant to oxidation even when exposed to O_2 with a pressure as high as 10^{-5} mbar.

5.4 Conclusions

We studied the self-assembly of DHICA on Au(111), with the goal of investigating how the interaction between the carboxyl and catechol groups drive the self-assembly process. Once on the surface, DHICA molecules rearrange in several polymorphs with different symmetries and packing densities. However, various DHICA SAMNs share a number of similar bonding motifs, suggesting that the self-assembly is driven mainly by the formation of hydrogen bonds between carboxylic acids, which marks the most stable intermolecular interaction of DHICA. The formation of multiple self-assembled phases can be attributed to the relatively weak molecule-substrate interactions, under which the molecules do not react. The molecules remain in their catechol form, exhibiting multiple non-covalent bonding configurations allowed by their functional groups. While the carboxylic cyclic dimer is a feature of all the formed networks, the catechol group participates in a range of different bonding motifs. Our DFT calculations suggest that these geometries have similar interaction energies. MC simulations of the DHICA systems show how even slight perturbations to the relative strength of these interactions can shift the balance, producing the different phases on the surface in line with our experimental observations. We have also observed that the susceptibility of the molecule to oxidation is affected by the morphology of the formed self-assembled structure. After being exposed to O_2, the open lattice phase remains unaltered, while others react to form new phases. It is possible to trigger an additional molecular rearrangement upon thermal annealing. This phase may be composed of a mixed redox forms of DHICA that form a metal-organic structure. Controlled formation of SAMNs, which are prone or resistant to rearrangements following oxidation and annealing, is a promising feature that could form the foundation for the development of sensors or responsive devices. Additional exploration in this arena could lead to implementation of SAMNs in various applications. Moreover, further investigation of similar systems may help to elucidate the fundamental mechanisms underpinning these behaviours which control the architecture of 2D molecular networks.

5.5 Supporting information

5.5.1 STM calibration details

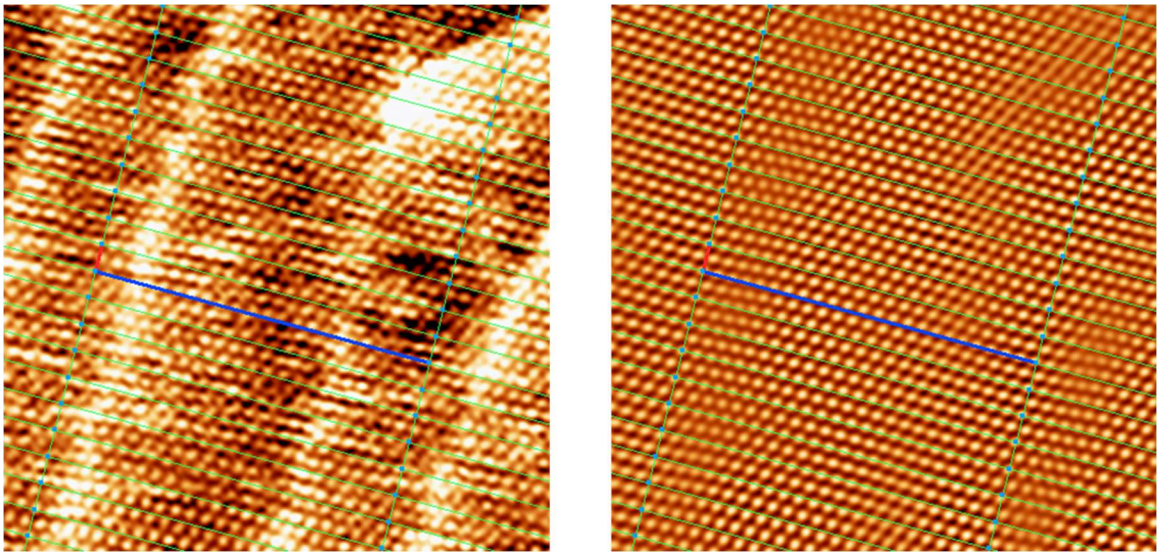

Figure 5.7: An example of the calibration adopted for the DHICA/Au(111), where the clean Au substrate image (3.30 nA, 0.01 V, 10x10 nm^2) is processed and filtered until the single atoms are properly visible. The image is calibrated by using the 6.23 nm herring bone reconstruction dimension ([1-10], blue vector in the image) at 90° respect to the direction of the solitons ([112], red vector in the image) as the distance between 23 atoms.

5.5.2 Additional details on brick wall phase DFT calculations

The observed brick wall phase is formed by all DHICA molecules, as shown by STM in Figure 5.2b in the main text. The molecules can assemble in different configurations, with either a head-to-head or a head-to-tail interaction. Although in the case of two isolated molecules, the head-to-head interaction is preferred (Figure 5.4), additional side interactions are present in a four-molecules unit cell. Nevertheless, our DFT calculations under PBC conditions show that the head-to-head yields the SAMNs with the lowest energy. In addition to being a more stable self-assembly, the head-to-head configuration also has a better agreement with the STM experimental images, preserving the observed symmetry.

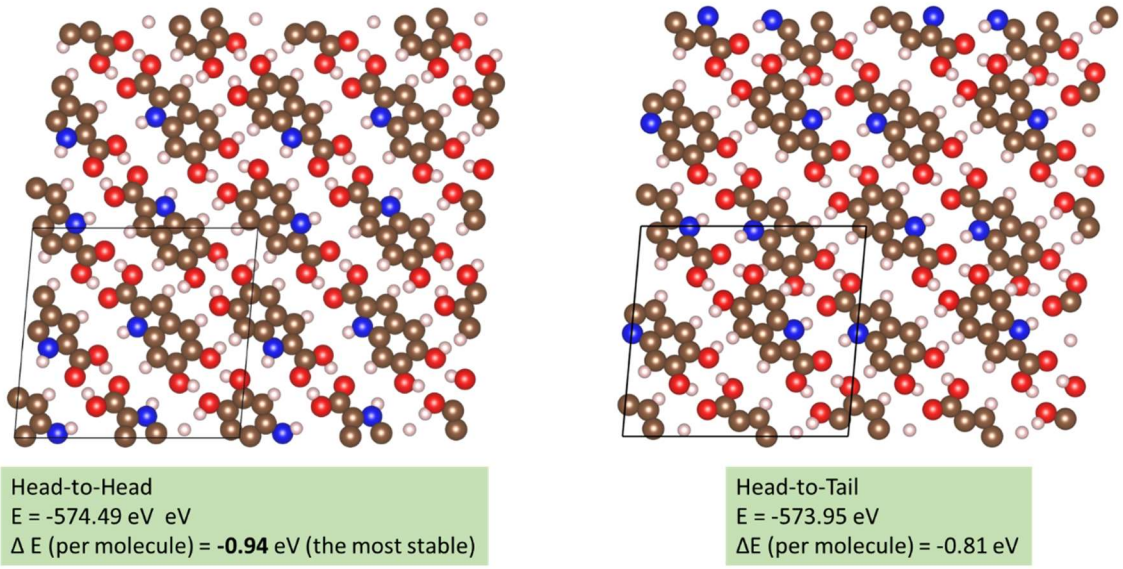

Figure 5.8. Comparison between the cohesive energy of a head-to-head and a head-to-tail conformation

5.5.3 Additional details on Monte Carlo calculations

To describe the ordering of DHICA, we constructed a statistical model which involves four molecular states and main dimeric interactions (see Figure 5.9). First of all, we took into account three axial bondings that occur when two molecules interact via carboxyl (further called head-head, e_{hh} interaction), carboxyl and catechol (head-tail e_{ht}) and catechol (tail-tail, e_{tt}) groups. The gas phase DFT calculation provided the following values of these interaction energies: e_{hh} = −25.12, e_{ht} = −11.58 and e_{tt} = −8.60 kcal/mol (see Figure 5.4a).

We also included and evaluated interactions caused by nearly perpendicular geometries of two interacting molecules. These interactions are obtained from the two-molecule as well as from the three-molecule complexes. In the latter case, the system comprises the main axial dimeric interaction and perpendicular interaction as well. These interactions are called in a same manner as the main axial interactions, but with a superscript “p” for perpendicularity: e_{hh}^{p}, e_{th}^{p} and e_{tt}^{p} (Figure 5.93). The magnitudes of these interactions determined from the three-molecule DFT geometry (see Figure 5.10b) are: $e_{hh}^{p} = -17.09$ and $e_{th}^{p} = -6.61$ kcal/mol. We also obtained the value of the trio complex when the third molecule is not in a perpendicular tail-to-head geometry (i.e. directed to one of the dimer molecules), but has its catechol group directed towards the dimeric bond itself. Such a complex is a bit more stable (-34.95 kcal/mol) than the one with dimeric e_{th}^{p} interaction (-

31.73 kcal/mol), but their energy difference is quite small (3.2 kcal/mol). The interaction $e_{tt}^{p} = -7.32$ kcal/mol was taken from the three-molecule geometry with an additional tail-tail axial interaction (see Figure 5.4b).

Finally, we considered two interactions potentially characteristic to the brick wall and ladder phases when two molecules interact from their sides (Figure 5.9). The denotation of interactions has the superscript "s" for the "side". The magnitudes of these interactions are $e_1^s = -5.09$ and $e_2^s = -3.78$ kcal/mol (Figure 5.4c). Note that in our model we did not take into account the chirality of DHICA, as nitrogen atom barely affects the side interactions. In our model we also take into account that two molecules within a certain close distance cannot coexist, because they either overlap or induce strong repulsion. Such configurations are subjected to infinite exclusion.

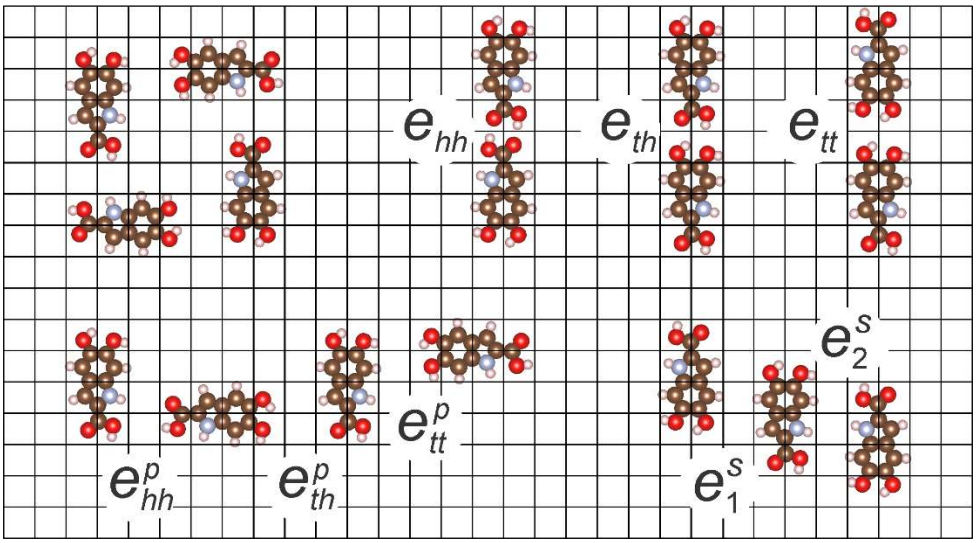

Figure 5.9: Four molecular states of DHICA on a square lattice (above, left) and the eight intermolecular interactions used in MC simulations.

The model was solved using MC simulations on a square lattice. The choice of such a lattice was motivated by the symmetry of the ordered phases. In our model, the distance between the interacting molecules is different for different types of interactions as indicated in Figure 5.9.

Note that we tolerate some freedom in the choice of interaction energies but try to keep a discrepancy from the DFT values as small as possible.

5.5.4 Additional STM images

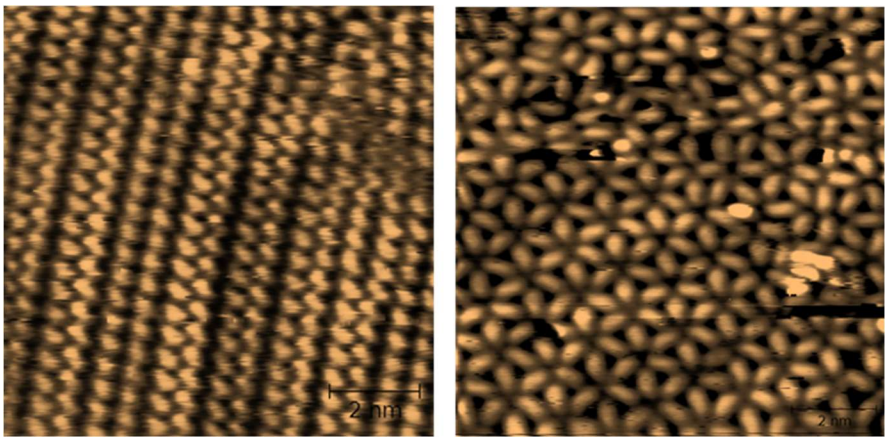

Figure 5.10: Other DHICA SAMNs phases formed on Au(111) at a) RT and b) LT

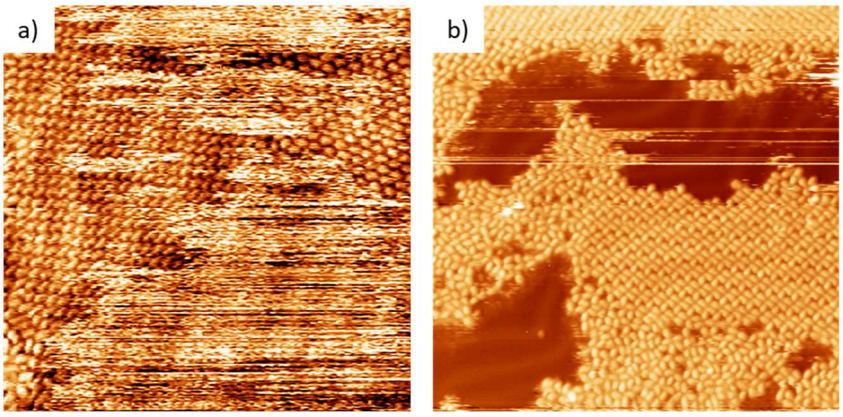

Figure 5.11: STM images of the a) brick wall and b) ladder close packed DHICA phase obtained at submonolayer coverages

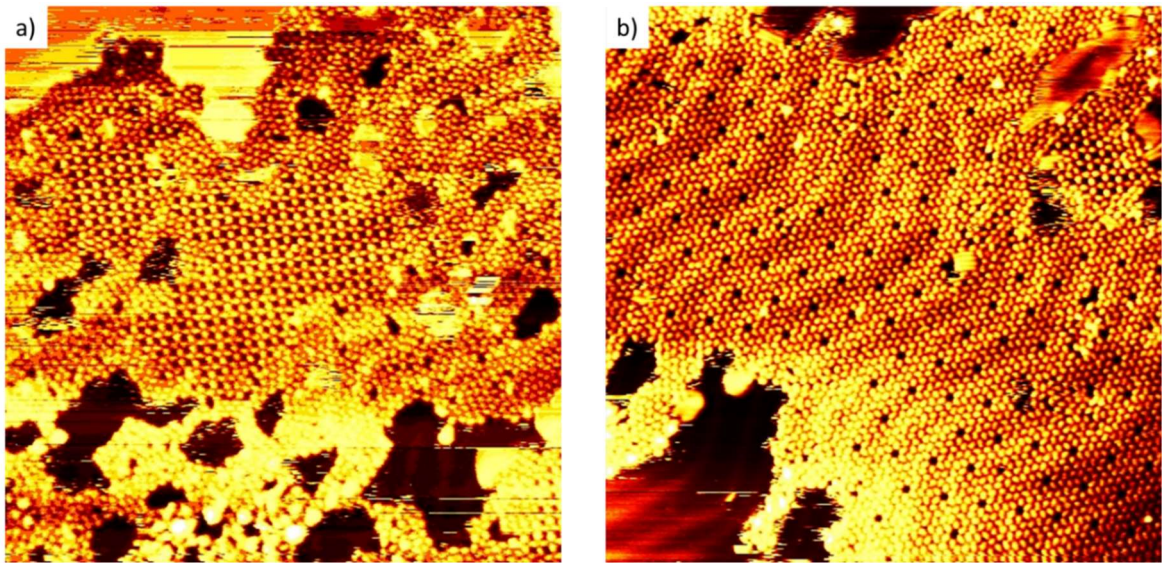

Figure 5.12: DHICA/Au after exposure to O_2 (a) and annealing to 100°C (b). Small domain of open lattice phase is still visible across the surface.

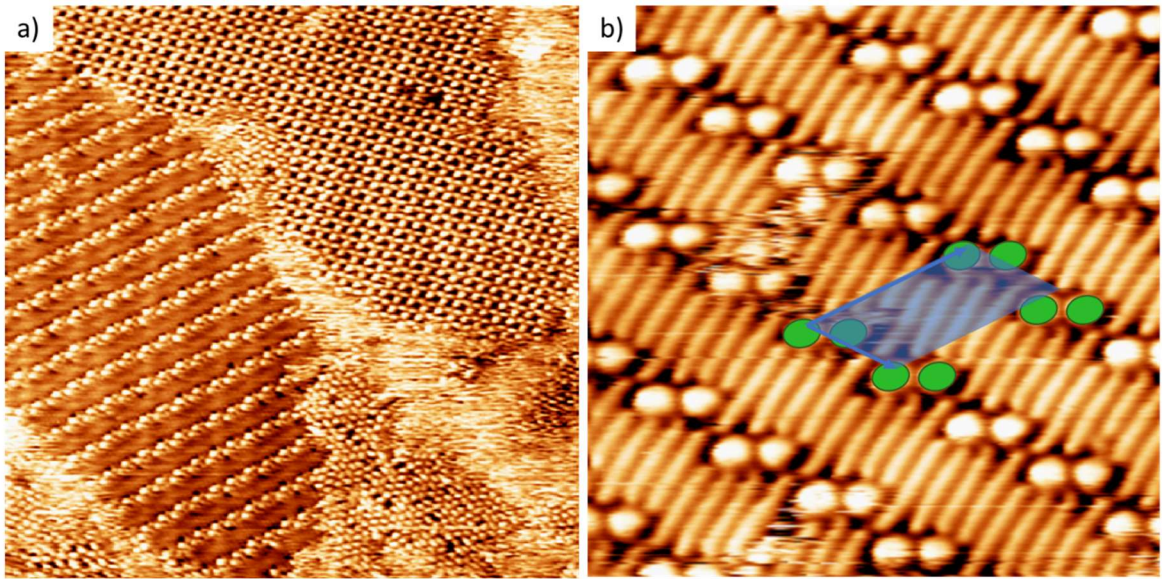

Figure 5.13: a) The DHICA/Au surface after exposure to O_2. b) Detail of the phase formed exposing the molecule to 10^{-5} mbar of O_2

5.6 Chapter bibliography

1. G. M. Whitesides, J. P. Mathias and C. T. Seto, *Science*, 1991, **254**, 1312.
2. G. M. Whitesides and M. Boncheva, *Proc. Natl. Acad. Sci U.S.A.*, 2002, **99**, 4769.
3. A. Schiffrin, A. Riemann, W. Auwärter, Y. Pennec, A. Weber-Bargioni, D. Cvetko, A. Cossaro, A. Morgante and J. V. Barth, *Proc. Natl. Acad. Sci. U.S.A*, 2007, **104**, 5279.
4. J. Reichert, A. Schiffrin, W. Auwärter, A. Weber-Bargioni, M. Marschall, M. Dell'Angela, D. Cvetko, G. Bavdek, A. Cossaro, A. Morgante and J. V. Barth, *ACS Nano*, 2010, **4**, 1218.
5. C.-A. Palma, M. Cecchini and P. Samorì, *Chem. Soc. Rev*,2012, **41**, 3713.
6. R. Otero, W. Xu, M. Lukas, R. E. A. Kelly, E. Lægsgaard, I. Stensgaard, J. Kjems, L. N. Kantorovich and F. Besenbacher, *Angew. Chem*, 2008, **120**, 9819.
7. R. Otero, M. Schöck, L. M. Molina, E. Lægsgaard, I. Stensgaard, B. Hammer and F. Besenbacher, *Angew. Chem. Int. Ed*, 2005, **44**, 2270.
8. S. Xu, M. Dong, E. Rauls, R. Otero, T. R. Linderoth and F. Besenbacher, *Nano Letters*, 2006, **6**, 1434.
9. M. S. Blois, in Photochemical and Photobiological Reviews: Volume 3, ed. K. 10.
10. E. Di Mauro, R. Xu, G. Soliveri and C. Santato, *MRS Commun*, 2017, **7**, 141.
11. A. A. R. Watt, J. P. Bothma and P. Meredith, *Soft Matter*, 2009, **5**, 3754.
12. M. D'Ischia, A. Napolitano, A. Pezzella, P. Meredith and T. Sarna, *Angew. Chem. Int. Ed*, 2009, **48**, 3914.
13. P. Meredith and T. Sarna, *Pigment Cell Melanoma Res*, 2006, **19**, 572.
14. J. Wünsche, Y. Deng, P. Kumar, E. Di Mauro, E. Josberger, J. Sayago, A. Pezzella, F. Soavi, F. Cicoira, M. Rolandi and C. Santato, *Chem. Mater*, 2015, **27**, 436.
15. M. D'Ischia, A. Napolitano and A. Pezzella, *Eur. J. Org. Chem*, 2011, **2011**, 5501.
16. S. Hong, Y. S. Na, S. Choi, I. T. Song, W. Y. Kim and H. Lee, Adv. *Funct. Mater*, 2012, **22**, 4711.
17. M. L. Tran, B. J. Powell and P. Meredith, *Biophys*. J, 2006, **90**, 743.
18. F. De Marchi, D. Cui, J. Lipton-Duffin, C. Santato, J. M. MacLeod and F. Rosei, *J. Chem. Phys*, 2015, **142**, 101923.
19. J. Yang, M. A. Cohen Stuart and M. Kamperman, *Chem. Soc. Rev*, 2014, **43**, 8271.
20. S. J. Orlow, M. P. Osber and J. M. Pawelek, *Pigment Cell Melanoma Res*, 1992, **5**, 113.
21. M. D'Ischia, A. Napolitano, A. Pezzella, E. J. Land, C. A. Ramsden and P. A. Riley, in *Advances in Heterocyclic Chemistry*, ed. R. K. Alan, Academic Press, 2005, Vol. 89.
22. L. Panzella, A. Pezzella, M. Arzillo, P. Manini, A. Napolitano and M. D'Ischia, *Tetrahedron*, 2009, **65**, 2032.
23. F. De Marchi, G. Galeotti, M. Simenas, E. E. Tornau, A. Pezzella, J. MacLeod, M. Ebrahimi and F. Rosei, *Nanoscale*, 2018, **10**, 16721.
24. R. Xu, C. T. Prontera, E. Di Mauro, A. Pezzella, F. Soavi and C. Santato, *APL Mater*, 2017, **5**, 126108.
25. L. Giovanelli, O. Ourdjini, M. Abel, R. Pawlak, J. Fujii, L. Porte, J.-M. Themlin and S. Clair, *J. Phys. Chem. C*, 2014, **118**, 14899.
26. S. Clair, M. Abel and L. Porte, Angew. Chem. Int. Ed, 2010, 49, 8237-8239. 27.
27. A. Corani, A. Huijser, T. Gustavsson, D. Markovitsi, P.-Å. Malmqvist, A. Pezzella, M. D'Ischia and V. Sundström, *J. Am. Chem. Soc*, 2014, **136**, 11626

28. I. Horcas, R. Fernandez, J. M. Gomez-Rodriguez, J. Colchero, J. Gomez-Herrero and A. M. Baro, *Rev. Sci. Instrum*, 2007, **78,** 013705.
29. G. Kresse and J. Hafner, *Phys. Rev. B*, 1993, **47**, 558-561.
30. G. Kresse and J. Furthmüller, *Phys. Rev. B*, 1996, **54**, 11169.
31. J. P. Perdew, M. Ernzerhof and K. Burke, *J. Chem. Phys*, 1996, **105**, 9982.
32. P. E. Blöchl, *Phys. Rev. B*, 1994, **50**, 17953.
33. G. Kresse and D. Joubert, *Phys. Rev. B*, 1999, **59**, 1758.
34. S. Grimme, J. *Comput. Chem*, 2006, **27**, 1787.
35. S. Grimme, J. Antony, S. Ehrlich and H. Krieg, *J. Chem. Phys*, 2010, **132**, 154104.
36. K. Momma and F. Izumi*, J. Appl. Crystallogr*, 2011, **44**, 1272.
37. D. Landau and K. Binder, *A Guide to Monte Carlo Simulations in Statistical Physics*, Cambridge University Press, 2005.
38. T. A. Pham, F. Song, M.-T. Nguyen, Z. Li, F. Studener and M. Stöhr, *Chem. Eur. J*, 2016, **22**, 5937.
39. Z. Tao, T. Wang, D. Wu, L. Feng, J. Huang, X. Wu and J. Zhu, *Chem. Commun*, 2018, **54**, 7010.
40. F. Cheng, X.-J. Wu, Z. Hu, X. Lu, Z. Ding, Y. Shao, H. Xu, W. Ji, J. Wu and K. P. Loh, *Nat. Commun*, 2018, **9**, 4871.
41. N. Thi Ngoc Ha, T. G. Gopakumar and M. Hietschold, *J. Phys. Chem. C*, 2011, **115**, 21743.
42. A. Ciesielski, S. Lena, S. Masiero, G. P. Spada and P. Samorì, *Angew. Chem. Int. Ed*, 2010, **49**, 1963.
43. M. Wriedt, A. A. Yakovenko, G. J. Halder, A. V. Prosvirin, K. R. Dunbar and H.-C. Zhou, *J. Am. Chem. Soc*, 2013, **135**, 4040.
44. S. Lei, K. Tahara, J. Adisoejoso, T. Balandina, Y. Tobe and S. De Feyter, *Cryst. Eng. Comm*, 2010, **12**, 3369.
45. S. Lei, K. Tahara, Y. Tobe and S. De Feyter, *Chem. Commun*, 2010, **46**, 9125.
46. B. E. Hirsch, K. P. McDonald, A. H. Flood and S. L. Tait, *J. Chem. Physics*, 2015, **142**, 101914.
47. M. Šimėnas and E. E. Tornau, *J. Chem. Phys*, 2013, **139**, 154711.
48. M. Šimėnas, A. Ibenskas and E. E. Tornau, *J. Phys. Chem*. C, 2015, **119**, 20524.
49. P. Szabelski, D. Nieckarz and W. Rżysko, *J. Phys. Chem*. C, 2017, **121**, 25104.
50. N. Saliba, D. H. Parker and B. E. Koel, *Surf. Sci*, 1998, **410**, 270.
51. M. Marschall, J. Reichert, K. Seufert, W. Auwärter, F. Klappenberger, A. Weber-Bargioni, S. Klyatskaya, G. Zoppellaro, A. Nefedov, T. Strunskus, C. Wöll, M. Ruben and J. V. Barth, *Chem Phys Chem*, 2010, **11**, 1446.
52. N. A. Wasio, R. C. Quardokus, R. D. Brown, R. P. Forrest, C. S. Lent, S. A. Corcelli, J. A. Christie, K. W. Henderson and S. A. Kandel, *J. Phys. Chem. C*, 2015, **119**, 21011.
53. J. Lipton-Duffin, M. Abyazisani and J. MacLeod, *Chem. Comm*, 2018, **54**, 8316.
54. H.-Y. Gao, P. A. Held, M. Knor, C. Mück-Lichtenfeld, J. Neugebauer, A. Studer and H. Fuchs*, J. Am. Chem. Soc*, 2014, **136**, 9658.
55. J. V. Barth, J. Weckesser, N. Lin, A. Dmitriev and K. Kern, *Appl. Phys. A*, 2003, **76**, 645.
56. T. Yokoyama, T. Kamikado, S. Yokoyama and S. Mashiko, *J. Chem. Phys*, 2004, **121**, 11993.
57. S. Clair, S. Pons, A. P. Seitsonen, H. Brune, K. Kern and J. V. Barth, *J. Phys. Chem. B*, 2004, **108**, 14585.

CHAPTER 6: CONCLUSIONS AND PERSPECTIVES

As we have seen in the course of the previous chapters, the deposition of functionalized indoles over a surface has proven to be an interesting yet challenging study. The $\pi - \pi^*$ interactions of the indole backbone make the molecule adsorb flat over the surface, thus makes a perfect specimen for a STM investigation. With the nanoscale resolution granted by this technique we were able to image the 2D networks created by the self-assembly of different functionalized indoles, I2CA, DHI and DHICA. At the same time, due to the small dimension of our molecular precursors, it is very hard to correctly understand the molecular orientation and its prochirality. Within this view DFT and MC modelling was fundamental, as the outcome of their simulations would support or reject our experimental hypothesis. While the main purpose of this investigation on functionalized indoles was to provide insights into the eumelanin "disordered" structure, these molecules proved to be also a useful model for the development of supramolecular structures. Regardless of the difficulties encountered, we were able to gain important knowledge on self-assembly and on the interplay between the different non-covalent interactions that govern the process.

The results concerning I2CA investigation perfectly represent this aspect. As expected, the carboxylic acid group drives the self-assembly process, leading the formation of hydrogen-bonded molecular dimers on Au(111). As our investigation moved from the UHV environment to the liquid-solid interface, less "ideal" and more akin to biological systems, we have seen the effect of the solvent on the self-assembly. At the TCB/HOPG interface, I2CA still forms the same tightly packed structure, which exhibit slight differences in the lamellar stacking due to the differing epitaxial constraints on the two surfaces. While heptanoic acid was used as a solvent, instead, the OH · · · O bonds between I2CA molecules were not present, to favour instead the formation of OH · · · N bonded dimers. The different self-assembly conformation and large spacing between the dimers implies the co-adsorption of heptanoic acid.

Comparison between the different models of I2CA networks show that the lamellar structure presents a different orientation based on the packing: while the double-lamellar structure contains one cis- and one trans-symmetric dimer in the unit cell, the single lamellar structure contains a single trans-symmetric –COOH dimer. Furthermore, energy calculations for the total cohesive energy show that in the absence of the substrate a 2D

assembly is unlikely to be stable. This suggest that the single carboxylic acid alone would not be able to build larger supramolecular structure, as the ones hypothesized for eumelanin.

The catechol group, on the other hand, opens far more possibilities, as our investigation of DHI helped reveal. When deposited on Au(111), DHI bonds into a close packed structure, whose features imagined by STM do not match the expected ones for single molecule. The possibility that the molecule forms covalent dimer structures upon adsorption without any annealing step, although unlikely, was proved by TOF-SIMS analysis. This is interesting development, as such bonding configuration is very uncommon in eumelanin units. The only known similar behaviour is the indole polymerization in acid solution, which however continues further to produce a cyclic trimer.

When deposited on Ag(111), the molecule forms again a lamellar structure, similar to the one obtained with I2CA. The molecular orientation on the other hand was a bit tilted, and XPS analysis of the sample revealed that DHI was partially oxidized upon adsorption. The structures are thus revealed to be of metal-organic nature and composed of a mixture of catechols and quinones. This oxidation process could be triggered further by exposure to oxygen, leading to additional conversion of the catechol species into quinone. In some case, the presence of IQ and can trigger a phase transition of the SAMNs, however we were not able to consistently control the oxidation ratio in order to create structures with long-range order. Despite that, such behaviour is unprecedented; while hydroxyl groups have commonly been disregarded, the inclusion of catechol groups may be a worthy tool for engineering self-assembly molecular networks.

We have thus tried to gain further insights into the catechol oxidation and reverted back to the more inert Au(111) surface. However, after the formation of the covalent dimer, DHI is stable and does not oxidize even after exposure to O_2. It was then useful to investigate the self-assembly of DHICA on Au(111), since we expected that the carboxylic acid on the pyrrole ring would prevent the formation of a covalent dimer. Furthermore, DHICA would be the perfect benchmark to test the knowledge that we have gained so far on carboxylic and catechol groups, and it will round up our investigation on eumelanin monomers.

Once on the Au surface, DHICA molecules rearrange in a plethora of polymorphs with different symmetries and packing densities, from porous to close-packed, square and hexagonal. Similar bonding motifs are shared among the phases, with the carboxylic cyclic

dimers ubiquitously present; DFT gas-phase simulation in fact show that they are the most stable intermolecular interaction, while the catechol group does not show a preferential bonding conformation. The reason behind DHICA polymorphism is thus more kinetically-driven, as MC simulations point out that even slight perturbations to the relative strength of these interactions can shift the balance between intermolecular forces, producing the different networks on the surface.

DHICA polymorphism is even more interesting when the molecule susceptibility to oxidation is taken in account. In fact, after being exposed to O2, the open lattice phase remains unaltered, while for the others the long-range order is lost and become more disordered. Interestingly, molecular rearrangement is triggered upon thermal annealing. Similar to the ordered phases of DHI/Ag(111), also in this case the networks seems to be composed of a mixed redox forms of DHICA that form a metal-organic structure.

While these results conclude our investigation on eumelanin monomers on surface, this is just the first step toward a better understanding of eumelanin structure and aggregation behaviour. STM proves to be a valuable tool for the investigation of small biologically-relevant molecules and their self-assembly behaviour, and it will be pivotal for the further development of the project. As we have seen, the surface constraint to 2D has hampered the formation of large covalent bonded systems, but this barrier may be overcome by using larger molecular precursor. Such investigation would help us moving forward a better description of the eumelanin supramolecular structure: would the eumelanin precursor self-assemble non-covalently between each other, as in the “disorder” model, or there would the formation of covalent bonds between the units still lead to the formation of a larger heteropolymer, as in the amorphous semiconductor model? Also, the study of other small, model systems, with different functionality, may push further our understanding of catecholamine polymerization, as well as the interactions that govern the molecular self-assembly.

The application of these results is however not limited to the eumelanin/biological world. Following the DHI dimerization on Au, molecular precursors could be *a priori* engineered to try to obtain an extended 2D conjugated polymer, an appealing objective for organic electronics. From a more surface science point of view, the catechol group proved to be a complex system but with plenty of potential, especially if we could achieve the control of the tautomerization of catechol-quinone. Redox reaction could be triggered in order to

induce phase transition in self-assembled networks, a useful tool for the design of nanostructures. In order to so, investigation on different metal surface, such as Pt and Pd, may prove helpful to fully understand the role of oxygen and the redox mechanism.

CHAPTER 7: ACKNOWLEDGMENTS

The results presented in this thesis were collected over a long period of time (almost six years!), during which I experienced a whole spectrum of emotions: the excitement of a discovery, the satisfaction of an accepted manuscript or the pride for a new achievement. Not everything was positive: there was the disappointment of a failed experiment, the tension during peer review process, or the irritation with the unstable instruments.

During these moments, the support of my supervisors was priceless: Dr. Lipton-Duffin would fix the instrument in few seconds, Dr. Macleod could steer every puzzling observation in a thrilling result, while prof. Ebrahimi was always ready to dive in calculations to support a new hypothesis. I am grateful to prof. Rosei for giving me the chance to be part of such high skilled research group and for his guidance that helped me succeed in preparing this thesis work.

I am also thankful to my colleagues, with whom I shared the joy and pain of PhD. They have helped me becoming a better scientist by setting an high bar (Luca, Luis, Daniele, Riccardo, Stefano and Artiom), by working side by side (Gianluca, Eduardo, Lucas, Oliver, Laurentiu and Daling), or simply by chilling during stressful times (Andrea, Yoann, Denis and Luca). I am grateful to Dominik, Penghui and Navathej, who gave me the honor to mentor them during their first steps in academia, and to Ahlem, Azza and Ahlem, who helped in the last-minute proofreading.

Finally, I must express my very profound gratitude to my family, that have provided continuous encouragement throughout my years of study, even if we live in two different continents. Lastly, I would like to thank my partner, which picked me up when I hit rock bottom and helped me through the process of researching and writing this thesis. This accomplishment would not have been possible without her. Thank you.